# UNIVERSITÀ DEGLI STUDI DI PADOVA

DIPARTIMENTO DI INGEGNERIA INDUSTRIALE

## TESI DI LAUREA MAGISTRALE IN
## INGEGNERIA CHIMICA E DEI PROCESSI INDUSTRIALI

# UTILIZATION OF CALCIUM-MAGNESIUM BASED SOLID SORBENTS FOR HIGH TEMPERATURE CO$_2$ CAPTURE

*Relatore: Ing. Matteo Strumendo*

*Correlatore: Ing. Alberto Biasin*

*Laureanda: SILVIA DOTTOR*

ANNO ACCADEMICO 2011-2012

# Riassunto

La comunità scientifica internazionale sta monitorando i cambiamenti climatici come l'aumento della temperatura media terrestre, l'estensione dei ghiacciai e l'innalzamento del livello del mare, da un lato e le emissioni di gas serra in atmosfera dall'altro. Osservando simultaneamente i due dati si è riscontrata una correlazione tra i due fenomeni. Le concentrazioni di gas serra che sono aumentate maggiormente dalla rivoluzione industriale sono quelle di $CO_2$, una cui quota significativa è legata alla produzione di energia da fonti fossili, come carbone, petrolio e gas naturale. La domanda energetica mondiale è in continuo aumento, quindi per ridurre le emissioni si deve ricorrere a fonti alternative, come le rinnovabili, e ad azioni di mitigazione. All'interno di questa categoria di azioni si colloca la cattura e lo stoccaggio di anidride carbonica, il cui scopo è appunto la separazione della $CO_2$ da correnti gassose industriali, il trasporto e lo stoccaggio della stessa in formazioni geologiche o nel fondo degli oceani in modo tale da isolarla dall'atmosfera a lungo termine; in alternativa, dopo la separazione il gas può essere riutilizzato in altri processi industriali.

Ad oggi le tecniche più utilizzate per la cattura dell'anidride carbonica sono basate su separazioni di tipo fisico o chimico condotte a bassa temperatura. In particolare, nel caso di processi di combustione si utilizzano le ammine, nel caso di processi di gassificazione si utilizza il processo Selexol. Tuttavia tali solventi possono lavorare solo a basse temperature (dell'ordine dei 100°C) e sono costosi, non solo per l'acquisto della materia prima ma anche per lo smaltimento del solvente esausto. Inoltre basse temperature di esercizio riducono l'efficienza termica del processo, in particolare nel caso di gassificazione di carbone (IGCC).

Una tecnica alternativa per catturare l'anidride carbonica è costituita dall'assorbimento su sorbenti solidi a base di ossidi di calcio e/o magnesio. Oltre ad essere materiali poco costosi, consentono di effettuare la separazione a temperature e pressioni prossime a quelle dei processi di combustione e gassificazione, consentendo quindi di ottenere un'elevata efficienza energetica.

Lo scopo di questa tesi è di presentare uno studio di fattibilità per la cattura di anidride carbonica tramite sorbenti solidi a base di ossidi di calcio e magnesio. I sorbenti a base di MgO, costituiti da dolomite semi-decomposta, sono stati usati nel dimensionamento dell'assorbitore per un impianto di gassificazione di carbone (IGCC) adottando una configurazione di pre-combustione; il sorbente a base di CaO è stato invece utilizzato per la simulazione della cattura in processi di combustione di carbone, in cui l'assorbitore è stato disposto secondo una schema di post-combustione.

Nella prima parte del lavoro di tesi, sono stati analizzati dati termodinamici e cinetici delle reazioni di decomposizione e carbonatazione dei sorbenti utilizzati. Tali dati sono necessari per poter stimare le cinetiche di assorbimento, ed in definitiva dimensionare gli assorbitori.

La correlazione tra la temperatura e la pressione parziale di decomposizione di $CO_2$ permette di identificare il sorbente da utilizzare alle fissate condizioni operative e di calcolare la forza motrice della reazione, proporzionale alla differenza tra la concentrazione di $CO_2$ nel reattore e la concentrazione di $CO_2$ di equilibrio. Una volta nota la curva di decomposizione del sorbente è possibile anche scegliere le migliori condizioni per effettuare la rigenerazione: abbassamento della pressione o innalzamento della temperatura.

Gli esperimenti riguardanti la cinetica delle reazioni sono stati condotti con analisi di tipo termo-gravimetrico (TGA), a pressione atmosferica. Per quanto riguarda le reazioni di decomposizione, i materiali analizzati sono la dolomite e la calcite e lo scopo dei test effettuati è l'identificazione della dipendenza della temperatura e del tempo di decomposizione dalla velocità del flusso di gas inviato nella camera del campione e dalla velocità di riscaldamento della stessa. La seconda serie di test effettuati riguarda la reazione di assorbimento di $CO_2$ su CaO, ed è stata eseguita per stimare la velocità di reazione e la sua dipendenza rispetto le dimensioni delle particelle. I risultati sono stati confrontati con dati di letteratura, verificando che le conclusioni, soprattutto le prestazioni in termini di velocità di reazione, siano in accordo con i valori in letteratura; questo è particolarmente importante nel caso della cinetica di assorbimento di anidride carbonica su ossidi di calcio, visto che nel dimensionamento vengono utilizzate le correlazioni (cinetiche) ricavate in letteratura. Nel caso dell'assorbimento di $CO_2$ su MgO non è stato possibile riprodurre i dati di letteratura in quando ottenuti ad alta pressione (20 bar).

Durante la ricerca bibliografica è però emerso un limite degli esperimenti condotti in TGA: questi sono affetti da limitazioni al trasporto di massa e materia all'interno del campione. Nel tipo di reattori con cui si è deciso di lavorare, ovvero *circulating fluidized bed risers*, le particelle di sorbente sono separate le une dalle altre, quindi il sistema non risente di tali resistenze al trasporto: le cinetiche ricavate da questi test risultano più lente di quelle reali, di conseguenza il dimensionamento è conservativo.

Note le informazioni riguardanti cinetica e termodinamica delle reazioni si è proceduto al dimensionamento dell'assorbitore. Questo è stato progettato verificando i bilanci di materia ed energia e assicurando che il regime di fluidizzazione consenta di operare l'assorbitore in modo continuo e stabile, quindi si è deciso di operare nei regimi di *fast fluidization* o di *core annular dilute transport*. La $CO_2$ viene fissata sull'ossido di calcio o di magnesio tramite carbonatazione dello stesso; il sorbente in uscita dall'assorbitore viene inviato al rigeneratore dove si effettua la decomposizione dei carbonati mediante la variazione delle condizioni operative, nello specifico diminuendo la pressione nel caso di IGCC e aumentando la temperatura nel caso di combustione.

Per la cattura in pre-combustione si è simulato di trattare il syngas prodotto da una centrale da 70 MW. Si è ottenuta un'efficienza di cattura pari al 68% della $CO_2$ entrante in un reattore che opera in *fast fluidization* (1.3 m di diametro per 30 m di altezza) e con sorbente costituito da dolomite semi decomposta (70 µm di diametro). Considerando che il valore desiderato per impianti di produzione di energia di grandi dimensioni è pari al 90%, il risultato ottenuto non è completamente soddisfacente. Va tuttavia ricordato che si tratta di un risultato conservativo, per i seguenti due motivi:

1) le cinetiche di reazione sono ricavate da dati ottenuti tramite esperimenti di TGA, in cui le resistenze al trasporto di materia e calore non sono trascurabili mentre nella tipologia di reattore utilizzata nel dimensionamento tali resistenze non sono significative;

2) l'assorbitore è stato dimensionato considerando una pressione operativa pari a 20 bar (poiché i dati cinetici utilizzati si riferiscono a tale pressione) ma solitamente il syngas esce dal gassificatore a pressioni maggiori; in tali condizioni operative le concentrazioni di $CO_2$ sono maggiori, quindi anche le velocità di reazione risultano maggiori con conseguente aumento dell'efficienza di cattura.

Si è riscontrato anche un problema di carattere impiantistico: il sorbente deve essere trasferito dall'assorbitore, che lavora ad alta pressione, al rigeneratore, che invece si trova a bassa pressione. Una possibile soluzione è l'adozione di due *lock hoppers* tra i due reattori: quando il solido si trova all'interno del primo dei due, questo viene temporaneamente chiuso da due valvole a ghigliottina e si effettua la variazione di pressione; il sorbente viene poi inviato al secondo *hopper* dove viene accumulato per essere inviato al rigeneratore in maniera continua tramite una valvola a rotocella. Il trasporto dal rigeneratore all'assorbitore avviene in maniera analoga.

È stato studiato anche un caso di cattura in post-combustione, applicato a fumi di combustione di una centrale di combustione di carbone da 70 MW. In questo caso l'assorbitore ha dimensioni molto maggiori (4.5 m di diametro e 20 m di altezza) per limitare le velocità del gas: trattandosi di fumi da combustione, le portate volumetriche coinvolte nel processo sono elevate, a causa dell'alta temperatura, della bassa pressione e della presenza di azoto. Il regime di moto che si instaura all'interno dell'assorbitore è il *core annular dilute transport regime*. Il sorbente utilizzato è l'ossido di calcio (100 µm di diametro) e l'efficienza di cattura risulta prossima al 90%, ovvero il risultato desiderato. Si tenga a mente che anche in questo caso i dati cinetici sono stati ricavati da esperimenti TGA, quindi la conversione effettiva potrebbe essere superiore, però nella cinetica è stato trascurato l'effetto del numero di cicli sulla capacità di cattura del sorbente. In effetti la velocità di reazione cala all'aumentare dei cicli di carbonatazione/calcinazione cui il sorbente viene sottoposto; la permanenza ad alte temperature in fase di rigenerazione provoca fenomeni di *sintering* nel sorbente. La necessità di disporre di volumi notevoli per poter installare l'unità di cattura, è un fattore limitante, soprattutto nel caso di impianti già esistenti. In questo caso si può pensare

di iniettare l'ossido di calcio direttamente a valle della camera di combustione; il dimensionamento dovrà essere affiancato da un'approfondita analisi CFD per verificare ed ottimizzare le posizioni dei punti di iniezione e di raccolta dei sorbenti, che devono essere inviati alla fase di rigenerazione.

# Abstract

This thesis deals with the carbon dioxide capture from gas streams obtained in the power generation industries, such as fossil fuel combustion and coal gasification processes. The most mature and commercially ready technologies to separate the $CO_2$ are based on the utilization of physical and chemical solvents, which can absorb the carbon dioxide at low temperatures.

The technology investigated in this work of thesis is the carbon dioxide absorption on calcium-magnesium based solid sorbents. These materials allow to operate at high temperatures; this is particularly advantageous in coal gasification processes because the thermal efficiency of the plant is higher compared to the physical solvent based capture.

The work of this thesis is divided into two main parts: 1) the computation and/or measurement of the thermodynamic and kinetic properties of the absorption reactions, and 2) the absorber design.

The thermodynamics of the thermal decomposition reactions, namely the reaction equilibrium constants, enthalpies and Gibbs free energies, are useful to understand which sorbent can be used at fixed pressure and temperature, and to evaluate the carbon dioxide absorption kinetics. Thermogravimetric analyses were conducted to obtain the decomposition temperature and time of calcite and dolomite and kinetic data of $CO_2$ absorption on calcium oxides. The performance obtained, in terms of $CO_2$ absorption rate, with calcium oxide produced by thermal decomposition of calcium carbonate is in line with the literature results. These kinetic data can be used in the design of the absorber, in the case of atmospheric capture of carbon dioxide from flue gases.

The carbon dioxide separation unit is conceived to be composed by the absorber and the regenerator. The absorber design is developed for two kinds of processes: coal gasification and coal combustion. In the two cases the plant configuration is different, with pre-combustion and post-combustion capture, respectively. Also the utilized sorbent is different, half decomposed dolomite in the first case and calcium oxide in the second. The design was developed solving the material and energy balances, and simultaneously verifying the fluidization regime of the absorber, to ensure that the absorber is operated either in the fast fluidization or in the core annular regimes.

# Index

# Introduction

Global warming is unequivocal as is evident from observations of increases in global average temperatures; the scientists relate the climate changes to the anthropogenic emission of greenhouse gases, first of all the carbon dioxide. The main industrial sector involved in $CO_2$ emissions is the power generation industry, in particular the power plant which utilize fossil fuels. To reduce the GHG emissions and to limit their effect on climate, mitigation actions must be taken. One of these mitigation actions is the carbon capture and storage, whose aim is to separate the carbon dioxide from the industrial gas streams and to transport it to a storage location, such as geological formations or oceans, or reuse it in industrial processes.

The most mature and commercially ready technologies to separate the $CO_2$ are based on the utilization of physical and chemical solvents, which can absorb the carbon dioxide at low temperatures. Amine base scrubbing is used to separate the carbon dioxide from flue gases of fossil fuel combustion power plants. The disadvantages of this technology is the high cost of the solvent and its operative limits. The amines are thermo labile and they must be used near 100°C which reduce the thermal efficiency of the process; moreover they are sensitive to poisoning due to $O_2$ and $SO_2$, frequently present in flue gases, which causes the solvent deactivation. To separate acid gases such as hydrogen sulfide and carbon dioxide from syngas, the Selexol process is used; the (physical) solvent used is composed by a mixture of the dimethyl ethers of polyethylene glycol and it is suitable for operation at high pressure and low temperature (up to 175°C). This process imparts a severe energy penalty.

An alternative process for the carbon dioxide capture is the absorption on metal oxide based solid sorbents such as calcium or magnesium. These materials are cheaper than amines, and disposal is less environmental and safety problematic. The separation can be performed at temperature and pressure close to the process conditions, preserving a high thermal efficiency in the case of coal gasification power plants. The presence of pollutant as sulfur oxide lowers the $CO_2$ capture efficiency, but they can be used to capture both the gas species.

The goal of this thesis is to present a feasibility study of the carbon dioxide capture utilizing calcium and magnesium oxide based solid sorbents. Magnesium based solid sorbents are used in the case of $CO_2$ capture in coal gasification power plants, and calcium based solid sorbents are considered in the case of $CO_2$ capture in coal combustion power plants. The objective of this work of thesis is to present a design of the absorber both in the case of pre-combustion capture in a coal gasification power plant and in the case of post-combustion capture in a coal combustion power plant.

In the first chapter an introduction to the subject of the carbon dioxide capture is presented, relating it to the global climate change. The effects and causes of the global climate change

are presented to understand why the mitigation actions are important. Then, the presently available technologies for the $CO_2$ separation are discussed.

In the second chapter the thermodynamics of the thermal decomposition of the calcium and magnesium carbonates is investigated. The knowledge of the correlation between the temperature and the decomposition partial pressure of $CO_2$ allows to identify the (thermodynamically favored) sorbent which can be used at fixed operative conditions, the driving force of the process (which is used in the kinetic calculations) and the regeneration techniques, namely lowering the pressure or increasing the temperature.

In chapter three thermogravimetric analysis (TGA) is used to investigate the absorption/calcination kinetics. Experiments were performed on dolomite and calcite decomposition to study the decomposition dependence on the gas flow rate and on the heating rate. A second set of experiments was performed on the carbon dioxide absorption on CaO. The goal of these tests was to estimate the absorption reaction rate and verify the dependence of the reaction rate on the particle diameter. Additionally, a comparison of the measured experimental data with literature data is presented; as far as the experiments on the carbon dioxide absorption this comparison is particularly important because it demonstrates that the performance, in terms of $CO_2$ absorption rate, of our calcium based sorbents is in line with the literature results.

TGA measurements can be affected by mass and energy transport phenomena; however, heat and mass transfer resistances do not affect significantly the kinetics in circulating fluidized bed risers (reactor type chosen in this work for the carbon dioxide absorption). A discussion about the impact of mass/heat transport phenomena on TGA measurements is therefore included at the end of chapter 3.

The design of the absorber reactor is presented in chapter 4. It is developed for two types of power plants: 1) integrated gasification combined cycle (IGCC) plant adopting a pre-combustion configuration with half decomposed dolomite sorbent, and 2) a coal combustion plant adopting a post-combustion plant with calcium oxide sorbent. The reactor design is based on the solution of the material and energy balances, simultaneously ensuring that the absorber is operated in the fast fluidization/core annular regimes.

# Chapter 1

# Global climate change: the driver to CCS

This chapter is an introduction to the subject dealt in this thesis, the carbon dioxide capture. Actual intensive exploitation of fossil fuels result in large quantities of $CO_2$ emissions that are closely related to climate changes observed. The aim of carbon capture and storage, being a mitigation action, is to reduce the greenhouse gas emissions.

## 1.1 Climate change

Climate change is defined by the IPCC (2007) as a change in the state of the climate that can be identified by changes in the mean and/or the variability of its properties, and that persists for an extended period, typically decades or longer. It can be due to natural variability or to human activity, and it can be measured, for example, by statistical tests. The definition is not unique, indeed, for the United Nations Framework Convention on Climate Change (UNFCCC) the climate change refers to a change of climate that is attributed directly or indirectly to human activity that alters the composition of the global atmosphere and that is in addition to natural climate variability observed over comparable time periods (IPCC, 2007). From many decades, researchers are collecting and analyzing data related to climate change in order to understand how humans have influenced it and how climate change could be mitigated.

### 1.1.1 Observations of climate changes and their effects

Warming of the climate system is unequivocal as is evident from observations of increases in global average air and ocean temperatures, widespread melting of snow and ice and rising global average sea level (IPCC, 2007) (Fig. 1.1). In the period 1995-2006, eleven of these twelve years rank among the twelve warmest years since 1850 as far as the superficial mean global temperature (the estimate of the global mean surface air temperature). From 1906 to 2005 the increase of the superficial mean global temperature was of 0.74°C. The rise of air and water mean global temperatures affects also other climate aspects, as the sea level and the snow and ice extent: global average sea level rose at the average rate of 3.1 mm per year from 1993 to 2003; mountain glaciers and snow cover has decreased by 7% in the Northern Hemisphere since 1900 (15% in spring); since 1978 the annual average Arctic sea ice extent

has shrunk by 2.7% per decade (7.4% in summer). The temperature increase is widespread over the globe but it is greater at most high northern latitudes and land regions warms faster than the oceans.

It is important to note that there is a notable lack of geographic balance in data and literature on observed changes, with marked scarcity in developing countries. Moreover, sometimes it is difficult to distinguish between changes due to the normal climate variability and anthropogenic changes.

**Changes in temperature, sea level and Northern Hemisphere snow cover**
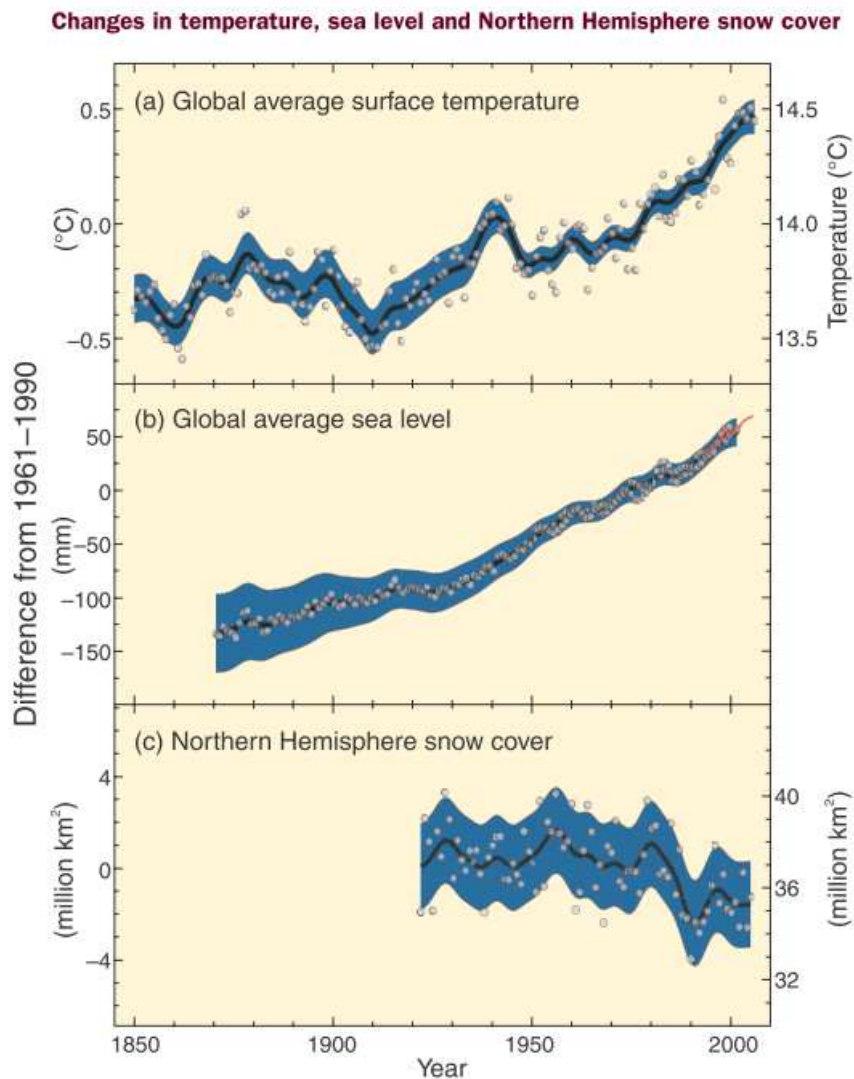


**Figure 1.1.** *Observed changes in (a) global average surface temperature, (b) global average sea level from tide gauge (blue) and satellite (red) data, and (c) Northern Hemisphere snow cover for March-April. All differences are relative to corresponding averages for the period 1961-1990. Smoothed curves represent decadal average values while circles show yearly values; the shaded areas are the estimated uncertainty intervals (IPCC, 2007)*

The international organism that collects and analyzes climate change data is the Intergovernmental Panel on Climate Change (IPCC), instituted in 1988 by the Word

Meteorological Organization (WMO) and by the United Nations Environmental Program (UNEP); its aim is to produce scientific, technical and socioeconomic guide lines to be presented to the United Nations Framework Convention on Climate Change (UNFCCC).

From 1900 to 2005, precipitations increased significantly in eastern parts of the North and South America, northern Europe and northern and central Asia whereas precipitation declined in the Sahel, in the Mediterranean, in southern Africa and in parts of southern Asia. Globally, the area affected by drought has increased since the 1970s (IPCC, 2007).

Some extreme weather events have changed in frequency and/or intensity over the last 50 years: it is very likely that cold days, cold nights and frosts have become less frequent over most land areas, while hot days, hot nights and heat waves have become more frequent; the frequency of heavy precipitations has increased over most areas and the incidence of extreme high sea level has increased at a broad range of sites worldwide since 1975. Some climate aspects appear not to have changed and, for some, data inadequacies mean that it cannot be determined if they have changed. For example there are no significant average multi-decadal trend for Antarctic sea ice extent, the meridional overturning circulation, tornadoes, hail, lightning and dust storms.

Natural systems are influenced by the regional climate changes; all the different studies data (IPCC, 2007) confirm that more than the 89% of significant changes observed in the physical and biological system are consistent with a response expected to warming. Systems connected to snow, ice and frozen ground are affected by enlargement and increased numbers of glacial lakes, increasing ground instability in permafrost regions and rock avalanches in mountain regions, changes in some Arctic and Antarctic ecosystems, including those in sea-ice biomes, and predators at high levels of the food web. Warming is affecting also terrestrial biological systems, mainly due to the earlier timing of spring events: leaf-unfolding, bird migration, egg-laying, poleward and upward shifts in habitat of plants and animals. The rising water temperatures and the changes in ice cover, salinity, oxygen levels and circulation will lead to changes in marine and freshwater biological systems: algal, plankton and fish are migrating towards high latitude oceans, algal and zooplankton are more abundant in oceans and lakes and natural fish migration in river happens earlier. Some of this effects can be induced also by overfishing and pollution, which are not climate related stresses, but identifying the real cause is complex.

## 1.1.2 Causes of climate change

Usually, human activities result in emissions of four long lived GHGs (IPCC, 2007): carbon dioxide $CO_2$, methane $CH_4$, nitrous oxide $N_2O$ and halocarbons (gases containing fluorine, chlorine or bromine). The warming influence of a GHG is measured in terms of radiative forcing, namely the variation of the net irradiance at the boundary between the troposphere

and the stratosphere. The climate change responses are different for different GHGs, because they have different warming influence on the global climate system due to different radiative properties and lifetimes in the atmosphere. In order to compare the different influences, these may be expressed through a common metric based on the radiative forcing of carbon dioxide: the $CO_2$ equivalent emission that is the amount of $CO_2$ emission that would cause the same time integrated radiative forcing over the same period (IPCC, 2007). It is obtained by multiplying the emission of a GHG by its global warming potential for the given time horizon; for a mixture of different GHGs the emissions of each gas are summed. The global warming potential (GWP) is the index used to measure the radiative forcing of a unit mass of a given greenhouse gas in today's atmosphere integrated over a chosen time horizon, relative to that of $CO_2$. The GWP represents the combined effect of the differing times these gases remain in the atmosphere and their relative effectiveness in absorbing outgoing thermal infrared radiation (IPCC, 2007). The reference gas is the carbon dioxide because it is the most emitted anthropogenic GHG (77% of total emissions in 2004 are due to human activities and its annual emissions have grown by 80% between 1970 and 2004, increasing from 21 in 1970 to 38 Gt in 2004).
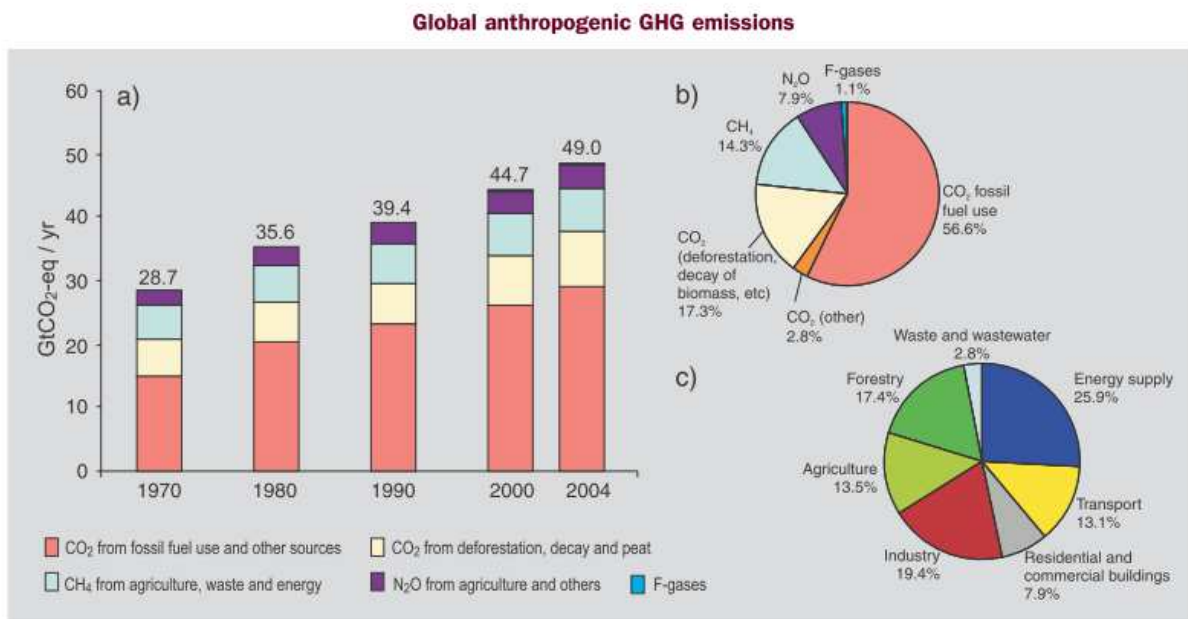


**Figure 1.2.** *(a) Global annual emissions of anthropogenic GHGs from 1970 to 2004; (b) share of different anthropogenic GHGs in total emissions in 2004 in terms of $CO_2$eq; (c) share of different sectors in total anthropogenic GHG emissions in 2004 in terms of $CO_2$eq (forestry includes deforestation) (IPCC, 2007)*

Global anthropogenic GHG emissions have grown since 1750, with an increase of 70% between 1970 and 2004 (Fig 1.2). The increasing rate of $CO_2$eq emissions was higher during the period 1995-2004 (0.92 $GtCO_2$eq/year) than during the previous period of 1970-2004

(0.43 GtCO$_2$eq/year). The sectors that register the largest growth in GHG emissions are the power generation industry, the transport and the industry sectors. The impact of the residential and commercial buildings, forestry and agriculture on GHG emissions has been lower.
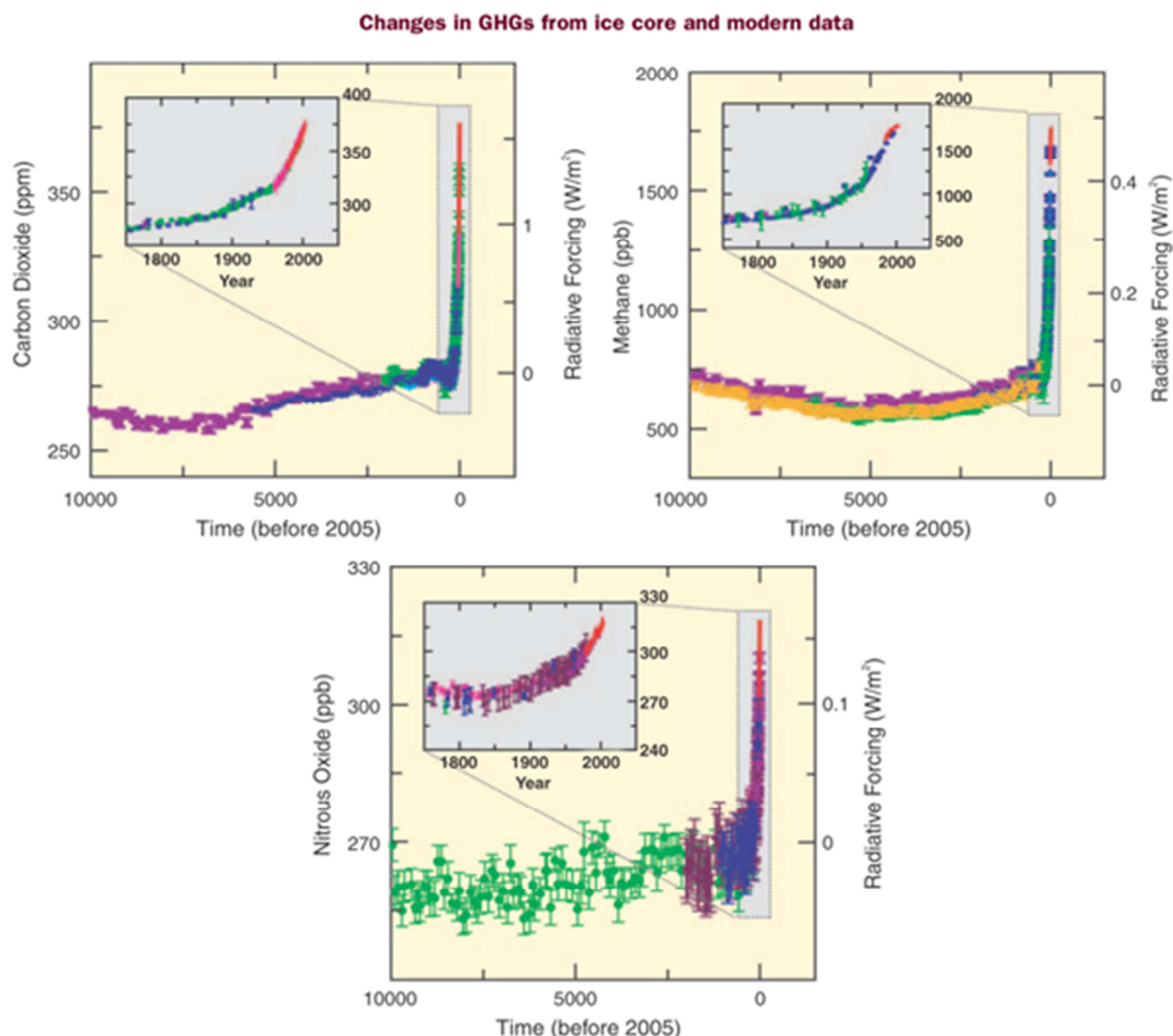


**Figure 1.3.** *Atmospheric concentration of CO$_2$, CH$_4$ N$_2$O over the last 10000 years(large panel) and since 1750 (insert panel). Measurements are shown from ice cores (symbols with different colours for different studies) and atmospheric samples (red lines). The corresponding radiative forcings relative to 1750 are shown on the right hand side axes of the large panels (IPCC, 2007)*

The global atmospheric concentration of CO$_2$ increased from a pre-industrial value of about 280 ppm to 379 ppm in 2005; its annual growth rate is increased during the period 1995-2005 (1.9 ppm/year while in the period 1960-2005 is 1.4 ppm/year), although there is year to year variability in growth rate. Increases in CO$_2$ concentrations are due primarily to fossil fuel and land use change.

The global atmospheric concentration of CH$_4$ has increased from a pre-industrial value of about 715 ppb to 1732 ppb in the early 1990s; since then, growth rates have declined (its

concentration was 1774 ppb in 2005) consistent with total emissions (sum of anthropogenic and natural sources) being nearly constant during this period. It is supposed that the methane emissions are due to agriculture and fossil fuel use.

Global atmospheric concentration of $N_2O$ has increased from a pre-industrial value of about 270 ppb to 319 ppb in 2005. The increase in this concentration is primarily due to agriculture. Many halocarbons have increased from a near zero pre-industrial background concentration primarily due to human activities.

It is worth to note that there are significant differences in per capita income, per capita emissions and energy intensity among different countries. In 2004 UNFCCC Annex I countries (Australia, Austria, Belarus, Belgium, Bulgaria, Canada, Croatia, Czech Republic, Denmark, Estonia, Finland, France, Germany, Greece, Hungary, Iceland, Ireland, Italy, Japan, Latvia, Liechtenstein, Lithuania, Luxembourg, Malta, Monaco, Netherlands, New Zealand, Norway, Poland, Portugal, Romania, Russian Federation, Slovakia, Slovenia, Spain, Sweden, Switzerland, Turkey, Ukraine, United Kingdom of Great Britain and Northern Ireland, United States of America) held the 20% population, produced 57% of the world's Gross Domestic Product based on Purchasing Power Parity and accounted for 46% of global GHG emissions.

The combined radiative forcing due to increases in $CO_2$, $CH_4$ and $N_2O$ is +2.3 W/m$^2$ and their radiative forcing is increased since the industrial era. Also anthropogenic contributions to aerosols (sulphate, organic carbon, black carbon, nitrate and dust) must be considered: they produce a cooling effect with a total radiative forcing of -0.5 W/m$^2$ and an indirect cloud albedo forcing of -0.7 W/m$^2$ that counteracts the GHGs warming effect. Then, the net effect of anthropogenic activities, since 1750, has been a global warming with a radiative forcing of +1.6 W/m$^2$.

The equilibrium climate sensitivity is a measure of the climate system response to sustained radiative forcing. It is defined as the equilibrium global average surface warming following a doubling of $CO_2$ concentration. IPCC assessed that climate sensitivity is likely to be about 3°C, in any case between 2 and 4.5°C. As far as these considerations, feedbacks must be carefully evaluated because they can amplify or dampen the response to a given forcing. For example, the water vapor is a GHG with a negligible radiative forcing but when the global average temperature increases, its tropospheric concentration increases. Warming reduces terrestrial and ocean uptake of atmospheric $CO_2$, increasing the fraction of anthropogenic emissions remaining in the atmosphere. This positive feedback leads to larger atmospheric $CO_2$ increases and greater climate change for a given emission scenario; the strength of this feedback effect varies markedly among models.

The process of attribution of causes of climate change evaluates if the observed changes are consistent with the expected response to external forcings (changes in solar irradiance or anthropogenic emissions) and inconsistent with alternative physically plausible explanations. Global climate change of the past 50 years are explainable considering natural and

anthropogenic forcings together, indeed simulation models reproduce correctly the warming pattern if the two causes are considered. The observed pattern of tropospheric warming and stratospheric cooling is very likely due to the combined influences of GHG increases and stratospheric ozone depletion because solar and volcanic forcings alone would likely have produced cooling, instead of warming in troposphere.

Anthropogenic forcing is likely to have contributed to changes in wind patterns, affecting extra-tropical storm tracks, sea level rise, hydrological cycle (including the precipitations) and it is very like that drought areas increase because of human influence (IPCC, 2007).

Global warming has likely had an influence in observed changes in physical and biological systems: several studies have demonstrated a spatial correspondence between regions more affected by warming and areas in which were observed significant changes in natural systems consistent with warming and therefore this link cannot be due only to natural variability of temperatures and/or systems.

Difficulties remain in simulating and attributing observed temperature changes at smaller scales: on these scales natural climate variability is relatively larger, making it harder to distinguish between natural changes and changes caused by external forcings.

### 1.1.3 Mitigation

Because of observed climate changes, there is a general agreement among scientists that mitigation policies and sustainable development practices must be adopted. Societies can respond to climate change by adapting to impacts and adopting mitigation actions, that is to reduce GHG emissions, in order to attenuate the rate and the magnitude of changes. The capacity to adapt and mitigate is dependent on socio-economic and environmental circumstances and the availability of information and technology of each country. Beyond increasing energy efficiency, the countries can consider the use of low carbon energy sources: renewable sources energy, nuclear power, $CO_2$ carbon capture and storage and widening forests which are natural sinks for $CO_2$ accumulation. Additionally life style changes can contribute to mitigation in several sectors (changes in consumption patterns, education and trainings, in building occupant behavior, transport demand management, etc.), but it is essential that policies provide incentives for low GHG products, technologies and processes (IPCC, 2007). There is not a single technology that is sufficient to mitigate all the global warming effects, for this reason it is important to implement different mitigation actions in order to realize synergies and obtain direct and long term effects.

The macro-economic costs of mitigation usually rise with the stringency of the stabilization target. In 2050 global average macro-economic costs for mitigation towards stabilization between 710 and 445 ppm of $CO_2$eq are expected to correspond to slowing the average annual global GDP growth by less than 0.12 percentage points (IPCC, 2007). Adopting international

cooperation it is possible to reduce the emissions lowering costs and incrementing the action efficiency. For these reasons UNFCCC instituted the Kyoto Protocol: its aim is to find a response to climate change problem stimulating an array of national policies, creating an international carbon market and establishing new institutional mechanisms that may provide new mitigation actions. To obtain the aims periodically fixed by the Protocol, different elements can be adopted, as emissions targets, sectorial, local, regional actions, research and development programs, common policies and financing instruments.

## 1.2 Carbon capture and storage

Carbon dioxide capture and storage (CCS) is a process consisting of the separation of $CO_2$ from industrial and energy-related sources, transport to a storage location and long-term isolation from the atmosphere (IPCC, 2005). CCS is a mitigation action useful for stabilization of atmospheric greenhouse gas concentration; this should be adopted with other mitigation options in order to reduce global costs and increase flexibility in achieving GHG emission reductions. Other possible options indicated in the IPCC report (2005) are energy efficiency improvements, switch to less carbon intensive fuels, nuclear power, renewable energy sources, enhancement of biological sinks and reduction of non $CO_2$ GHG emissions.

Carbon capture can be applied to large point sources as fossil fuel or biomass energy facilities, major $CO_2$ emitting industries, natural gas production, synthetic fuel plant and fossil fuel based hydrogen production plant. Once captured, the gas can be compressed and stored in geological formations or oceans, as mineral carbonates or used in industrial processes.
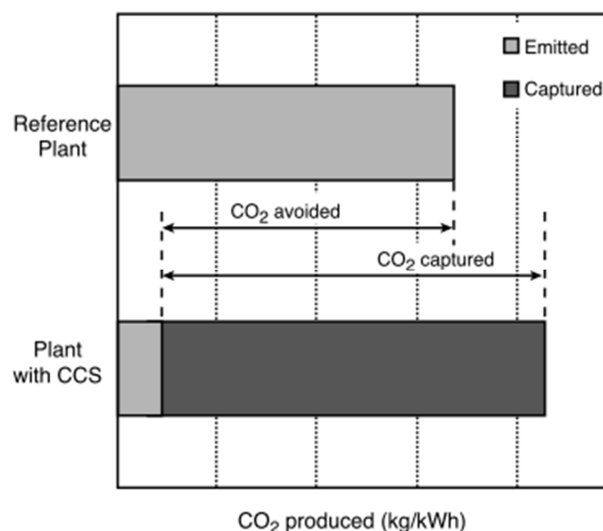


**Figure 1.4.** *$CO_2$ capture and storage from power plants: the increased $CO_2$ production resulting from the loss in overall efficiency of power plants due to the additional energy required for capture, transport and storage and any leakage from transport result in a larger amount of "CO2 produced per unit of product" (lower bar) relative to the reference plant (upper bar) without capture (IPCC, 2005)*

Available capturing technology allows to capture 85-95% of the processed $CO_2$; a plant equipped with CCS system would need 10-40% more energy than the equivalent plant without CCS to be used for capture and compression of the gas. The net result is that the carbon dioxide atmospheric emissions are reduced by 80-90% compared to the plant without capture section (Fig. 1.4).
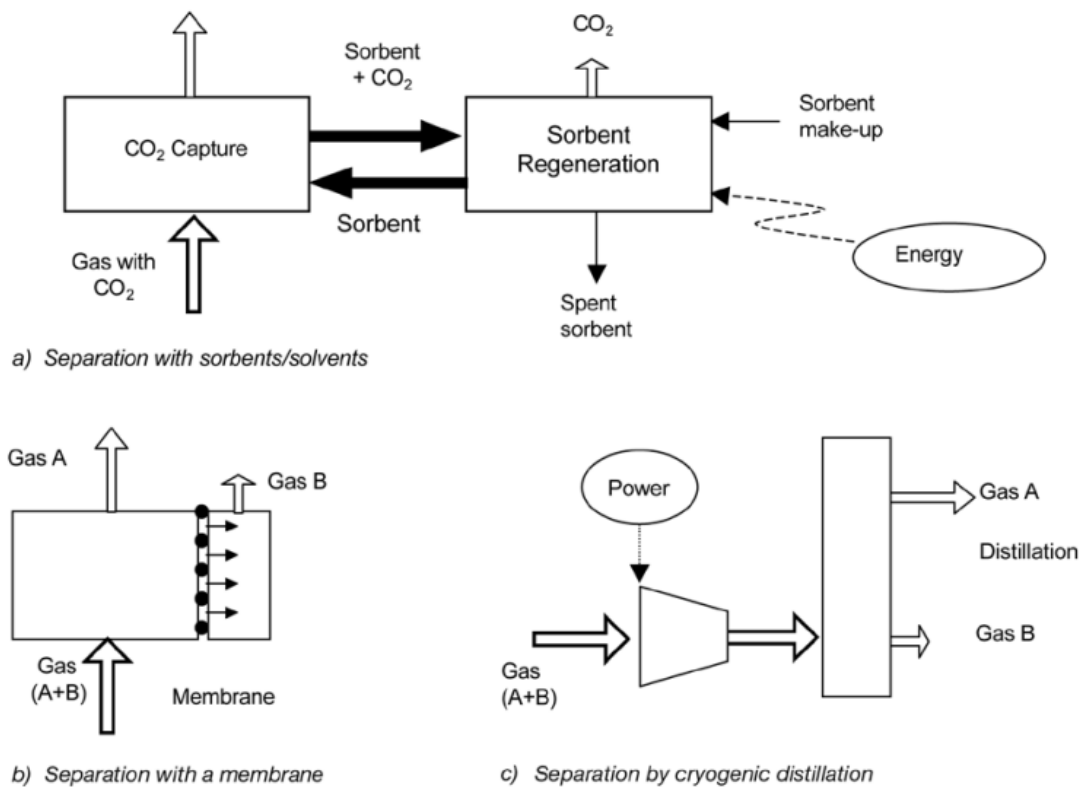


**Figure 1.5.** *General schemes of the main separation processes relevant for $CO_2$ capture: (a) separation with sorbents or solvents, (b) separation with membrane, (c) separation by cryogenic distillation (IPCC, 2005)*

The capturing technologies to obtain the $CO_2$ separation are: sorbents or solvents, membranes and cryogenic distillation.

The separation with sorbents or solvents is achieved by processing the $CO_2$-rich gas in intimate contact with a liquid absorbent or a solid sorbent that capture the $CO_2$ (Fig. 1.5a). Usually the sorbent can be regenerated, in a continuum or discontinuous way, by heating and/or pressure decreasing and it can be utilized again to capture the $CO_2$. It is always required a fresh sorbent makeup flow to compensate the natural decay of activity or sorbent losses. One problem of this kind of capture system is that the sorbent flow between the absorber and the regenerator, in the continuum process, is large, in order to match the significant flow of $CO_2$ processed (IPCC, 2005): equipment sizes and energy requirement are therefore large and entail efficiency penalty and added costs. Moreover, some sorbent

materials, as monoethanolammine, can be very expensive not only as raw materials but also as residuals to be disposed.

The separation with membranes is obtained by selective permeation of a gas through them (Fig. 1.5b). Membranes can be made with different materials, as polymers, metals and ceramics, which determine the selectivity to the different gases; the passage of the gas is driven by the pressure difference across the membrane. This kind of separation has not yet been applied at large scale and research and development efforts are in progress (IPCC, 2005).

The separation by cryogenic distillation requires that the gas stream is condensed, by compression and cooling then the gas is separated in a distillation column (Fig. 1.5c). As far as carbon capture, this technology is used to separate impurities from high purity $CO_2$ streams, such as in the case of oxyfuel combustion or in the case of water gas shifted syngas (IPCC, 2005).

There are different types of $CO_2$ capture systems: post-combustion, pre-combustion and oxyfuel combustion.

Post-combustion capture is usually utilized in conventional coal fired, oil fired or gas fired power plants. During the fuel combustion, water vapor is produced and it is used to drive a turbine/generator to produce electricity; flue gas goes to pollutant control unit in order to limit nitrogen oxide $NO_x$, particulate matter and sulphur dioxide $SO_2$ emissions (Fig. 1.6). This configuration implies that the treated gas has high volume, $CO_2$ is dilute (12-14 mol% $CO_2$) and that the other pollutants present can degrade the used solvent/sorbent.
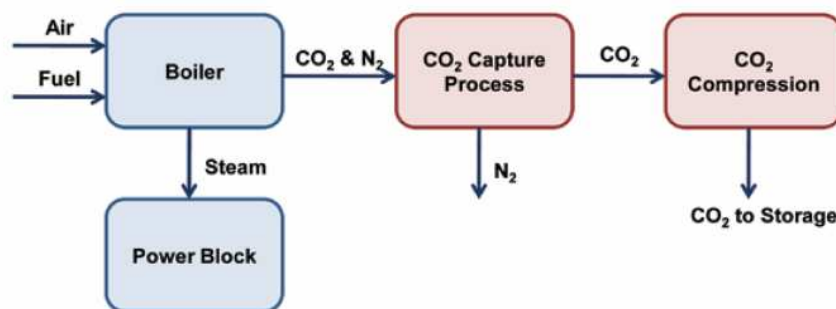


**Figure 1.6.** *Block diagram illustrating power plant with post-combustion $CO_2$ capture (US DOE, 2010)*

Pre-combustion capture is mainly applicable to gasification plant. The produced syngas, a mixture of $H_2$ and CO, is sent to the water-gas-shift reaction where CO is converted to $CO_2$ increasing the $H_2$ production. Carbon dioxide is then removed and the hydrogen rich syngas is used as fuel in a combustion turbine (Fig. 1.7). The separation in this case is favoured by the high concentration of $CO_2$ (15-60%) and the high pressures used in the gasifier.
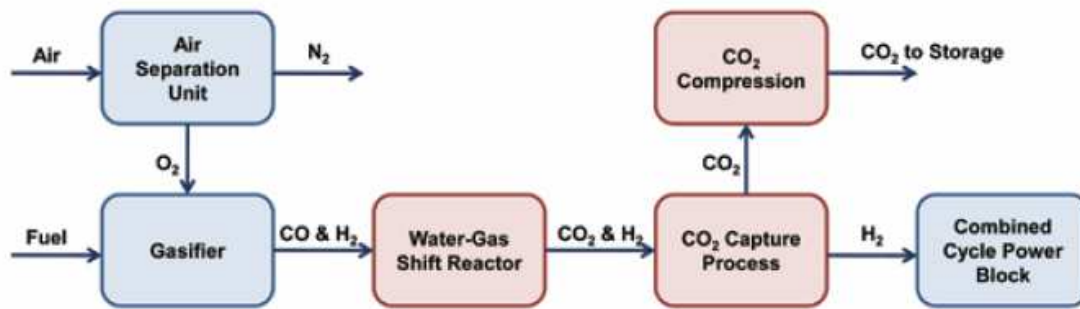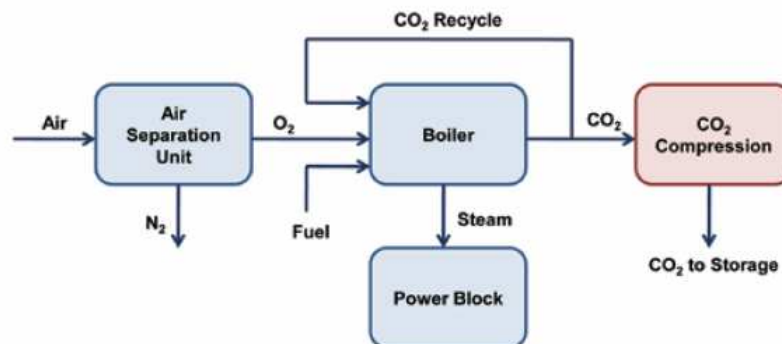
**Figure 1.7.** *Block diagram illustrating power plant with pre-combustion $CO_2$ capture (US DOE, 2010)*

Oxyfuel combustion is applicable to new and existing coal fired power plant. In this case the combustion is conducted in oxygen with a purity degree of 95-99% instead of air resulting in a flue gas constituted by $CO_2$ (80% or more) and $H_2O$ (part of flue gas can be recycled to the combustor to moderate the temperature); the $CO_2$ separation is obtained by water condensation through cooling and/or compression (Fig. 1.8). This configuration allows to process small flue gas volumes and concentrated $CO_2$ streams are directly produced, but the air separation unit to obtain $O_2$ is very expensive.



**Figure 1.8.** *Block diagram illustrating power plant with oxyfuel-combustion $CO_2$ capture (US DOE, 2010)*

The largest cost component is represented by the capture, including the compression (IPCC, 2005). However the IPCC previsions affirm that such cost will be reduced by 20-30% thanks to new technologies which are now been investigated while the transport and storage costs could decrease slowly with the maturing of technologies and the increasing of the plant scale.

In its report, the IPCC (2005) sets down the $CO_2$ capture cost ranges for new power plants, using technologies in commercial use to estimate the costs; the power produced by plant without capture is supposed to be 400-800 MW, for the one with capture it drops to 300-700 MW. For power plants, that are large source of $CO_2$, the cost of capturing this GHG is the largest component of all CCS costs; therefore, in this analysis the transport and the storage costs are not included (IPCC, 2005). Capture units require energy to be operated and this is

translated in plant efficiency losses. More fuel is needed to produce the same kWh of electricity output: usually 24-40% for a coal plant and 14-25% for a IGCC plant. In both cases, the $CO_2$ reduction per kWh fall in the range 80-90% but the capital cost increase is bigger in the first case: 44-74% versus 19-66% for the second one. This affects the cost of electricity production by an increase of 42-66% and 20-55% respectively: for coal plant this cost passes from 0.043-0.052 to 0.062-0.086 US$/kWh; for IGCC plant from 0.041-0.061 to 0.054-0.079 US$/kWh. The resulting cost of net carbon dioxide capture is 29-51 US$/tCO$_2$ for pulverized coal plant and 13-37 US$/tCO$_2$ for IGCC plant.

As far as the carbon dioxide transport, pipelines are the most common method used and $CO_2$ is in gaseous phase, usually at 8 MPa. It can be moved also in ships, road or rail tankers and this case it is in liquid phase. To ensure the safety of humans and environment the transport requires detailed route selection and tanks or pipelines must be equipped with over pressure protections and leak detectors. The transport costs depend on the distance, the quantity and, for pipelines, the morphology land; for this reason for a detail treatment we refer to the IPCC report (2005) Chapter 4.

As far as the storage, the IPCC report (2005) illustrates the geological and the ocean storage (refer to Chapters 5 and 6), but there are also options that consider the reutilization of the $CO_2$: mineral carbonation and industrial use. When carbon dioxide reacts with alkaline or alkaline-earth oxides, as magnesium oxide MgO or calcium oxide CaO, it forms carbonates that are stable over long time scales. They can be disposed or used in construction industries as cement compound. Captured $CO_2$ can be used in all the processes where it is a reactant, such as the urea and methanol production, horticulture, refrigeration, pharmaceuticals production, food and beverages industries, welding and fire extinguishers (IPCC, 2005). However in these applications the carbon dioxide can have a limited storage times: it can degrade sooner to $CO_2$ and be emitted to the atmosphere. In addition it is not sure that industrial re-use results in a net reduction of $CO_2$ emissions; a detailed life cycle analysis should be performed.

The IPCC (2005) foresees a large deployment of CCS only if policies are imposed to limit the GHG emissions, otherwise its diffusion is unlikely, and its effectiveness on mitigation will be relevant if it is applied to the power generation sector. The utilization of CCS could reduce by 30% or more the $CO_2$ concentration stabilizing costs and it will be competitive because this technology is compatible with most energy plants.
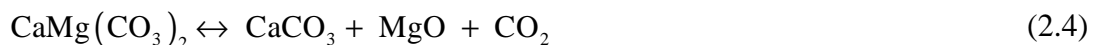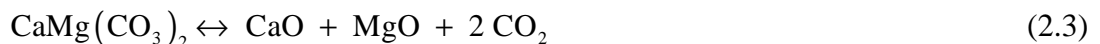
# Chapter 2

# Thermodynamics of calcite, magnesite and dolomite

This chapter deals with the thermodynamics of the thermal decomposition reactions of the calcium and magnesium carbonates. The knowledge of the reaction equilibrium constants, enthalpies and Gibbs free energies is required to understand what reactions can occur at given conditions of pressure and temperature and to evaluate the equilibrium $CO_2$ concentration, which is needed to compute the carbon dioxide absorption kinetic.

## 2.1 Considered reactions

This goal of this thesis is to analyze the applicability of calcium and magnesium based solid sorbents to the high temperature $CO_2$ capture. The compounds that can absorb such gas are calcium oxide and magnesium oxide. They can be obtained from the calcination of the respective carbonates or of the dolomite, which is composed by both of them. The reactions analyzed in this chapter are the calcite (2.1), magnesite (2.2) and dolomite thermal decompositions. As far as the dolomite, both the complete (2.3) and the half decomposition (2.4) reactions will be analyzed:

$$CaCO_3 \leftrightarrow CaO + CO_2 \tag{2.1}$$

$$MgCO_3 \leftrightarrow MgO + CO_2 \tag{2.2}$$

$$CaMg(CO_3)_2 \leftrightarrow CaO + MgO + 2\,CO_2 \tag{2.3}$$

$$CaMg(CO_3)_2 \leftrightarrow CaCO_3 + MgO + CO_2 \tag{2.4}$$

The knowledge of the reaction equilibrium constants, enthalpies and Gibbs free energies is required to understand what reactions can occur at the given conditions of pressure and temperature. More specifically they are required to define the values of $T$ and $P$ in which carbon dioxide absorption (or desorption) is thermodynamically allowed. Additionally, from the thermodynamics equilibrium conditions, the carbonates decompositions curve are computed. These identify the values of pressure (carbon dioxide partial pressure), as a

function of the temperature, above which carbon dioxide absorption is thermodynamically favored. On this ground it is possible to evaluate which sorbents (calcium, magnesium or dolomite based sorbents) can be used for the $CO_2$ absorption at given $T$ and $P$.

## 2.2 Governing equations

The equilibrium criterion for a multicomponent reactive system, at constant pressure $P$ and temperature $T$, is the minimization of the Gibbs potential $G$ with respect to the extents of reaction $\varepsilon_j$ (in case of multiple nr reactions):

$$\left( \frac{\partial G}{\partial \varepsilon_j} \right)_{T,P,\varepsilon_{i \neq j}} = 0 \qquad j = 1, 2, ..., nr. \tag{2.5}$$

In the case of a single reaction, the extent of reaction describes the progress of the reaction and is proportional to the variation of the number of moles of component $i$ in the system $N_i$:

$$d\varepsilon = \frac{dN_i}{v_i}. \tag{2.6}$$

In eq. (2.6) $v_i$ is the stoichiometric coefficient of the species $i$; usually the eq. (2.6) is integrated from the reaction beginning, thus $\varepsilon$ is zero and $N_i$ is equal to the moles initially present in the reactor.

The equilibrium criterion can be rewritten in terms of the activities $a_i$ of the involved species (*nc* is their total number) (Schieber and de Pablo, under publication). In the case of a single reaction the equilibrium condition can be written as:

$$\prod_{i=1}^{nc} a_i^{v_i} = K(T). \tag{2.7}$$

$K$ is the equilibrium reaction constant, defined as:

$$K(T) = \exp\left[ -\frac{\Delta g^0(T)}{RT} \right] \tag{2.8}$$

and is a function of the temperature $T$ only; $\Delta g^0$ is the standard Gibbs free energy change of reaction and $R$ is the universal gas constant. Assuming the standard state, identified by the superscript $^0$, as the pure substance at $P_{ref} = 1$ bar, the $\Delta g^0$ can be evaluated from the Gibbs

free energy of formation of each component tabulated at $T_{ref} = 298.15$ K and the natural state of the component:

$$\Delta g^o(T_{ref}) = \sum_{i=1}^{nc} \nu_i \Delta g_{form,i}^0(T_{ref}) . \tag{2.9}$$

In order to find the standard Gibbs free energy change of reaction at an arbitrary temperature $T$, the formula that must be used is one of the following (Schieber and de Pablo, under publication):

$$\Delta g^0(T) = \Delta h^0(T) - T \Delta s^0(T) \tag{2.10}$$

$$\Delta g^0(T) = \Delta g^0(T_{ref}) - (T - T_{ref})\Delta s^0(T_{ref}) + \int_{Tref}^{T} \left(\frac{T'-T}{T'}\right)\Delta c_p(T')dT' . \tag{2.11}$$

In these equations $\Delta s^0$ is the standard entropy change of reaction, $\Delta h^0$ is the standard enthalpy change of reaction and they are evaluated as summation of the entropy/enthalpy of formation of each component times the stoichiometric coefficients (in analogous way as for the Gibbs free energy change, eq.(2.9)), $\Delta c_p(T)$ accounts for the heat capacity variation in the reaction:

$$\Delta c_p(T) = \sum_{i=1}^{nc} \nu_i c_{p,i}(T) . \tag{2.12}$$

To use eq. (2.10), the component enthalpy and entropy of formation must be tabulated at the desired temperature $T$; if such data are lacking the second equation can be used.

The equilibrium constant dependence on the temperature can be computed using two methodologies. In the first one (method A), given the dependence of the standard Gibbs free energy change of reaction with respect to the temperature $\Delta g^0(T)$, it is then possible to evaluate the equilibrium constant $K(T)$ through eq. (2.8).

A second methodology (method B) to compute the reaction equilibrium constant as a function of the temperature is based on the standard reaction enthalpy change $\Delta h^0$ (Schieber and de Pablo, under publication):

$$\ln\left[\frac{K(T)}{K(T_{ref})}\right] = \int_{Tref}^{T} \frac{\Delta h^0(T')}{RT'^2}dT' \tag{2.13}$$

therefore the equilibrium reaction constant is given by the equation:

$$K(T) = K(T_{ref}) \exp\left[ \int_{Tref}^{T} \frac{\Delta h^0(T')}{RT'^2} dT' \right]. \tag{2.14}$$

The reaction standard enthalpy change can be computed from the heat capacities of the reactants and products involved:

$$\Delta h^0(T) = \Delta h^0(T_{ref}) + \int_{Tref}^{T} \Delta c_p(T') dT'. \tag{2.15}$$

To estimate the heat capacities, reaction enthalpy and Gibbs free energy changes, tabulated data from different sources had been used, depending on the reaction:

a) data from the Perry's Chemical Engineer's Handbook (Perry and Green, 1997) were used for the calcium carbonate decomposition (eq.(2.1)),

b) data from the NIST-WebBook (which uses as a source Chase, 1998) were used for the magnesium carbonate decomposition (eq.(2.2)),

c) data from Knacke et al. (1991) were used for the dolomite decompositions (eq. (2.3) and (2.4)).

Heat capacities are evaluated in the three cases with different formulas thus to evaluate the standard Gibbs free energy change (when eq. (2.11) is used), standard enthalpy change and the equilibrium constant of the reaction (when method B is used).

In the case of calcium carbonate and dolomite decompositions, in both methods A and B, the heat capacities are evaluated using Perry and Green (1997) and Knacke et al. (1991) data. They compute the heat capacity $c_p$ [J/mol*K] of a given substance as a function of temperature with the same expression:

$$c_p = a + bT + \frac{c}{T^2} \tag{2.16}$$

where temperature is in Kelvin.

Correspondingly the heat capacity variation of the reaction $\Delta c_p$ is:

$$\Delta c_p = A + BT + \frac{C}{T^2}. \tag{2.17}$$

In eq. (2.17) capital letters $A$, $B$ and $C$ denote the difference between the summation of involved species coefficients, in agreement with eq. (2.12).

In the case of magnesium carbonate decomposition, the heat capacities are evaluated using NIST-WebBook data. In this case, the formula of the heat capacity of a given substance $c_p$ [J/mol*K] is computed by:

$$c_p = a' + b't + c't^2 + d't^3 + \frac{e'}{t^2} \tag{2.18}$$

where and $t=T[K]/10^3$.

Subtracting reactant coefficients from the product ones allow to obtain the heat capacity variation of the reaction $\Delta c_p$:

$$\Delta c_p = A' + \frac{B'T}{10^3} + C'\frac{T^2}{10^6} + D'\frac{T^3}{10^9} + E'\frac{10^6}{T^2}. \tag{2.19}$$

In eq. (2.19) capital letters denote the difference between the summation of product coefficients and the summation of reactant coefficients, in agreement with eq. (2.12).

## 2.2.1 Formulas for calcium carbonate and dolomite decompositions (method B)

Substitution of eq (2.17) in eq (2.15) gives the value of the reaction standard enthalpy change:

$$\Delta h^0(T) = \Delta h^0(T_{ref}) + \int_{Tref}^{T} \left( A + BT' + \frac{C}{T'^2} \right) dT'$$

$$= \Delta h^0(T_{ref}) + A(T - T_{ref}) + \frac{B}{2}(T^2 - T_{ref}^2) - C\left( \frac{1}{T} - \frac{1}{T_{ref}} \right). \tag{2.20}$$

Substitution of eq (2.20) in eq (2.13) gives:

$$\ln\left[ \frac{K(T)}{K(T_{ref})} \right] = \int_{Tref}^{T} \left[ \Delta h^0(T_{ref}) - AT_{ref} - \frac{B}{2}T_{ref}^2 + \frac{C}{T_{ref}} \right] \frac{1}{RT'^2} dT' + \int_{Tref}^{T} \left( \frac{A}{RT'} + \frac{B}{2R} - \frac{C}{RT'^3} \right) dT'$$

$$= \frac{cost_1}{R} \left[ -\frac{1}{T'} \right]_{Tref}^{T} + \left[ \frac{A}{R}\ln T' + \frac{B}{2R}T' + \frac{1}{2}\frac{C}{RT'^2} \right]_{Tref}^{T}$$

$$= -\frac{cost_1}{R} \left( \frac{1}{T} - \frac{1}{T_{ref}} \right) + \frac{A}{R}\ln\frac{T}{T_{ref}} + \frac{B}{2R}(T - T_{ref}) + \frac{1}{2}\frac{C}{R}\left( \frac{1}{T^2} - \frac{1}{T_{ref}^2} \right)$$

$$\tag{2.21}$$

$$cost_1 = \Delta h^0(T_{ref}) - AT_{ref} - \frac{B}{2}T_{ref}^2 + \frac{C}{T_{ref}}$$

from which the equilibrium constant $K$ can be computed, as a function of temperature. The term $cost_1$ that compares in eq. (2.21) groups all the terms non dependent on $T$ that compare in eq. (2.20).

## 2.2.2 Formulae for magnesium carbonate decomposition (method B)

Substituting eq. (2.19) into eq. (2.15) and then in eq. (2.13), the enthalpy and the equilibrium constant of the reaction can be calculated with the following equations:

$$\Delta h^0(T) = \Delta h^0(T_{ref}) + \int_{Tref}^{T} A' + \frac{B'T'}{10^3} + C'\frac{T'^2}{10^6} + D'\frac{T'^3}{10^9} + E'\frac{10^6}{T'^2} dT'$$

$$= \Delta h^0(T_{ref}) + \left[ A'T' + \frac{B'T'^2}{2\cdot10^3} + \frac{C'T'^3}{3\cdot10^6} + \frac{D'T'^4}{4\cdot10^9} - \frac{10^6E'}{T'} \right]_{Tref}^{T}$$

$$\Delta h^0(T) = \Delta h^0(T_{ref}) + A'T - A'T_{ref} + \frac{B'T^2}{2\cdot10^3} - \frac{B'T_{ref}^2}{2\cdot10^3} + \frac{C'T^3}{3\cdot10^6} - \frac{C'T_{ref}^3}{3\cdot10^6} +$$

$$\frac{D'T^4}{4\cdot10^9} - \frac{D'T_{ref}^4}{4\cdot10^9} - \frac{10^6E'}{T} + \frac{10^6E'}{T_{ref}} \tag{2.22}$$

$$= cost_2 + A'T + \frac{B'T^2}{2\cdot10^3} + \frac{C'T^3}{3\cdot10^6} + \frac{D'T^4}{4\cdot10^9} - \frac{10^6E'}{T}$$

$$\ln\left[ \frac{K(T)}{K(T_{ref})} \right] = \int_{Tref}^{T} \frac{cost_2}{RT'^2} + \frac{A'}{RT'} + \frac{B'}{2\cdot10^3}\frac{1}{R} + \frac{C'T'}{3\cdot10^6}\frac{1}{R} + \frac{D'T'^2}{4\cdot10^9}\frac{1}{R} - \frac{10^6E'}{RT'^3} dT'$$

$$= \left[ -\frac{cost_2}{RT'} + \frac{A'}{R}\ln T' + \frac{B'T'}{2\cdot10^3R} + \frac{C'T'^2}{6\cdot10^6R} + \frac{D'T'^3}{12\cdot10^9R} + \frac{10^6E'}{2RT'^2} \right]_{Tref}^{T}$$

$$= -\frac{cost_2}{R}\left( \frac{1}{T} - \frac{1}{T_{ref}} \right) + \frac{A'}{R}\ln\frac{T}{T_{ref}} + \frac{B'(T - T_{ref})}{2\cdot10^3R} + \frac{C'(T^2 - T_{ref}^2)}{6\cdot10^6R} + \tag{2.23}$$

$$\frac{D'(T^3 - T_{ref}^3)}{12\cdot10^9R} + \frac{10^6E'}{2R}\left( \frac{1}{T^2} - \frac{1}{T_{ref}^2} \right)$$

In both the last two equations, the term $cost_2$ is:

$$cost_2 = \Delta h^0(T_{ref}) - A'T_{ref} - \frac{B'T_{ref}^2}{2\cdot10^3} - \frac{C'T_{ref}^3}{3\cdot10^6} - \frac{D'T_{ref}^4}{4\cdot10^9} + \frac{10^6E'}{T_{ref}} \tag{2.24}$$

and it groups all the terms non dependent on $T$ that compare in eq. (2.22).

## 2.3 Heat capacity, entropy, Gibbs free energy and enthalpy of formation data

The following tables summarize the data used for the calcium carbonate (tab 2.1), magnesium carbonate (tab 2.2) and dolomite (tab. 2.3) decompositions reactions.

**Table 2.1.** *Thermodynamic data used for the calcium carbonate decomposition evaluation; source Perry and Green (1997)*

|  | $c_p$ [J/mol*K] | | | $\Delta g^0_{form}$ (298K) | $\Delta h^0_{form}$ (298K) |
|---|---|---|---|---|---|
|  | a | b | c | [kJ/mol*K] | [kJ/mol] |
| $CaCO_3$ | 82.341 | 4.974e-2 | -1.287e6 | -1133.027 | -1211.268 |
| $CaO$ | 41.840 | 2.025e-2 | -0.452e6 | -603.751 | -634.713 |
| $CO_2$ | 43.263 | 1.146e-2 | -0.818e-6 | -394.384 | -393.514 |

**Table 2.2.** *Thermodynamic data used for the magnesium carbonate decomposition evaluation; source NIST-WebBook*

|  | $c_p$ [J/mol*K] | | | | | $s^0$ (298K) | $\Delta h^0_{form}$ (298K) |
|---|---|---|---|---|---|---|---|
|  | a' | b' | c' | d' | e' | [J/mol*K] | [kJ/mol] |
| $MgCO_3$ | 44.937 | 149.708 | -74.183 | 11.977 | -0.629 | 65.856 | -1111.689 |
| $MgO$ | 47.260 | 5.682 | -0.873 | 0.104 | -1.054 | 26.849 | -601.241 |
| $CO_2$ | 24.997 | 55.187 | -33.691 | 7.948 | -0.137 | 213.790 | -393.522 |

**Table 2.3.** *Thermodynamic data used for the dolomite decomposition evaluation; source Knacke et al. (1991)*

|  | $c_p$ [J/mol*K] | | | $s^0$ (298K) | $\Delta h^0_{form}$ (298K) |
|---|---|---|---|---|---|
|  | a | b | c | [J/mol*K] | [kJ/mol] |
| $CaMg(CO_3)_2$ | 155.226 | 80.333e-3 | -2.134e6 | 155.226 | -2327.894 |
| $CaCO_3$ | 104.516 | 21.924e-3 | -2.594e6 | 93.052 | -1208.856 |
| $CaO$ | 50.417 | 4.184e-3 | -0.849e6 | 38.212 | -635.089 |
| $MgO$ | 48.995 | 3.431e-3 | -1.134e6 | 26.941 | -601.701 |
| $CO_2$ | 51.128 | 4.368e-3 | -1.469e6 | 213.794 | -393.521 |

It is noticeable that Knacke et al. (1991) ensure the data validity up to the species decomposition temperature at atmospheric pressure.

## 2.4 Results

In this section the computed reaction standard Gibbs free energy changes, standard enthalpy changes and equilibrium constants of the decomposition reactions are presented. The obtained

results were compared with literature data in order to verify the temperature dependences $\Delta g^0(T)$, $\Delta h^0(T)$ and $K(T)$.

The standard Gibbs free energy changes of the decompositions were calculated with eq. (2.11) using the data previously tabulated (tab. 2.1, 2.2, 2.3). To verity the results computed for the $CaCO_3$ (fig. 2.1) decomposition, $\Delta g^0(T)$ was computed with Knacke et al. (1991) data by the formula (2.10) and with Stern (2001) data; for the $MgCO_3$ (fig. 2.2) decomposition, the comparison was performed with Stern (2001) (which refers to Knacke et al. (1991) for $MgCO_3$ and MgO data) and Chase (1998) values. For the calcite calculations, the reaction standard Gibbs free energy change is almost equivalent for the three sources (Stern (2001) values is $\approx 4$ kJ/mol less than Perry and Green (1997) and Knacke et al. (1991) is $\approx 2.5$ kJ/mol less; these differences tend to disappear at high $T$) and the temperature dependence is correct. For the magnesite calculations, Stern (2001) data are shifted ($\approx 15$ kJ/mol less) with respect to Chase (1998) data (remember that NIST refers to this source, Stern (2001) to Knacke et al. (1991) for $MgCO_3$ and MgO data). As far as dolomite (fig. 2.3 and 2.4), the computed results are compared with the data tabulated by Knacke et al. (1991) in order to verify the accuracy of the $\Delta g^0$ temperature dependence.

The standard enthalpy change of reactions were calculated with eq. (2.20) or (2.22) as previously explained. The comparisons for the $CaCO_3$ (fig. 2.5) and the $MgCO_3$ (fig. 2.6) decompositions were performed with Stern (2001) and Knacke et al. (1991) or Chase (1998) data. For the last two sources, $\Delta h^0(T)$ was calculated multiplying the compound enthalpy at temperature $T$ and 1 bar $h_i^0(T)$ by the corresponding stoichiometric coefficient:

$$\Delta h^0(T) = \sum_{i=1}^{nc} \nu_i h_i^0(T) \,. \tag{2.25}$$

The calcite decomposition reaction standard enthalpy change shows differences in the reference (at 298.15 K) value that affect the following data (Stern (2001) value is $\approx 4.5$ kJ/mol smaller than Perry and Green (1997) and Knacke et al. (1991) is $\approx 3$ kJ/mol smaller); this does not influence the correct temperature dependence. The same observations are valid for the magnesite decomposition as well (Stern (2001) data is $\approx 15$ kJ/mol smaller than Chase (1998) one). The dolomite decompositions standard enthalpy changes (fig. 2.7 and 2.8) match the Knacke et al. (1991) data, obtained multiplying the values of enthalpy $h_i^0(T)$ by the stoichiometric coefficient of the species involved in the reaction (eq. (2.25)).

The equilibrium constants were computed from the reaction standard enthalpy change, with eq. (2.21) or (2.23) depending on the reaction, and from the standard Gibbs free energy change, with eqs. (2.11) and (2.8). In figures from 2.9 to 2.12, the equilibrium thermal decomposition curves are plotted as $CO_2$ partial pressure versus $1/T$ because the reaction equilibrium constant is dependent on partial pressures of developed gases:

$$K(T) = a_{CO_2}^{\nu_{co2}} = \left[ \frac{f_{CO_2}(T, P, y_{CO_2})}{f_{CO_2}^{pure}(T, P_{ref})} \right]^{\nu_{co2}} = \left[ \frac{\phi_{CO_2} y_{CO_2} P}{P_{ref}} \right]^{\nu_{co2}} = \left[ \frac{\phi_{CO_2} P_{CO_2}}{P_{ref}} \right]^{\nu_{co2}}. \qquad (2.26)$$

Equation (2.26) derives from eq. (2.7) assuming that activities of solid species are equal to 1. For magnesite, calcite and dolomite full decompositions, the $CO_2$ fugacity $f_{CO2}$ is equivalent to the $CO_2$ partial pressure $P_{CO2}$ because the $CO_2$ fugacity coefficient $\phi_{co2}$ is approximately equal to 1 at the considered temperatures and pressures; as far as dolomite half decomposition at elevated temperatures the fugacity coefficient is no more equal to 1 and it is computed by:

$$\phi = \exp\left( \frac{BP}{RT} \right) \qquad (2.27)$$

based on the virial equation:

$$z = 1 + \frac{BP}{RT}. \qquad (2.28)$$

In the virial equation, $z$ is the compressibility factor and $B$ is the second virial coefficient and is a function of the reduced temperature $T_r = T / T_c$ (Elliott and Lira, 1999):

$$B = \left( B^0 + \omega B^1 \right) \frac{RT_c}{P_c} = \left[ 0.083 - 0.422 T_r^{-1.6} + \omega \left( 0.139 - 0.172 T_r^{-4.2} \right) \right] \frac{RT_c}{P_c}. \qquad (2.29)$$

In equation (2.29) $\omega$ (= 0.228) is the acentric factor and $T_c$ (= 304.2 K) and $P_c$ (= 72.8 atm) are the critical properties of the $CO_2$ (data from Bird, 2002).
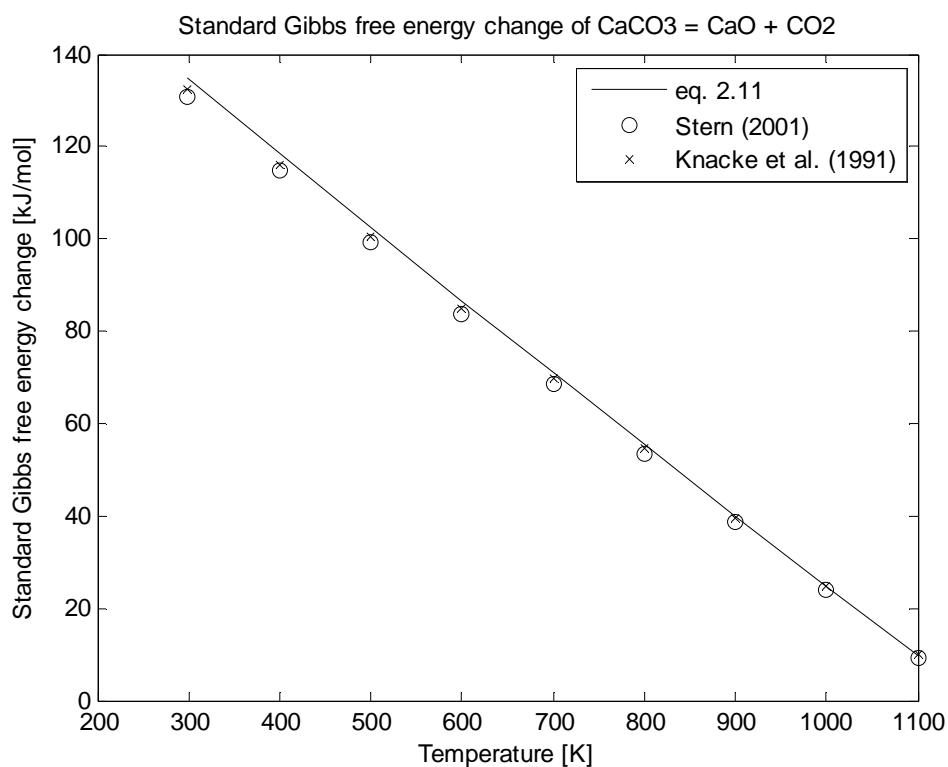
Therefore, for the dolomite full decomposition the stoichiometric coefficient of the gas is 2 and $P_{CO2} \phi_{CO2} / P_{ref} = \sqrt{K(T)}$; for all the other cases $\nu_{CO2} = 1$, therefore $P_{CO2} \phi_{CO2} / P_{ref} = K(T)$. For calcite decomposition (fig. 2.9) Stern (2001) and Knacke et al. (1991) data are plotted as well; the four series are congruent with each other despite the differences in the reaction standard enthalpy change at 298.15 K. In the plot there are also the experimental data of two authors: Baker (1962) and Harker and Tuttle (1955). Calculated values lie between these data and are in better agreement with the former series (25 degrees of difference at the same partial pressure of $CO_2$) than with the latter (50 degrees). For the magnesite, as already noticed, there is a difference between the computed values of the $\Delta h^0(T)$ and the Stern (2001) data of about 15 kJ/mol (this turn in a mismatch for the $\Delta g^0(T)$ as well). Such discrepancy affects the trends of equilibrium constants (fig. 2.10), namely the calculated $K(T)$ of $MgCO_3$ is different from the Stern (2001) one. The other three data series (calculated from $\Delta g^0(T)$, $\Delta h^0(T)$ and Chase (1998) ones) are in agreement and match also with Harker and Tuttle (1955) experimental data (10 degrees mismatch). This observation supports for Chase (1998) data correctness and for Stern (2001) unreliability about $MgCO_3$ information. For the dolomite decompositions

Knacke et al. (1991) data are available only for the half decomposition until 700 K, the decomposition temperature at atmospheric pressure. Additionally two series of experimental data were found only for the half decomposition: Graf and Goldsmith (1955) and Harker and Tuttle (1955). They match with each other and differ from the calculated values (fig. 2.12) of 80 degrees. When the temperature is larger than 1000 K this discrepancy increase (150 degrees) if the approximation $\phi_{CO2} = 1$ is used. Computing the correct value of the fugacity coefficient (black dotted line of fig. 2.12) the difference between experimental and calculated values is reduced (100 degrees). For the complete decomposition (fig. 2.11) the comparison is made with the equilibrium constant obtained using the tabulated data from Knacke et al. (1991) and eq. (2.10) and (2.8). In both cases the values are in agreement.

For the four reactions the resulting decomposition temperatures at atmospheric pressure are tabulated in tab 2.4; they are identified by the condition of $K(T) = 1$ considering the values of the equilibrium constants obtained from the standard enthalpy change of decomposition of each carbonate.

**Table 2.4.** *Calculated decomposition temperatures, identified by the condition K(T$_{dec}$)=1*

|                          | T$_{dec}$ [K] |
|--------------------------|---------------|
| Calcite (2.1)            | 1160          |
| Magnesite (2.2)          | 675           |
| Dolomite, complete (2.3) | 900           |
| Dolomite, half (2.4)     | 690           |

**Figure 2.1.** *Δg0(T) [kJ/mol] of the calcite decomposition: calculated value from Perry and Green (1997) data (solid line), Stern (2001) data (circles), Knacke et al. (1991) data (crosses)*
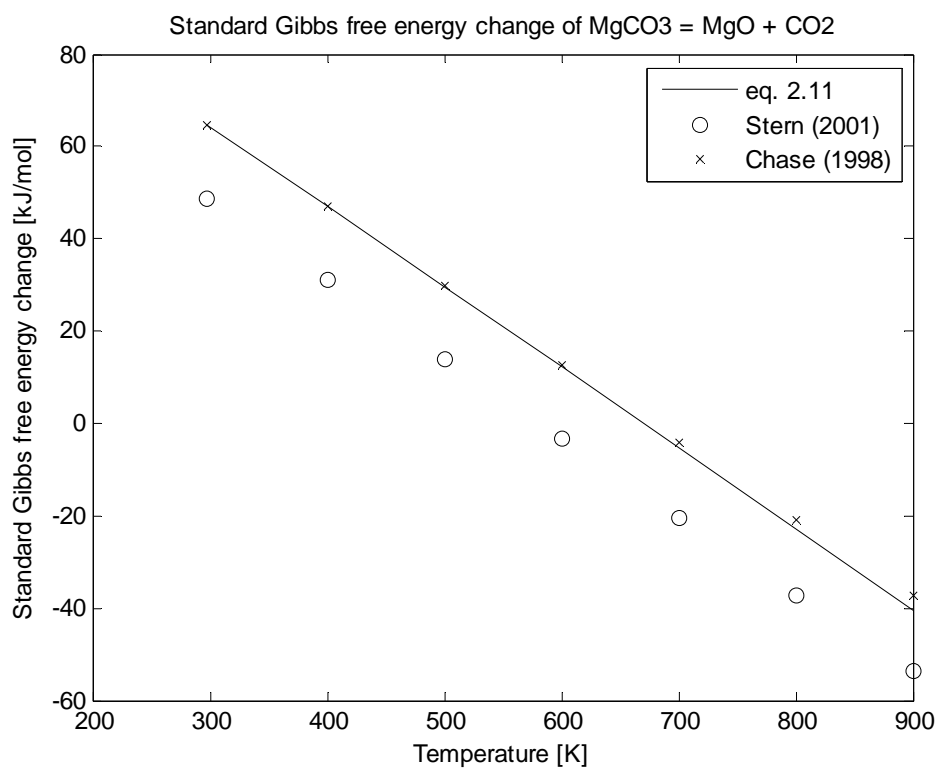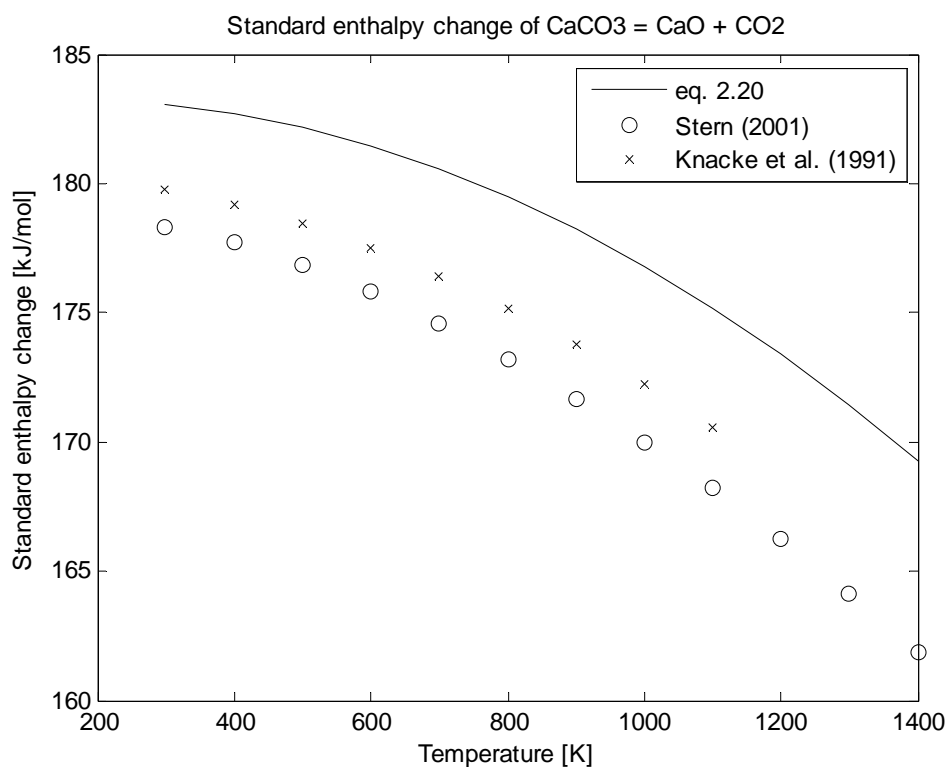


**Figure 2.2.** *Δg⁰(T) [kJ/mol] of the magnesite decomposition: calculated value from NIST-WebBook data (solid line), Stern (2001) data (circles), Chase (1998) data (crosses)*
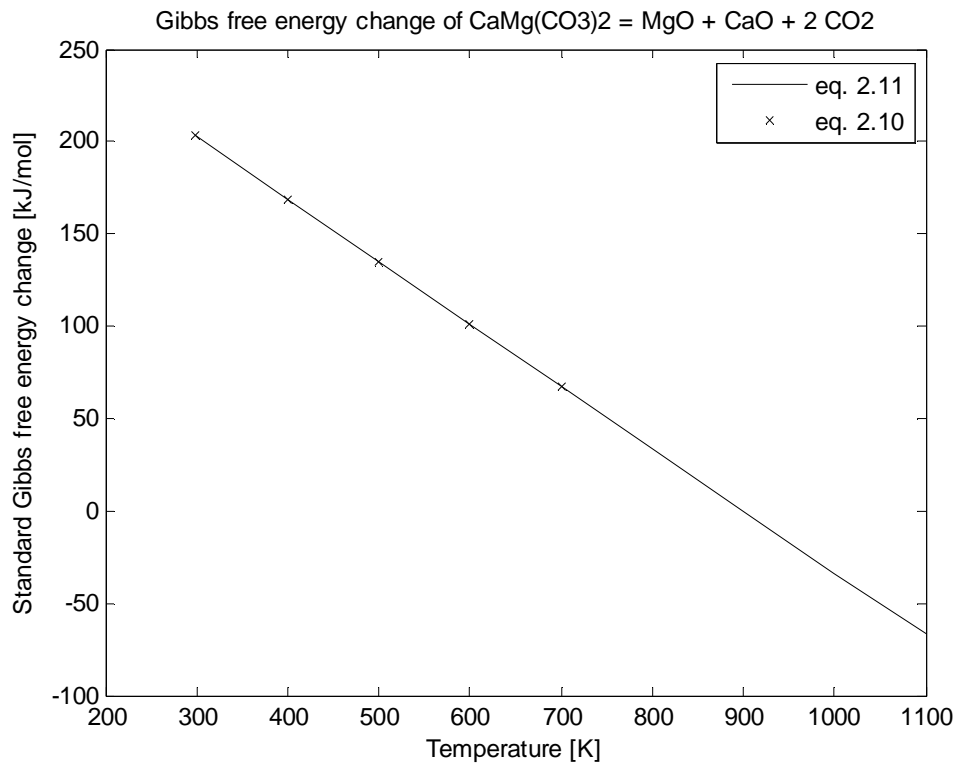
**Figure 2.3.** *Δg⁰(T) [kJ/mol] of the dolomite full decomposition: calculated value from Knacke et al. (1991) data by eq. 2.11 (solid line) and eq. 2.10 and 2.25 (crosses)*
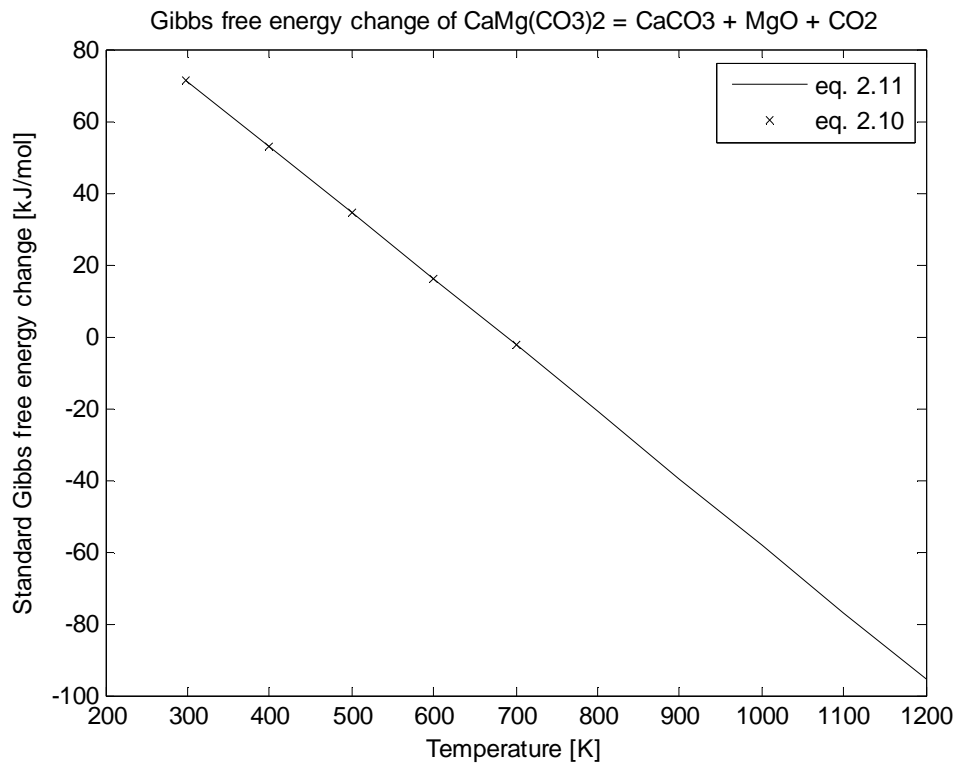


**Figure 2.4.** *Δg⁰(T) [kJ/mol] of the dolomite half decomposition: calculated value from Knacke et al. (1991) data by eq. 2.11 (solid line) and eq. 2.10 and 2.25 (crosses)*

**Figure 2.5.** *$\Delta h^0(T)$ [kJ/mol] of the calcite decomposition: calculated value from Perry and Green (1997) data (solid line), Stern (2001) data (circles), Knacke et al. (1991) data (crosses)*



**Figure 2.6.** *$\Delta h^0(T)$ [kJ/mol] of the magnesite decomposition: calculated value from NIST-WebBook data (solid line), Stern (2001) data (circles), Chase (1998) data (crosses)*
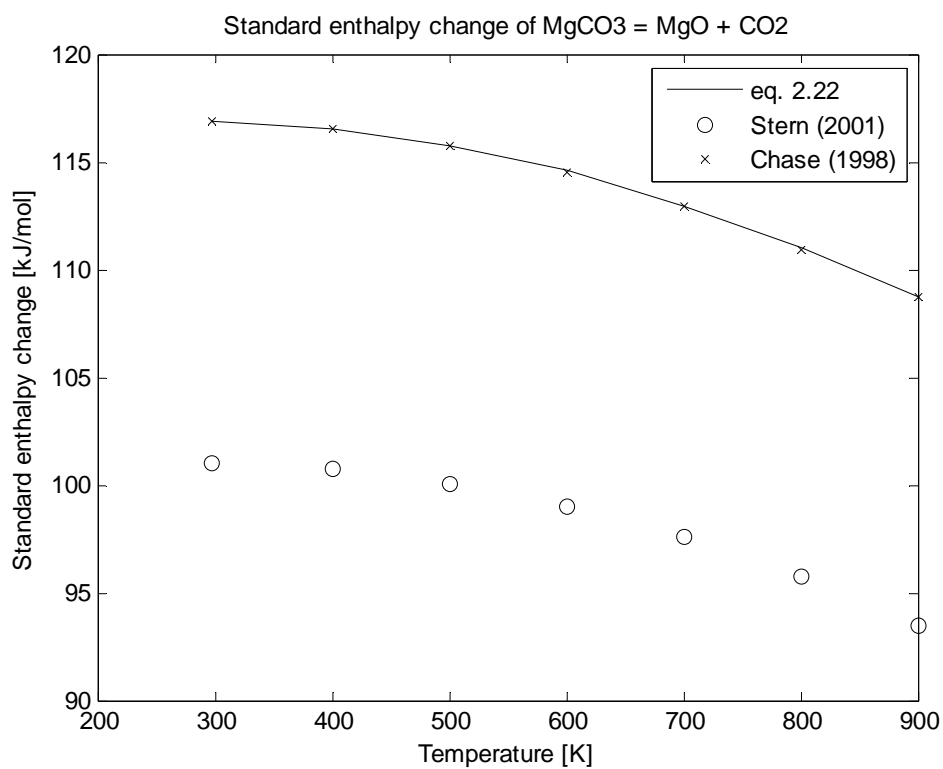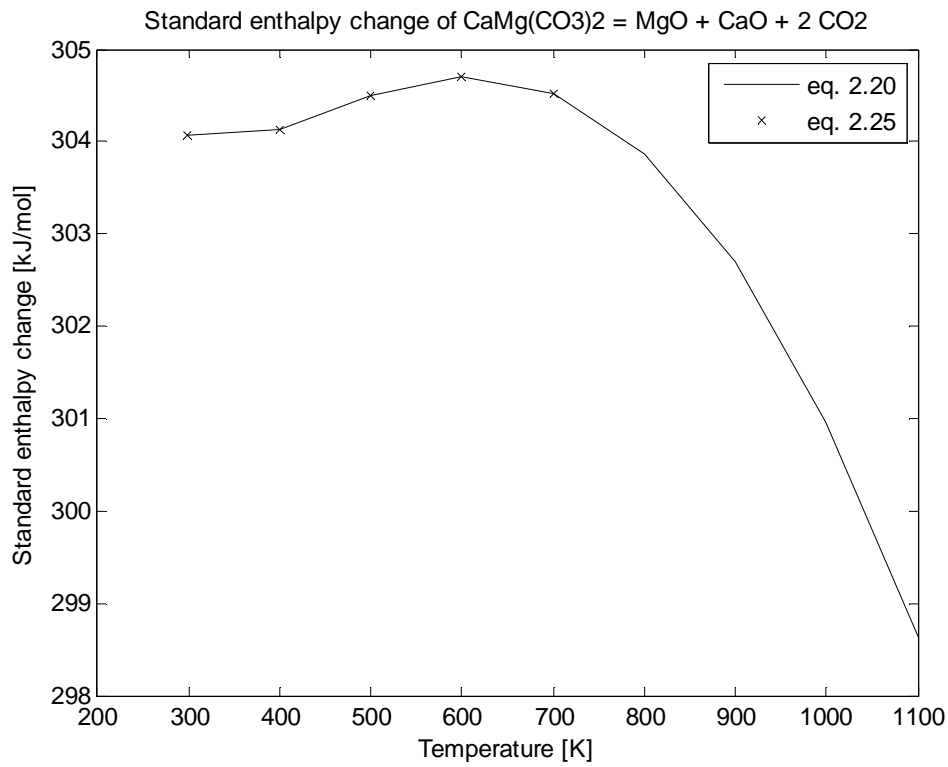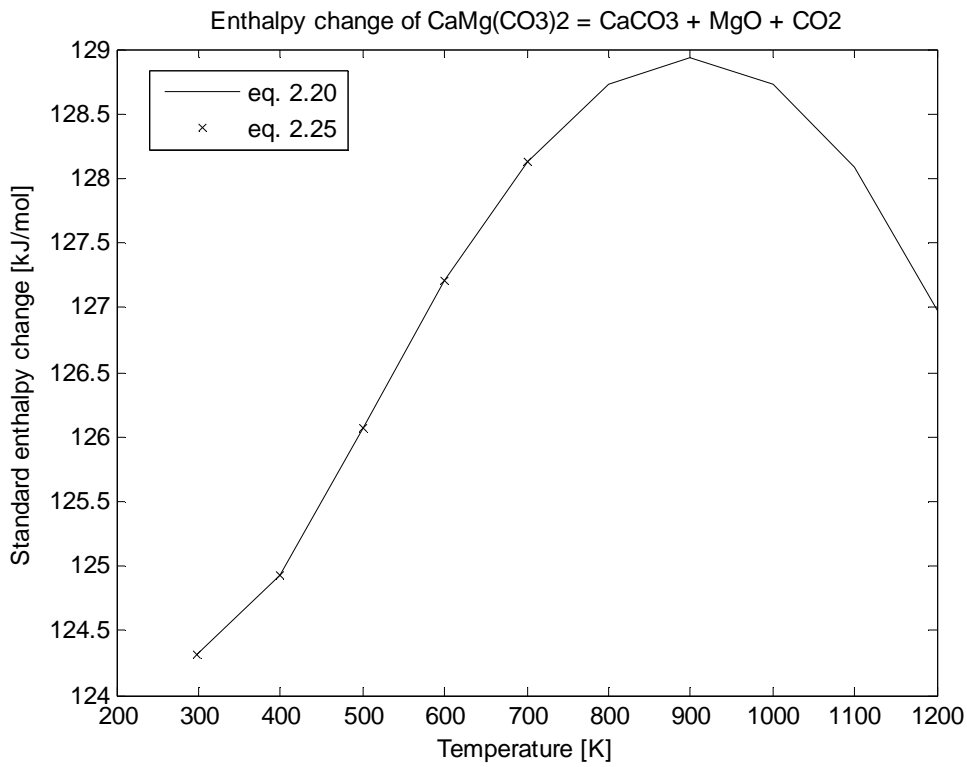
**Figure 2.7.** *$\Delta h^0(T)$ [kJ/mol] of the dolomite full decomposition: calculated value from Knacke et al. (1991) data by eq. 2.20 (solid line) and eq. 2.25 (crosses)*



**Figure 2.8.** *$\Delta h^0(T)$ [kJ/mol] of the dolomite half decomposition: calculated value from Knacke et al. (1991) data by eq. 2.20 (solid line) and eq. 2.25 (crosses)*
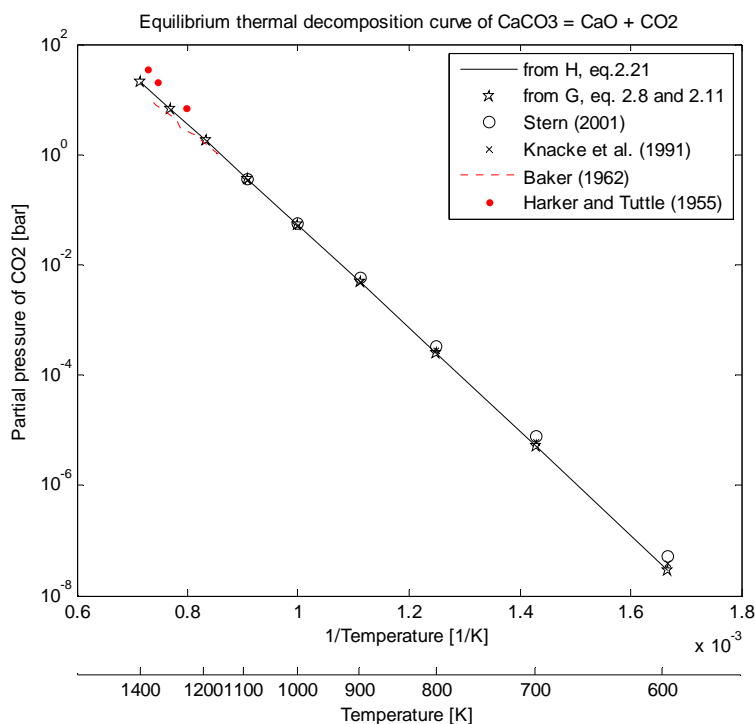
**Figure 2.9.** *K(T) of the calcite decomposition: calculated value from Perry and Green (1997) data (eq. 2.21: solid line; eq. 2.11: stars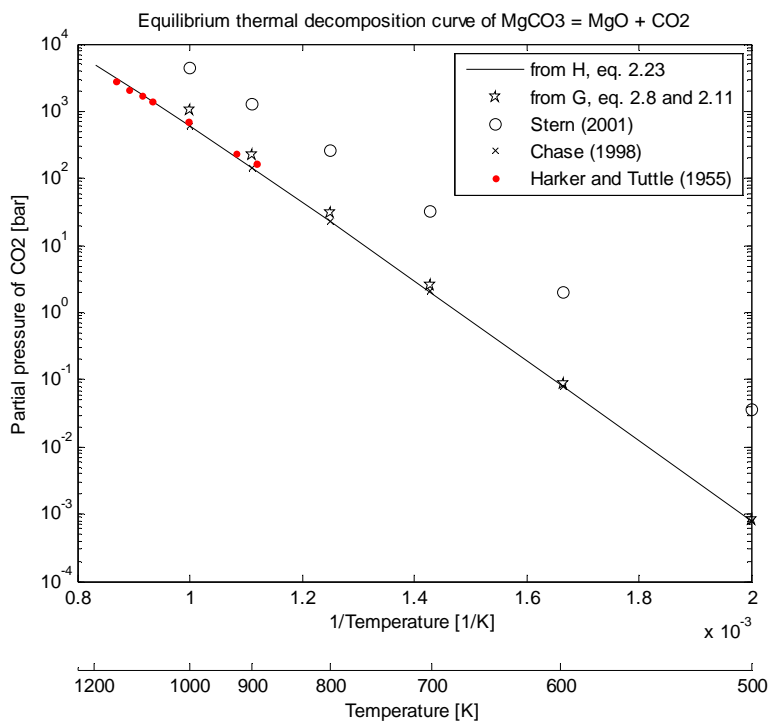), Stern (2001) data (circles), Knacke et al. (1991) data (crosses); experimental values from Baker (1962) (red dotted line) and Harker and Tuttle (1955) (red points)*



**Figure 2.10.** *K(T) of the magnesite decomposition: calculated value from NIST- WebBook data (eq. 2.23: solid line; eq. 2.11: stars), Stern (2001) data (circles), Chase (1998) data (crosses); experimental values from Harker and Tuttle (1955) (red points)*

**Figure 2.11.** *K(T) of the dolomite complete decomposition: calculated value from Knacke et al. (1991) data (eq. 2.21: solid line; eq. 2.11: circles; eq. 2.10 and 2.25: crosses)*
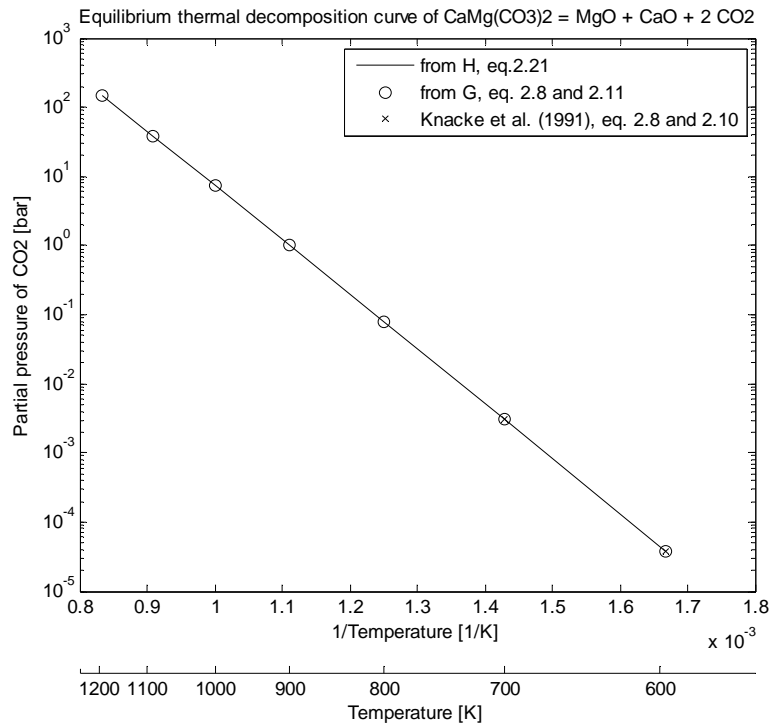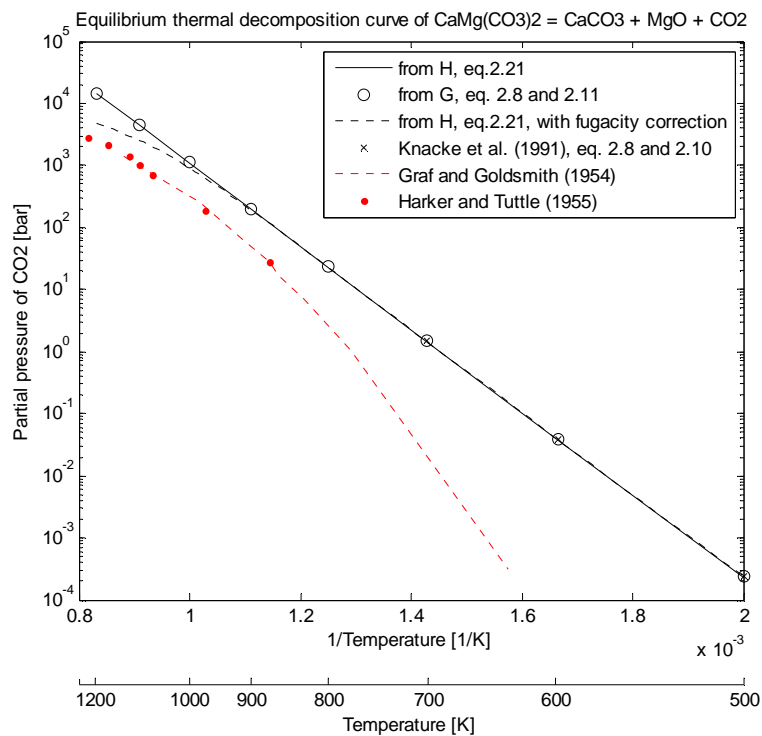


**Figure 2.12.** *K(T) of the dolomite half decomposition: calculated value from Knacke et al. (1991) data (eq. 2.21: solid line; eq. 2.11: circles; eq. 2.21 with correc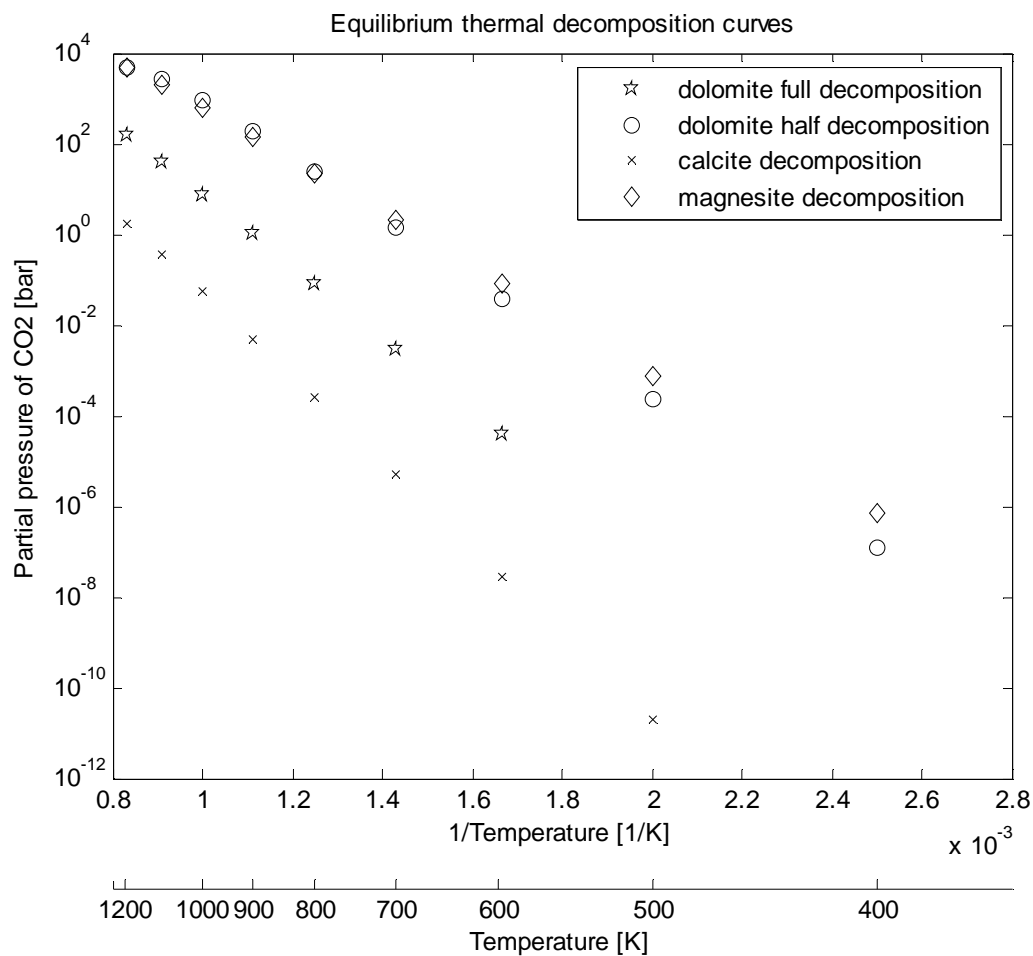tion for fugacity: black dotted lines; eq. 2.10 and 2.25: crosses); experimental values from Graf and Goldsmith (1954) (red dotted line) and Harker and Tuttle (1955) (red points)*

**Figure 2.13.** *Equilibrium thermal decomposition curves of dolomite (full: stars; half: circles), calcite (crosses) and magnesite (diamonds)*

The thermal decomposition curves (fig. 2.13) are useful to understand what material can be used at given temperature and pressure for the $CO_2$ absorption.

For example, at 1 bar and 400 K every decomposed carbonate (CaO, MgO, fully or half decomposed dolomite) can be used; if the operating temperature is 700 K the calcium oxide and the fully decomposed dolomite (CaO and MgO) can be used. At 20 bar and 400 K again every oxide can be used, but increasing the operating temperature to 800 K only CaO can be utilized and it can be obtained by calcite or dolomite fully decomposed (CaO and MgO).

## 2.5 Conclusions

From the analysis of the thermodynamics of the decomposition reactions and the comparison with literature data it is clear that the computed values from Perry and Green (1997) data of $\Delta g^0(T)$, $\Delta h^0(T)$ and $K(T)$ are acceptable in the case of calcite. Some differences are present in

the standard enthalpy and Gibbs free energy change of formation of the different sources but they do not affect significantly the computed values, in particular the equilibrium constants.

For the magnesite decomposition, the Chase (1998) data are in agreement with experimental data (Harker and Tuttle, 1955), instead Stern (2001) values are not in agreement because of the difference of the $MgCO_3$ standard enthalpy of formation.

As far as dolomite decompositions, only one source for the thermodynamic quantities was found, namely Knacke et al. (1991). In the case of the dolomite half decomposition, the calculated values of equilibrium constants differ significantly from the experimental data of Graf and Goldsmith (1955) and of Harker and Tuttle (1955), even when the corrected fugacity coefficient was used. It is possible that the disagreement is caused by the dolomite formation enthalpy and entropy values (as in the case of magnesium carbonate) but no other literature data to confirm the ones used were found.

It is worthy to note that no experimental data for the dolomite complete decomposition were found thus it was not possible to check the accuracy of the computed $\Delta g^0(T)$, $\Delta h^0(T)$ and $K(T)$.

# Chapter 3

# Thermogravimetric analysis of calcite/dolomite calcination and carbonation reactions

Process simulations of the carbon dioxide capture require estimates of the carbon dioxide absorption/desorption kinetics. These data can be obtained by thermogravimetric analysis. Additionally, in the carbon dioxide capture regenerative processes, the sorbent is continually cycled between the carbonation and calcination stages, but its capture capacity decreases upon cycling. Theoretically, it should be possible to improve the sorbent performance by modifying the conditions of calcination and carbonation step. This chapter presents thermogravimetric measurements of the sorbent thermal decompositions and absorption reaction; the obtained results are compared with literature data.

## 3.1 Introduction

In carbon dioxide capture regenerative processes the sorbent is cycled between the absorber and the regenerator reactors. However, their maximum carbonation conversion (the ratio of moles of carbonate produced over the initial moles of Ca/Mg oxide) or sorption capacity decreases upon $CO_2$ capture and release cycles.

Dean et al. (2011) report that the loss of sorbent reactivity can be caused by a number of factors, the most important of which is sintering of the porous metal oxide during the high temperature calcination stage. Metal oxides formed by calcination are very porous because there is a marked reduction in molar volume during the decomposition from the carbonate to the oxide form.

The sintering is characterized by changes in pore shape and grain growth, which causes a reduction in the reactive surface area and a drop-off of the sorbent reactivity. This phenomenon is caused by high temperatures but there is also a contribution due to reactive sintering specific of cycling experiments. The sorbent reactivity can decrease also because of the loss of bed material due to attrition, that causes elutriation of fines.

Therefore, the sorbent reactivity and mechanical stability are critical factors in the selection of the sorbents. Ultimately, the implementation of regenerative calcium/magnesium based

sorbents for $CO_2$ removal is possible, but such processes could be economically viable on industrial scale if highly durable, reactive and mechanically strong sorbents with elevated $CO_2$ sorption capacity will be developed.

As discussed by Dean et al. (2011), improving sorbent performance upon cycling can be done by sorbent enhancement or by alteration of the process conditions. In the first case, the typical used technique is solid doping, obtained by impregnation with catalytic agents, in particular with traces of inorganic salts. The second option is related to the sorbent regeneration process: modifying the regeneration conditions, namely decreasing the calcination temperature (reducing the $CO_2$ partial pressure) or changing the residence time at high temperatures. An experimental investigation of the sorbent calcinations based on the thermo-gravimetric analysis can be useful to identify optimal regeneration conditions.

In §3.2 the results of the experiments on the calcite/dolomite thermal decompositions are presented; more specifically, thermal-gravimetric analysis (TGA) was used to investigate the thermal decomposition. These experiments were performed to reproduce some experimental data available in literature, namely to verify the values of full decomposition temperature, time and the degree of carbonate conversion. In fact, in literature these two materials show a moderate variance in the values of these properties; the reason is that the decomposition rate depends on parameters such as the amount and the purity of the sample, the particle size, the type of the crystalline structure, the heating rate, the temperature range considered, the atmosphere at which the calcination is carried out, etc. (Wang and Thomson, 1995; Gallagher and Johnson, 1973; Samtani et al., 2002; Galan et al., 2012; Wilburn et al., 1991; Romero Salvador, 1989). In addition, the carbonate decomposition is influenced by the heat and mass transfer resistances (Wang and Thomson, 1995; Gallagher and Johnson, 1973; Wilburn et al., 1991; Gallagher and Johnson, 1976; Satterfield and Feakes, 1959). The heat transfer from the surface of the grain through the layer of reactants and products up to the interface of reaction controls the achievement of the decomposition temperature in the inner portion of the particle, while the mass transfer of the released $CO_2$, which moves away from the reaction zone through the particle itself via a diffusion mechanism, is related to the local value of the $CO_2$ partial pressure that affects the kinetics of thermal decomposition. The problems related to the transport resistances, which affect the thermogravimetric analysis, are discussed in §3.4. In this work of thesis it is important to consider them because the kinetics in circulating fluidized bed reactors (which will be considered in the process simulations of Chapter 4) is not significantly influenced by heat/mass transfer resistances. Therefore, the TGA data do not reproduce correctly the kinetics in CFBs.

In §3.3 the results of the TGA experiments on the carbon dioxide absorption by calcium oxide are presented. These experiments were performed to reproduce some experimental data available in literature, namely to verify the TGA data obtained by Grasa et al. (2008).

## 3.2 Thermo-gravimetric analyses of calcite/dolomite calcinations

A widely approach described in the scientific literature in the investigation of the thermal decomposition reactions is represented by thermo-gravimetric analysis (TGA), differential thermo-gravimetry (DTG) and differential thermal analysis (DTA); the tests described in this section belong to the first group. In thermo-gravimetric analyses the material samples are introduced in a reactor chamber with a controlled atmosphere, the temperature program is planned and the resulting changes in weight are registered. Through the observation of the derivative weight loss curve it is possible to identify the points where the weight loss are complete (when complete release of stoichiometric $CO_2$ is achieved) and then obtain information about the maximum temperature at which the carbonates are totally decomposed at a fixed heating rate, and the time required to observe the total decomposition at a fixed temperature.

As already mentioned, many authors underline the factors that can affect the decomposition rate. As far as TG experiments on calcite, Galan et al. (2012) distinguish between intrinsic and extrinsic factors that influence the decomposition. Intrinsic factors include chemical purity and defects content of the carbonate, solid surface area, particle size and/or crystallite size, morphology, etc.. Extrinsic factors are the sample packing in the holder (i.e. sample quantity), flow rate of the sweeping gas which influences the gas interchange between furnace/cell atmosphere and the sample, the gaseous environment in which the reaction is carried out, severity of the thermal gradient developed in the sample that is correlated to the decomposition temperature range and the heating rate, etc..

During the conducted TG tests, two operating variable were modify to evaluate how they affect the decomposition behavior: the purge gas flow rate and the heating rate.

### 3.2.1 Effect of purge gas flow rate

The effect of the purge gas flow rate of the purge gas on the calcite decomposition was investigated performing tests at the same heating rate of 10°C/min with 15 mg samples of high purity $CaCO_3$ (> 99%) provided by Sigma-Aldrich (C6763) with a particle size distribution around 10 µm.

Two DTG test were conducted to verify the decomposition temperature dependence on the purge gas flow rate. The experiments were performed with air, but the first one was performed at a 70 cm$^3$/min flow rate while the second at 23 cm$^3$/min (Fig. 3.1).
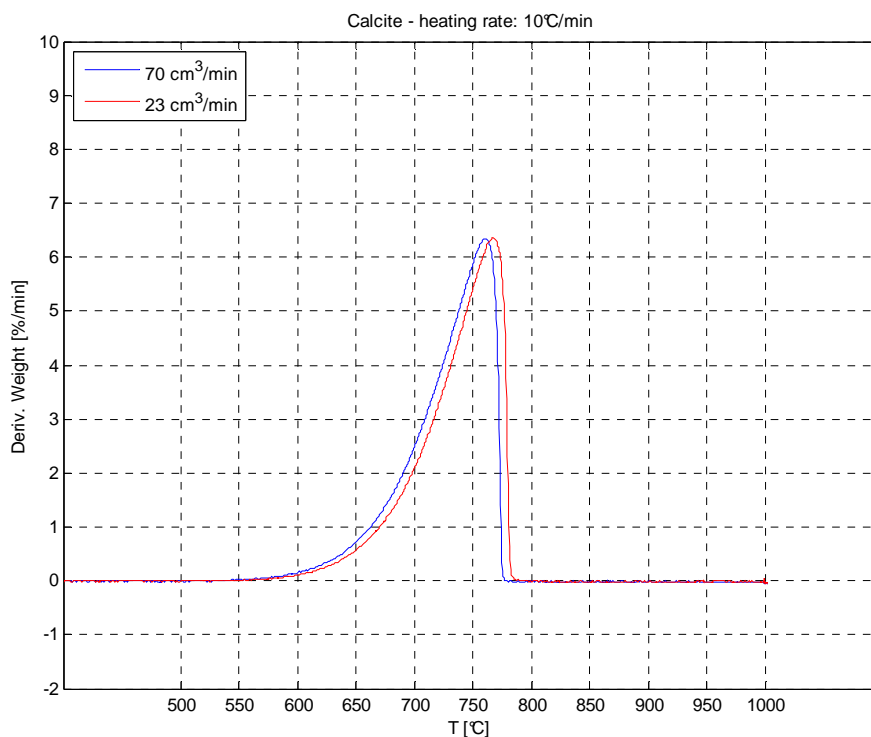
**Figure 3.1.** *DTG analysis: derivative weight loss vs. temperature of $CaCO_3$ calcined in air at a heating rate of 10°C/min with purge flow rate of 70 $cm^3$/min (blue line) or 23 $cm^3$/min (red line) (sample size: 15 mg, particle diameter: 10 μm)*

The purge gas influences the ambient conditions, namely it determines if the environment around the sample is inert or not: the purge gas is used to quickly remove the product gas from the decomposing sample and to ensure that there is no reaction between the gaseous products and the gases that compose the environment (Samtani et al., 2002). Therefore, if the purge gas flow rate is adequate, the purge gas flushes away the $CO_2$ produced during the decomposition, maintaining a very low partial pressure of carbon dioxide in the sample crucible and hence making the $CO_2$ influence on the thermal decomposition of the carbonate negligible. On the contrary, for low values of purge gas velocities, the sample is affected by the increasing $CO_2$ partial pressure in its surroundings and hence the corresponding decomposition temperature peak is shifted towards higher temperature. In Figure 3.1, the lower flow rate leads to a 10°C increment in the decomposition temperature (from 770 to 780°C), which corresponds to a time delay of about 2 min in the achievement of the full decomposition, considered negligible in first approximation. The trend of the experimental test of Figure 3.1 supports the interpretation given by Samtani et al. (2002): performing TG experiment at three different typical values gas purge flow rate (25, 50, 100 mL/min), it is expected that the flow rate of the purge gas does not affect the decomposition reaction and it should not influence the DTG curve shape as well.

### 3.2.2 Effect of the heating rate

The effect of the heating rate on carbonate decompositions was investigated by many authors, in nitrogen or in mixed $N_2$-$CO_2$ atmospheres, concluding that increasing this parameter the decompositions of calcite and dolomite occur at higher temperatures (Gallagher and Johnson, 1973; Galan et al., 2012; Samtani et al., 2001 and 2002).

In this work, the effect of the heating rate on the calcium carbonate decomposition was investigated carrying out experiments in air, with a gas flow rate value of 70 $cm^3$/min, at three different heating rates: 2, 10 and 15°C/min. The material used is commercial $CaCO_3$ powder provided by Sigma-Aldrich (C6763) with 99% purity and particle size distribution of 10 µm in diameter. All the tests were performed loading in the TG crucible samples of about 15 mg.

The obtained results agree with those available in literature: as mentioned by Galan et al. (2012), modifying the heating rates leads to a shift in the temperature range where the calcium carbonate decomposition occurs, namely, when the heating rate increases, the decomposition occurs at higher temperatures (Fig. 3.2) and is accelerated in terms of time (Fig. 3.3).

DTG plots are more sensitive to sample weight changes compared to TGA ones, therefore this type of graph is more precise to identify the effect of the heating rate on the temperature decomposition. Calcium carbonate thermally decomposes to give CaO (solid) and $CO_2$ (gas) according to the reversible stoichiometric reaction (eq. 2.1). The molecular weights of the involved species are 100 g/mol for $CaCO_3$, 56 g/mol for CaO and 44 g/mol for $CO_2$. The complete conversion of the carbonate occurs when a weight loss equal to 44% of the mass fraction (corresponding to the stoichiometric amount of $CO_2$ in $CaCO_3$) is recorded, or similarly, when the final mass percentage is equal to the CaO/$CaCO_3$ ratio of 0.56. Different results are indications of the presence of impurities in the sample. The used material is high purity and the obtained results confirm the achievement of the complete $CaCO_3$ decomposition, or the achievement of stoichiometric $CO_2$ loss, in agreement with the theoretical considerations.

However, the graph of Figure 3.3 present an anomalous aspect: the TG curves seem to be affected by a drift after the achievement of the sample complete decomposition and before the beginning of the calcium carbonate conversion (in particular for the test at heating rate of 2°C/min). This unexpected increase in sample weight can be explained by the fact that there are a number of sources of error in TGA which can lead to inaccuracies in the recording of temperature/time and mass data.

A common source of error during TG experiments is due to the buoyancy effect. When a thermally inert crucible is heated when empty (or partially loaded) there is usually an apparent weight change as the temperature increases which is due to the effect of change in the buoyancy of the gas in the sample environment: the density of the gas within the sample surrounding decreases during the heating and this typically results in an apparent gain in the
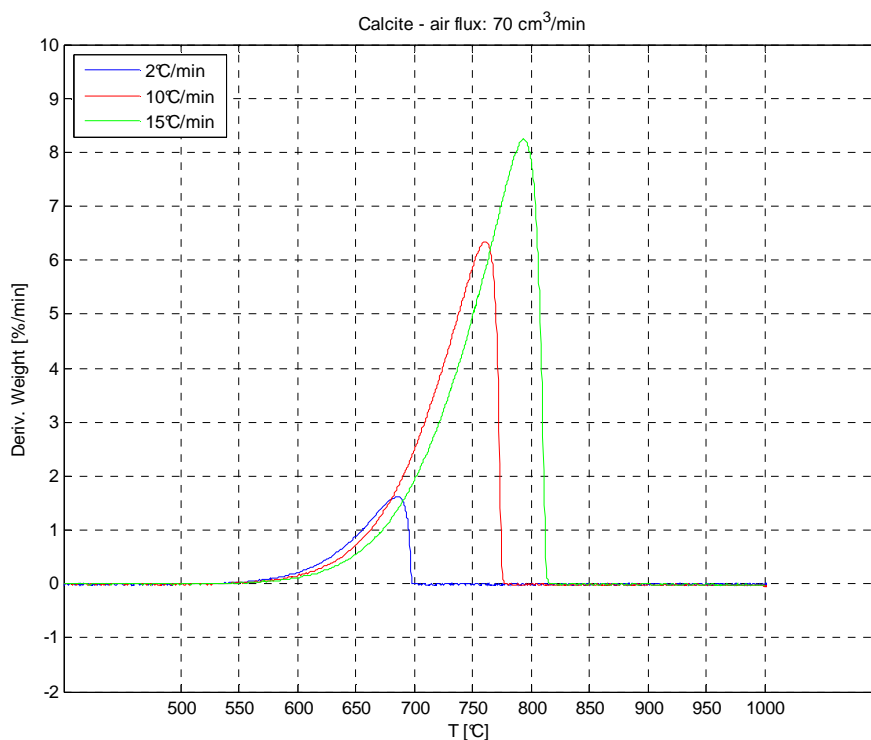
**Figure 3.2.** *DTG analysis: derivative weight loss vs. temperature of $CaCO_3$ calcined in air at a heating rate of 2 (blue line), 10 (red line) and 15°C/min (green line) with purge flow rate of 70 $cm^3$/min (sample size: 15 mg, particle diameter: 10 µm)*
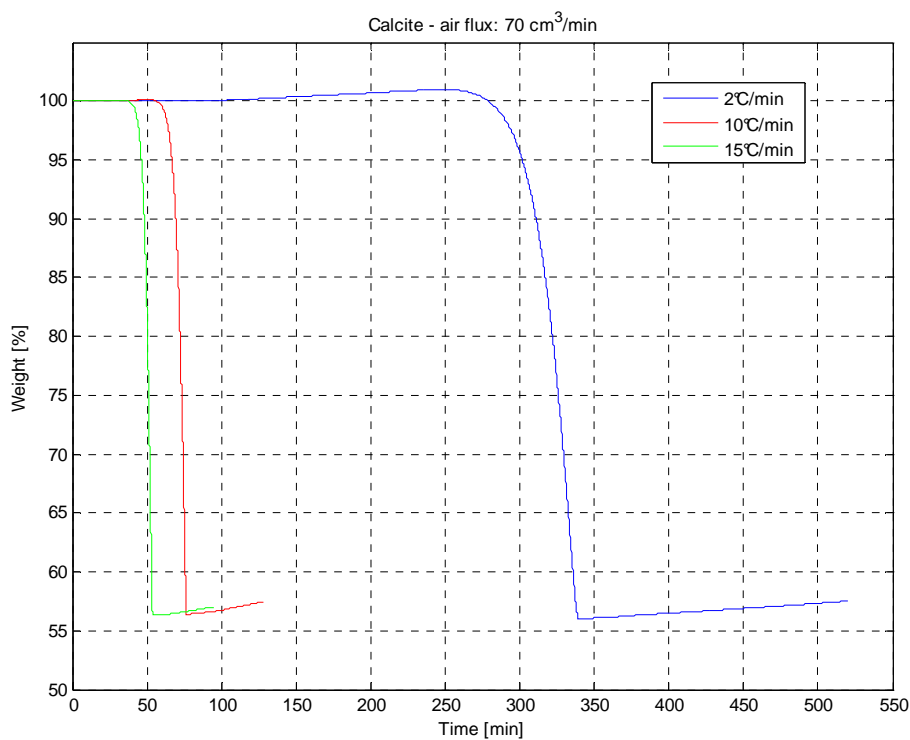


**Figure 3.3.** *TG analysis: weight loss vs. time of $CaCO_3$ calcined in air at a heating rate of 2 (blue line), 10 (red line) and 15°C/min (green line) with purge flow rate of 70 $cm^3$/min (sample size: 15 mg, particle diameter: 10 µm)*

sample weight. These effects are reproducible and hence the TG curve can be corrected by a blank curve, performed at the same conditions but with an empty crucible, that can be subtracted to the sample one.

The values of the sample weight (as % over the initial mass) after the complete decomposition of calcium carbonate, the corresponding calcination temperatures and the times required to obtain the complete decomposition are summarized in Table 3.1. The full decomposition temperature, or time, is defined as the value at which the maximum in derivative weight versus temperature curve (Fig. 3.2) and the minimum in weight loss versus time (Fig. 3.3) curve is observed.

**Table 3.1.** *Values of final weight of sample (%), decomposition temperature (°C) and time (min) required for the CaCO₃ calcinations in TG analysis*

| Heating rate [°C/min] | Decomposed sample weight [wt %] | T [°C] | Time [min] |
|:---:|:---:|:---:|:---:|
| 2 | 56.0025 | 698.67 | 339.70 |
| 10 | 56.4014 | 777.39 | 76.78 |
| 15 | 56.3197 | 821.39 | 54.29 |

When increasing the heating rate from 2°C/min to 15°C/min, the time required to obtain the complete decomposition of CaCO$_3$ reduces from about 5 hr up to approximately 50 min. On the other hand, at 15°C/min the temperature has to increase of more than 100°C in order to observe the complete calcination of the sample.

### 3.2.3 Comparison with literature data

An overview of the scientific literature highlights how the investigation of the thermal decomposition of calcite and dolomite, in particular the investigation of their kinetics, is a highly complex and frequently controversial subject. Differing shapes are reported for DTA and TG curves and this is reflected on differing values of the decomposition temperatures, of the degree of conversion and of the kinetic parameters as well. Several authors (Wang and Thomson, 1995; Galan et al., 2012; Wilburn et al., 1991; Romero Salvador, 1989) suggest that these differences are due in part to the choice of equipment and operating conditions (atmosphere, heating rate, sample size, etc.), in part to the sample properties, namely crystalline states of the precursor calcium carbonate/dolomite and particle size of the sample powder.

Despite the same operating conditions in terms of heating rates (10°C/min) and furnace/cell atmosphere (air or N$_2$), samples of approximately 10 mg constituted by optical quality calcite single crystals (Iceland Spar) of about 2x2x1 mm in size (Rodriguez-Navarro et al., 2009)

give a different decomposition trend compared to those of 100 mg of commercial $CaCO_3$ powder with particle size of few tens of µm (Galan et al., 2012). As reported by Rodriguez-Navarro et al. (2009) the conversion for calcite single crystal starts at approximately 600°C and is completed at about 850°C while for Galan et al. (2012) calcium carbonate begins to decompose around 700°C and reaches the theoretical stoichiometric loss of $CO_2$ at temperatures higher than 900°C. Similarly, this happens also for dolomite. At heating rate of 10°C/min, it is reported (Rodriguez-Navarro et al., 2012) that samples of approximately 10 mg constituted by optical quality dolomite single crystals of about 2x2x1 mm in size start to decompose at approximately 500°C with an initial slow rate up to approximately 750°C beyond which, the conversion reaches the stoichiometric values (at approximately 900°C) with a faster, nearly constant decomposition rate. Instead samples of grounded rock dolomite (amount of approx. 14-20 mg) with grain size of approximately 80 µm start to decompose again at approximately 500°C but reach the full decomposition at temperatures lower than 800°C (Gallagher and Johnson, 1973; Samtani et al., 2002).

These discrepancies arise from the fact that the sample amount and the grain size strongly affect the calcite/dolomite decomposition. Wilburn et al. (1991) observed that when the sample mass is increased, the peak temperature in DTG plots increases, suggesting that the larger the sample mass, the higher the decomposition temperature or, similarly, the higher the time at which the full-decomposition is measured. Instead, when the particle size of the sample is reduced, the DTG peak temperatures decrease. Satterfield and Feakes (1959) also report that calcium carbonate with a small particle size (approximately 0.2 µm) decomposes, even at high rates, at reaction temperatures and $CO_2$ partial pressure approximating those of equilibrium, while $CaCO_3$ samples with bigger particle size (about 10-15 µm) require temperatures in excess of equilibrium.

In order to gain sensibility on the decomposition of these carbonates, in terms of decomposition temperature and time required, classical TGA experiments were carried out in atmosphere of air (gas flow rate of 70 cm$^3$/min) with samples of approximately 15 mg and heating rate of 10°C/min. As previously indicated, the calcite samples were high purity $CaCO_3$ (>99%) provided by Sigma-Aldrich (C6763), with a particle size distribution of approximately 10 µm. The dolomite samples, instead, were provided by UniCalce S.p.A and consisted of powder with particle size up to 300 µm (more than 50% in weight is below 70 µm).

Figure 3.4 shows the comparison between the decomposition trend of calcium carbonate (in blue) and of dolomite (in red). It can be observed that the $CaCO_3$ decomposition starts at ~ 600°C, as reported in Rodriguez-Navarro et al. (2009), but finishes at a temperature lower than 800°C, almost 100°C less compared to the full decomposition temperature recorded by Rodriguez-Navarro et al. (2009). However, it must be underlined that the particle size of the samples used by Rodriguez-Navarro et al. (2009) was different from those utilized in our

experiments (namely, single crystals of few mm against powder with diameter of about 10 µm).

Therefore, considering what mentioned previously about the effect of the particle size on the thermal decomposition, it can be reasonably to assume this aspect as the source of the differences measured. In fact, the TGA curve proposed by Gunasekaran et al. (2007), in which the sample used was characterized by particle diameter of approximately 50 µm, reveals that the thermal decomposition of calcium carbonate in a $N_2$ atmosphere starts at approximately 600°C and ends near 850°C, namely at a temperature value at midway between the measurements by Rodriguez et al. (2009) and our result.
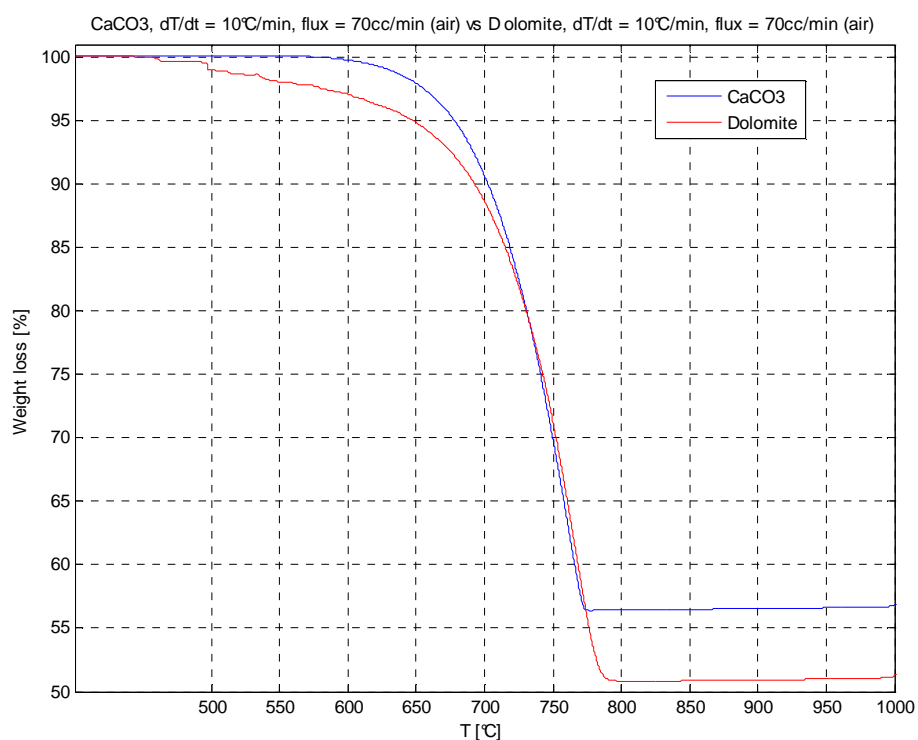


**Figure 3.4.** *Comparison between TGA curves (weight loss vs. temperature) of calcite (blue line) and dolomite (red line) obtained with a air flowrate equal to 70 cm³/min, 10°C/min heating rate and 15 mg samples*

Concerning the dolomite thermal behaviour, in our case the material seems to begin decomposing initially at a temperature lower than 500°C, while the full decomposition is at approximately 800°C, substantially in line with the values measured by Samtani et al. (2002). However, the sample weight change (i.e. the degree of conversion) recorded is slightly higher than the theoretical stoichiometric value expected. As for as the calcite decomposition discussed previously (§3.2.2), according to the stoichiometric full decomposition reaction (2.3), the evaluation of the molecular weight for each species involved suggests that the complete conversion of dolomite occurs when a weight loss of 47.7% is recorded. This value

corresponds to the stoichiometric amount of $CO_2$ in $CaMg(CO_3)_2$. This result can be explained considering the phenomenon that characterizes the dolomite decomposition known as decrepitation, which emerges from the DTG curves shown in Figure 3.5.
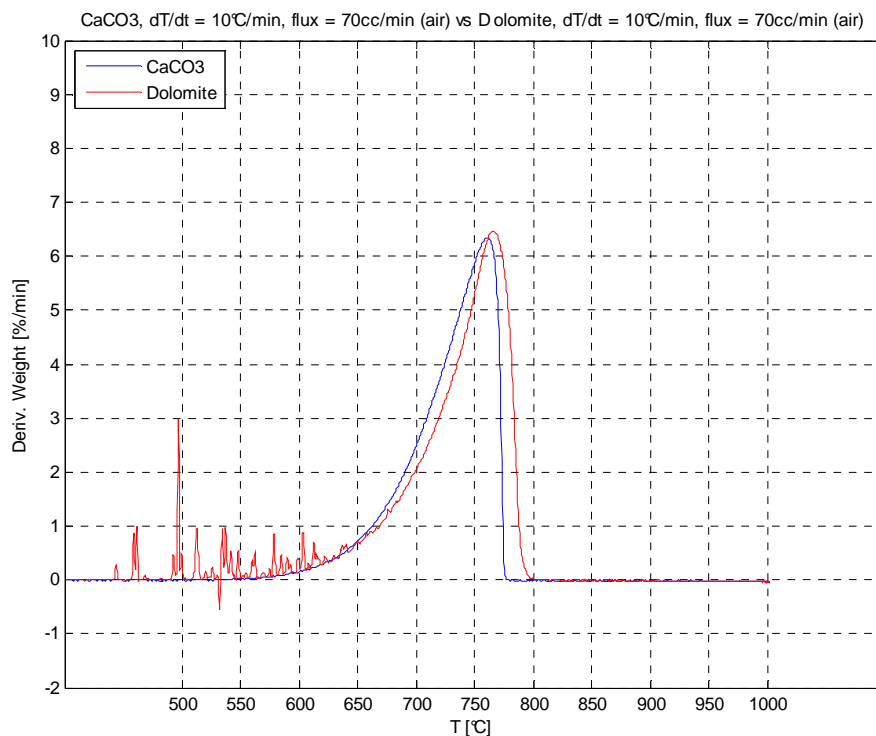


**Figure 3.5.** *Comparison between DTG curves (derivative weight loss vs. temperature) of calcite (blue line) and dolomite (red line) obtained with air flowrate of 70 cm³/mine, 10°C/min heating rate and 15 mg samples*

Decrepitation is a process cited by several authors (Rodriguez-Navarro et al., 2009; Samtani et al., 2001) and consists on the breaking of crystals as a result of the temperature increase, which produces the ejection of tiny fragments and a characteristic crackling. The ejection of the fragments determines the scattering of the weight change peaks recorded in the DTG diagram. It is the result of the pressure increase of the water molecules incorporated within the lattice structure of the dolomite during the formation of the mineral: the temperature increase in the calcination step induces the evaporation of these molecules with the consequent localized pressure increase. In the locations where the pressure exceeds the mechanical strength of the solid grains, it is possible to observe the characteristic mini explosions associated with the pressure release from the particles. Samtani et al. (2001) observe the decrepitation for samples of intermediate particle size (between 100 and 650 µm), with the maximum degree for grains in the range between 110 and 350 µm. On the contrary, in the case of particles larger than 850 µm, the release of pressure is not sufficient to overcome the cohesive forces of the solid molecules, while for particles of size lower than

100 µm, the incidence of the phenomenon is not sufficient to cause destabilization within the grains. The authors add that it is usually registered in the temperature range between 500 and 700°C. In Figure 3.5, this process is effectively recorded as a series of peaks on the dolomite DTG curve (in red); however, there is a variation in the typical temperature range of the decrepitation (500-700°C), with a shift of about 50°C towards lower temperatures (450-650°C). This discrepancy is probably due to the different nature/precursor of the dolomite.

Finally, it is noticeable that, according to Samtani et al. (2001), performing TG experiments in an inert atmosphere of air or nitrogen, the decomposition and the decrepitation overlap making difficult to follow the thermal decomposition behaviour of dolomite samples. This problem is avoided when the experiments are conducted in an atmosphere of $CO_2$ where the higher partial pressure of carbon dioxide leads to an increase in the dolomite decomposition temperature; in this way the decrepitation and the decomposition stages are segregated allowing a clear distinction between the two phenomena.

## 3.3 Thermo-gravimetric analyses of CaO carbonation

A second set of experiments was performed to obtain information concerning the absorption reaction rate of $CO_2$ on CaO previously obtained by thermal decomposition treatment. In particular, the goal was to reproduce some experimental evidences reported by Grasa et al. (2008). These authors investigated the carbonation reaction rates in highly cycled sorbents, studying their reactivity under different conditions of partial pressure of $CO_2$, temperature, particle size, limestone type and number of cycles. The model used to interpret the obtained data is a homogeneous model. The first reaction stage is a fast and chemically controlled stage, and it is followed by a slower reaction stage controlled by diffusion in the $CaCO_3$ product layer. The transition between the fast and the slow regimes occurs suddenly once reached a given level of conversion. This value decreases with the increasing of the cycles, mainly because of the sintering of the sorbent.

Grasa et al. (2008) performed experiments in a TGA apparatus specially designed for long multi-cycle tests: the furnace can be moved up or down, so that the crucible alternates between calcination conditions (>850°C, for 15 min) and carbonation conditions (650°C for 20 min) during the same batch test. The sorbent performance was examined on quantity of 15 mg and the gas flow rate was set to the required value to eliminate external diffusion effects around the sample crucible ($4·10^{-6}$ m$^3$/s).

Similarly, we performed thermo-gravimetric experiments, however our tests were conducted only in carbonation conditions due to the different features of our TG instrumentation. Approximately the same amounts of CaO, obtained by a previous calcination (heating at 5°C/min and isotherm at 1000°C for 30 min) were heated up to 600°C and up to 650°C at a 10°C/min heating rate in a $N_2$ flux (100 mL/min); once the final temperature was reached, it

was kept constant, for a time varying from 20 min up to 40 min, at a $CO_2$ flux of 100 mL/min (approximately $1.67 \cdot 10^{-6}$ m$^3$/s). The sample weight changes recorded are shown in Figure 3.6.
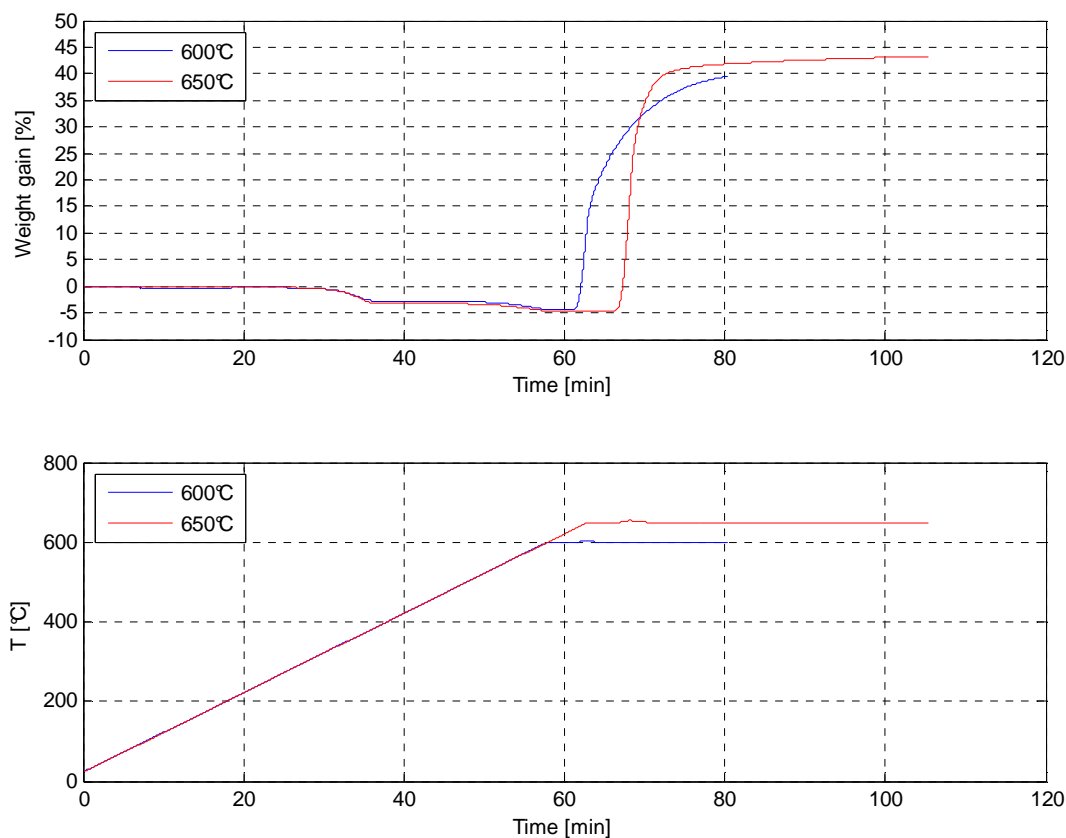


**Figure 3.6.** *TG analysis: weight gain vs. time of CaO carbonated in $CO_2$; heating up to carbonation temperature (10°C/min with $N_2$ flow rate of 100 mL/min) followed by a carbonation stage in $CO_2$ (100 mL/min). Sample size: ~15 mg, particle diameter: 10 μm*

It is noted that between the phase of heating (approximately 60-65 min) and the sorption stage (isotherm), there is a temperature stabilization phase of about 3 min after which the $N_2$ flux is switched in $CO_2$, indicating the real start of the absorption.

Analyzing Figure 3.6, it can be seen that during the heating ramp the CaO lost weight: we suppose that this phenomenon is caused by the release of the humidity that the oxide naturally and strongly absorbs from the atmosphere. For the 650°C test, the carbonation can be reasonably considered concluded after 40 min, while the test at lower *T* was stopped before the complete $CO_2$ absorption (carbonation stage of 20 min). The same conclusions can be more clearly drawn from the CaO conversion profiles shown in Figure 3.7, where the start time refers to the carbonation/absorption stage beginning.

The CaO conversion plot of Figure 3.7 (and 3.8) shows the transition between the fast (chemical-controlled) and the slow (diffusion-controlled) regimes during the $CO_2$ capture phase, in particular for the higher temperature.
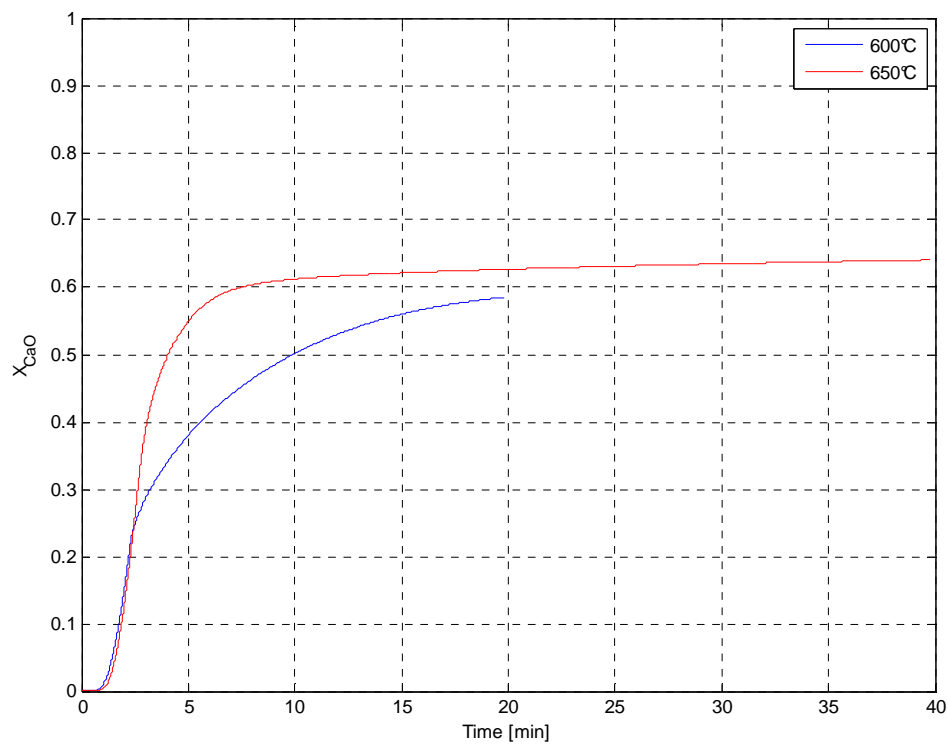
**Figure 3.7.** *CaO conversion vs. time during the carbonation stage conducted in the TG analyzer at a heating rate of 10°C/min with gas flow rate of 100 mL/min. Sample size: ~15 mg, particle diameter: 10 μm*
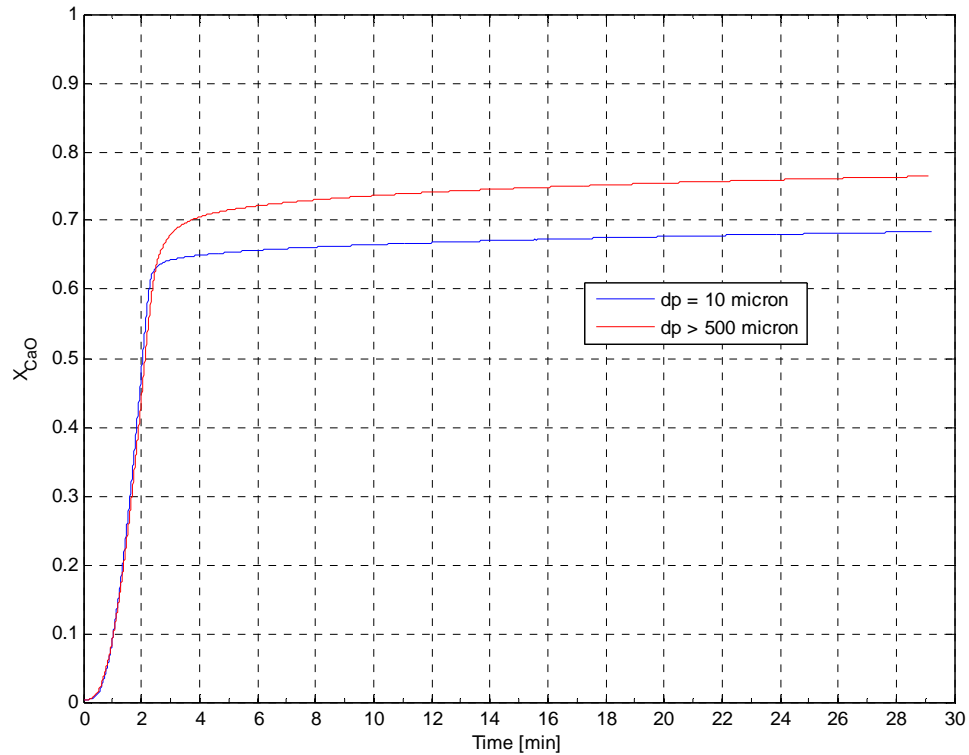


**Figure 3.8.** *CaO conversion vs. time during the carbonation reaction conducted in $CO_2$ atmospheric pressure at 650°C for 30 min; the tests were conducted on CaO particles of two different diameters (10 μm, blue line; 500 μm, red line) obtained by calcite calcination (15 min at 900°C)*

The results were compared to the measurements of Grasa et al. (2008), referring to one cycle of carbon dioxide absorption performed at $CO_2$ partial pressure of 1 atm. The comparison shows a similar CaO conversion in a comparable time scale of few minutes, even though there are some differences.

Grasa et al. (2008), who reach a conversion of approximately 60% in 1 min about, carried out experiments with sorbent samples with particle size ranging from 0.25 to 1 mm, bigger than those used in our tests (particle diameter of 0.01 mm). Although smaller particle size should ensure a higher conversion rate, we obtained the same conversion ($X_{CaO} \sim 0.60$) in a longer time than that reported by Grasa et al. (2008), namely 5-6 min, neglecting the first minute of stabilization in absence of $CO_2$ shown in Figure 3.7). Therefore, we can explain the discrepancy in the reaction rate observed considering the different chemical composition and/or physical structure of the CaO precursor, the calcination conditions at which the sorbent was obtained and, probably, the lower gas flow rate used during our carbonation stage. Concerning the effect of the calcination conditions, is should be recalled that thermal treatments at high temperatures promotes sintering, and that our severe calcination conditions could have caused changes in the CaO pores shape and a reduction in its reactive surface area with a penalization of the rate of the first chemically-controlled absorption stage.

Grasa et al. (2008) verified that the (initial) fast reaction regime is slightly affected by the particle size in the first calcinations/carbonation cycle; when the number of cycles is increased, the conversion curves of all the different particles are overlapped, indicating that the dependence on the size is no more significant. This is confirmed by our experiments (Fig. 3.8) also in the first cycle: the reaction rate is the same for the 10 µm and the 500 µm sized particles.

## 3.4 Critical aspects in thermo-gravimetric analyses

As already mentioned, thermal analysis techniques (TGA, DTA) are commonly utilized to study the thermal decomposition reactions where, in addition to solid reagents, gaseous reactants or products are involved. However, these techniques are plagued with problems of mass and energy transport which are usually unavoidable. Satterfield and Feakes (1959) explain in fact that among the potential rate-limiting processes in the thermal decomposition of carbonates, the following transport phenomena must be considered: the heat transfer to the particle surface and through the oxide product layer to the reaction interface; the mass transfer of $CO_2$ released at the reaction zone away from the interface.

The calcination is in fact strongly influenced by the partial pressure of carbon dioxide that is developed in the decomposition.

It is quite simple to understand how an increase of the partial pressure of $CO_2$ (at fixed temperature) enhances the effects of the reverse reaction, limiting the decomposition step.

The effects of sample mass and $CO_2$ partial pressure on the thermal decomposition are linked and significant. Wilburn et al. (1991), investigating the effect of several operative variables on the calcium carbonate decomposition in TGA-DTG, explain their results in terms of bed-depth effect: during the reaction, carbon dioxide evolves at a rate faster than it can escape from the reaction zone through the sample mass, causing a local increase of the partial pressure of $CO_2$ within the powder bed. The deeper the sample bed (namely the greater the mass of carbonate sample in a given volume/crucible), the greater the build-up of carbon dioxide partial pressure, at the same experimental conditions.

Another important aspect pertains to the temperature at which the thermal decomposition is carried out. At fixed heating rate, the decomposition starts when the calcination temperature within the particles is reached. As observed by Satterfield and Feakes (1959), the reaction temperature is determined by a balance between two rate processes, namely the rate of heat transfer towards the reaction zones and the rate of the heat consumption by the endothermic reaction. Heat must first be transferred at the surface of the particles, through the sample mass, and then through the product layers which are formed as the reaction proceeds. The heat transfer depends on the thermal conductivity of the gaseous environment and on the heat conduction mechanism through the particle. Gallagher and Johnson (1976) and Borgwardt (1985) argue that the thermal transport rather than $CO_2$ diffusion/mass transport is the rate determining factor which controls the carbonate decomposition rate. Under conditions of constant partial pressure of $CO_2$, the reaction is controlled by the ability to supply heat to the reaction interface, and this aspect is closely related to several factors (in particular, referring to TG experiments, sample packing and particle size, holder and geometry, the thermal conductivity of the atmosphere, the properties of the products layers etc.).

It was noted (Gallagher and Johnson, 1976; Borgwardt, 1985) that facilitating either the thermal transport or the mass transport has the same effect of decreasing the measured temperature at which the decomposition occurs but separating the effects of thermal and mass transport is difficult. Performing thermal decomposition tests with 10 µm particles using an entrained flow reactor, Borgwardt (1985) was able to measure $CaCO_3$ conversions of approximately 80% in a time scale (few seconds) lower than those observed by other authors carrying out TGA experiments (typically several minutes). In TGA the decomposition rate is influenced by mass and heat transfer resistances that are present in the sample, instead in the entrained flow reactor the particles are isolated from the each other with reduced heat/mass transfer resistances.

However, these aspects should be investigated more in detail in order to underline information on chemical or bond-breaking rate-limiting processes (Gallagher and Johnson, 1976) or/and, minimizing the effects of thermal and mass transport, to obtain real/pure kinetics information on the calcite/dolomite thermal decomposition.

# Chapter 4

# Utilization of $CO_2$ solid sorbents in gasification/combustion processes

## 4.1 Introduction

The goal of the work presented in this chapter is to investigate the feasibility of utilizing calcium/magnesium/dolomite based sorbents to capture the carbon dioxide in coal gasification or fossil fuel combustion processes.

Application of calcium based sorbents were recently reviewed by Dean et al. (2011) and include two kind of possible configurations for CCS: post- or pre-combustion $CO_2$ capture. The Ca-looping cycle is expected to have a widespread usage in the future because of the low overall cost of gas capture, namely ~19 USD/ton$CO_2$ avoided in case of post-combustion configuration; it results competitive with ammine-based scrubbing, for which this cost is 32.5-80 USD/ton$CO_2$ avoided. The avoided emissions result comparing the $CO_2$ emissions per kWh of the plant with capture to that of a reference plant without capture (Metz et al., 2005). The overall cost of gas capture is low mainly because of the cheapness of the used raw materials and the low energy penalty (~5%, including compression) compared to a plant without capture. In the world there are several pilot plant trials with post-combustion carbon dioxide capture and each of them reaches high levels of gas capture: CANMET Energy and Technology Center (Ottawa), INCAR-CSIC (Oviedo), University of Stuttgart (Stuttgart) and Ohio State University (Columbus) have different kWth facilities but all of them achieves at least 90% of $CO_2$ capture efficiency (increasing the number of regeneration cycles it usually decreases to 70-80%). Dean et al. (2011) describe also some configurations that are applied to plants for the production of hydrogen and/or electricity: coupling the carbonation reaction with the water-gas reaction, sorption enhanced reforming (reforming of hydrocarbons combined with the carbonation and the water-gas shift reactions), in situ $CO_2$ capture for solid fuels (coal and biomass) gasification, the zero emission coal (ZEC) process, the ENDEX configuration.

Magnesium based sorbents were developed by Hassanzadeh and Abbasian (2010), in the perspective of capturing the $CO_2$ from the syngas in an IGCC (integrated gasification combined cycle) plant adopting a pre-combustion configuration. Carbon capture is carried out by half calcined dolomite on syngas already desulfurized.

In this chapter, the focus is on two processes: IGCC (§4.2) and fossil fuel combustion (§4.3).

For each of these processes, a base case design of the absorber (the reactor where the $CO_2$ is captured) is proposed, assuming that it is a circulating fluidized bed; CFBs are a mature technology that allows to operate continuously high throughput of reactants. To capture the carbon dioxide, solid sorbents can be utilized because of their high mechanical strength (they are not significantly affected by attrition). Additionally they can be used also at high temperature, allowing to preserve a high thermal efficiency of the process: this is particularly advantageous in pre-combustion plant because the absorber can be operated at a temperature similar to the combustion temperature.

The gaseous stream is blown upward in co-current with the solid sorbent in the vertical absorber in conditions of fast fluidization or core annular regime to ensure fluid-dynamic stability (Fig. 4.1). The pneumatic conveying is typically avoided because the solid phase is too much diluted and it implies low conversion of the sorbent.
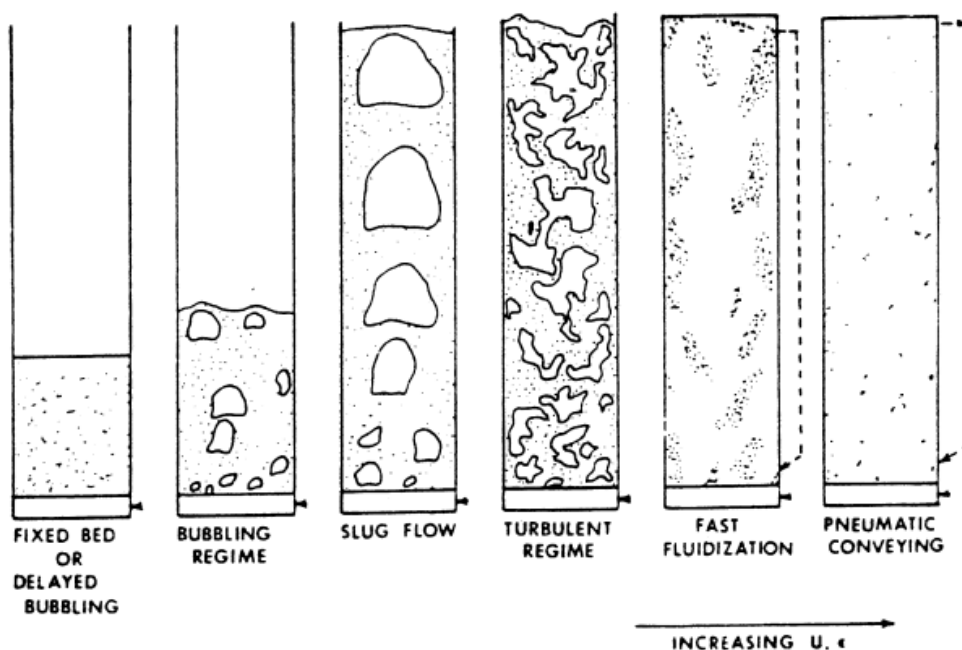


**Figure 4.1.** *Main flow regimes for up-ward flow of gas through solid particulate materials (Grace, 1986)*

The sorbent can be regenerated by decreasing the pressure or increasing the temperature, thus producing a concentrated carbon dioxide stream which can be utilized in industrial applications or stored.

In the following sections, it is verified that the absorber operates in the fast fluidization regime and that satisfies an adequate $CO_2$ capture with the considered process. Finally, energy and mass balances are discussed.

## 4.2 CO$_2$ capture in an IGCC process

### 4.2.1 Process description

In a coal IGCC (integrated gasification combined cycle) power plant the adopted configuration for carbon dioxide capture is the pre-combustion technology. In such kind of process the fuel is fed to a (heated and pressurized) gasifier and the produced syngas, a mixture of $H_2$, CO, $CH_4$, $CO_2$, $H_2O$ and other diluents, flows through a water gas shift reactor where the CO is converted to $CO_2$ producing additional $H_2$. Then the gas stream is sent to the $CO_2$ separation unit: carbon dioxide is removed and hydrogen rich syngas is used in a combustion turbine to generate electricity (US DOE, 2010). Solid sorbents are utilized in order to conduct the reaction at high temperature thus preserving a high thermal efficiency of the process. But, as pointed out by Hassanzadeh and Abbasian (2010), the sulfur present in the gas stream must be removed before the $CO_2$, otherwise it reacts with the sorbent leading to its deactivation. The hot gas desulfurization is expected to be carried out at 350-550°C then the ideal temperature for $CO_2$ removal is 300-500°C, which makes magnesium based sorbent ideal for such operation.
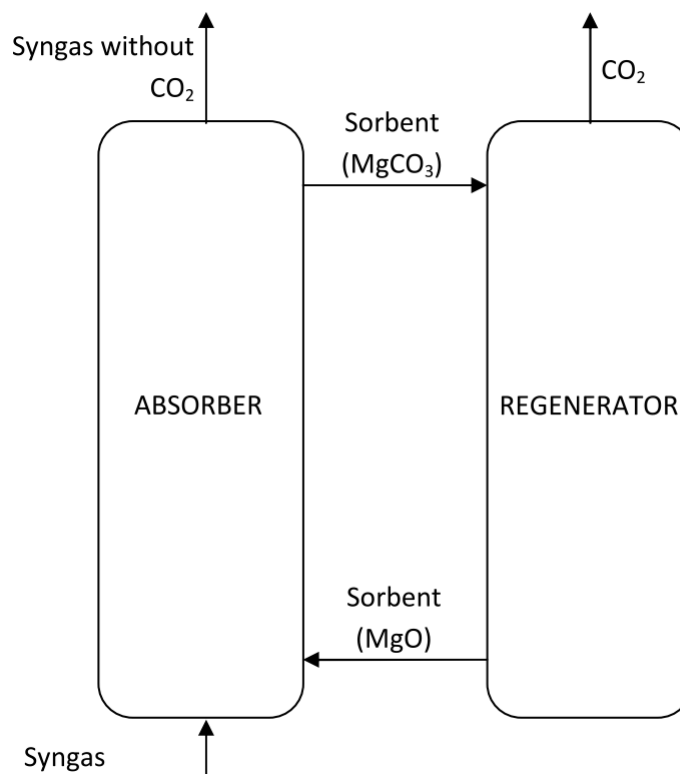


**Figure 4.2.** *Schematic of the CO$_2$ capture in a pre-combustion process utilizing magnesium based sorbents*

In the simulated process the used sorbent is the half decomposed dolomite externally covered by a potassium layer because of its low cost, high mechanical strength and high reactivity towards carbon dioxide (Hassanzadeh and Abbasian, 2010). The dolomite half decomposition is supposed to be complete, that is the sorbent is composed of MgO and $CaCO_3$. The carbon dioxide can react following two different paths:

$$CaCO_3 + MgO + CO_2 \leftrightarrow CaMg(CO_3)_2 \tag{4.1}$$

$$MgO + CO_2 \leftrightarrow MgCO_3. \tag{4.2}$$
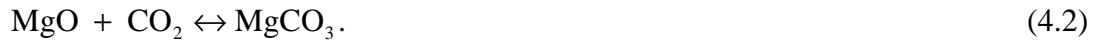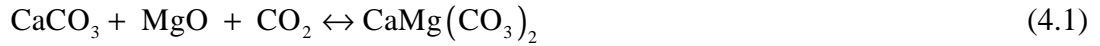
According to thermodynamic considerations the reaction that should take place is the first one (eq. (4.1)): the standard Gibbs free energy change of reaction is more negative for this reaction than for the other one.

The regeneration is carried out lowering the pressure and maintaining the temperature constant in the two reactors.

The process diagram is reported in Figure 4.2.

## 4.2.2 Operative conditions, kinetic data and $CO_2$ conversion

A typical syngas is composed by $H_2$ (25-30 vol%), CO (30-60 vol%), $CO_2$ (5-15 vol%), $H_2O$ (2-30 vol%), $CH_4$ (0-5 vol%) and other minor compounds (NETL website). For simplicity, in the absorber design the syngas is assumed to be constituted only by hydrogen and carbon dioxide, respectively 55.985 mol% and 44.015 mol% (Tab. 4.1).

The operating conditions are assumed to be 426°C and 20 bar in order to use the same kinetic data of Hassanzadeh and Abbasian (2010).

The syngas flowrate is derived from the conversion of 540 ton of coal per day, which roughly corresponds to a 70 MW power plant. It is assumed that all the carbon fed to the gasifier is converted to carbon dioxide after the water-gas shift unit. The gas volumetric flowrate $Q_v$, equal to 12439 $m^3$/h, is computed from the massive flowrate of coal feed $Q_p$:

$$Q_v = \frac{Q_p}{y_{CO_2} PM_C} \frac{RT}{P}. \tag{4.3}$$

$y_{CO_2}$ is the carbon dioxide molar fraction, $PM_C$ the molecular weight of carbon, $R$ the universal gas constant, $T$ the operating temperature, $P$ the operating pressure.

The reactor diameter and height are assumed to be 1.3 m and 30 m respectively. Such figures will be checked afterwards, namely it will be verified that the reactor can be operated in the

fast fluidization regime and that a high $CO_2$ capture efficiency can be obtained. Additionally, the solid flux $G_s$ is assumed to be equal to 483 kg/m²s.

Operative conditions, reactor size, solid and gas phase properties are summarized in Table 4.1.

**Table 4.1.** *Operating conditions and reactor size*

| Variable | Value |
|---|---|
| Temperature $T$ [K] | 703 |
| Pressure $P$ [bar] | 20 |
| Syngas composition [mol%] | $H_2 = 55.99$ $CO_2 = 44.01$ |
| Syngas flowrate $Q_v$ [m³/h] | 12439 |
| Absorber diameter $D$ [m] | 1.3 |
| Absorber height $H$ [m] | 30 |
| Solid flux $G_s$ [kg/m²s] | 483 |

Starting from the solid flux and the absorber height $H$, the average residence time of a solid particle $\tau_{solid}$ can be estimated as:

$$\tau_{solid} = \frac{H}{v_{solid}} \tag{4.4}$$

and it results to be equal to 10.8 s.

The solid velocity $v_{solid}$ is calculated as the difference of the gas velocity $v_{gas}$ and the terminal velocity $v_t$ (eq. (4.5)); this is an approximation because it should be computed as the difference between $v_{gas}$ and the slip velocity $v_{slip}$, which is defined as the velocity difference of the two phases. The slip velocity coincides with the terminal velocity only when the system is diluted, that is when the particles do not interact whit each other. Therefore, the simulated $v_{solid}$ results to be bigger than the real one and the $CO_2$ capture efficiency is underestimated. The solid and gas velocities, the solid volumetric fraction and the terminal velocities are computed as:

$$v_{solid} = v_{gas} - v_t \tag{4.5}$$

$$v_{gas} = \frac{4Q_v}{\pi D^2} \frac{1}{1 - \varepsilon_{solid}} \tag{4.6}$$

$$\varepsilon_{solid} = \frac{G_s}{\rho_{solid} v_{solid}} \tag{4.7}$$

$$v_t = \sqrt{\frac{4}{3}\frac{d_p}{f}\frac{\rho_{solid}-\rho_{gas}}{\rho_{gas}}g} = \sqrt{\frac{4}{55.5}d_p^{0.4}\frac{(\rho_{solid}-\rho_{gas})}{\rho_{gas}^{1.6}}\frac{\mu_{gas}^{0.6}g}{v_{gas}^{0.6}}} .$$ (4.8)

In eq. (4.6), $\varepsilon_{solid}$ is the solid volume fraction in the reactor, assumed to be constant; in eq. (4.8), $\rho$ is the solid or gas density, $g$ is the gravity acceleration (9.81 m/s$^2$), $\mu_{gas}$ is the gas viscosity. Eq. (4.6) and eq. (4.8) are the formulae for the gas velocity $v_{gas}$ and the solid terminal velocity $v_t$. The last one is determined through a force balance on a single particle suspended in the fluid: buoyancy force, friction force and gravity force. The friction factor $f$ is defined as a function of the Reynolds particle number $Re_p$:

$$\text{Re}_p = \frac{\rho_{gas}v_{gas}d_p}{\mu_{gas}} .$$ (4.9)

In the considered case $Re_p$ is 52.86 then the particle motion is in the transitional flow (characterized by the condition $0.2 < Re_p < 1000$) and $f = 18.5/Re_p^{3/5}$. The particle diameter $d_p$ is set equal to 70 µm, as discussed further.

The gas density $\rho_{gas}$ is computed (Tab. 4.3) assuming that the syngas is equal to a pseudo binary mixture composed of hydrogen and carbon dioxide:

$$\rho_{gas} = \frac{\left(PM_{H_2}y_{H_2} + y_{CO_2}PM_{CO_2}\right)P}{RT} .$$ (4.10)

The gas viscosity $\mu_{gas}$ is roughly around $260*10^{-6}$ g/(cm·s) (Tab. 4.3) and is evaluated from the critical properties (Tab. 4.2) of the pseudo binary mixture using Figure 4.3 which plots the reduced viscosity $\mu_r = \mu/\mu_c$ as function of reduced temperature $T_r = T/T_c$ and pressure $P_r = P/P_c$ (Bird et al., 2002):

$$P_c^{mix} = \sum_{i=1}^{nc} y_i P_{c,i}$$ (4.11)

$$T_c^{mix} = \sum_{i=1}^{nc} y_i T_{c,i}$$ (4.12)

$$\mu_c^{mix} = \sum_{i=1}^{nc} y_i \mu_{c,i} .$$ (4.13)
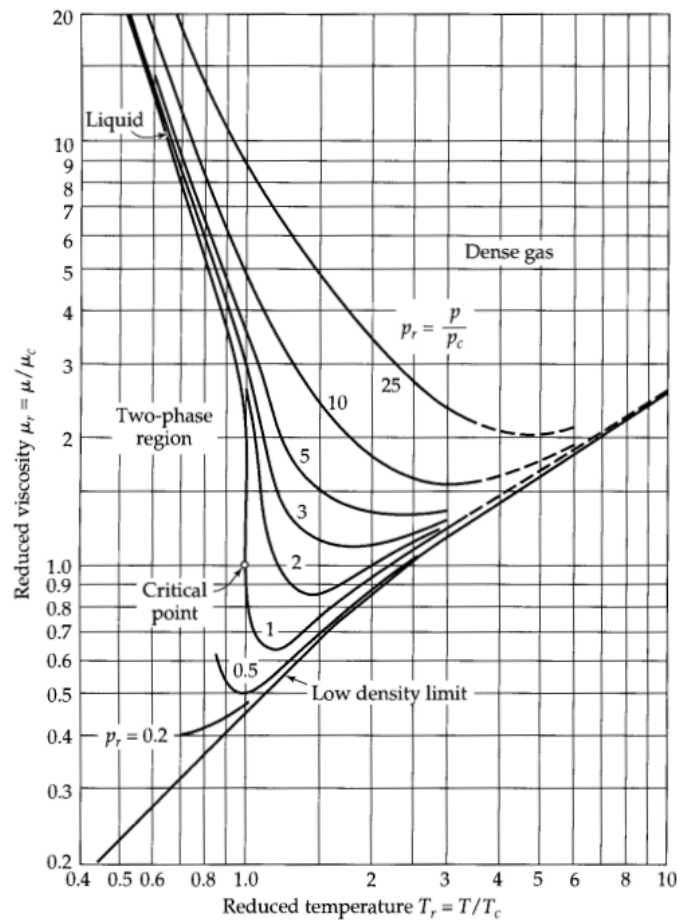
**Figure 4.3.** *Reduced viscosity as function of reduced temperature for several values of reduced pressure (Bird et al., 2002)*

**Table 4.2.** *Critical properties of gases*

|  | $T_c$ [K] | $P_c$ [atm] | $\mu_c$ [g/cm s] |
|---|---|---|---|
| $CO_2$ | 304.2 | 72.8 | $343 \cdot 10^{-6}$ |
| $H_2$ | 33.3 | 12.8 | $34.7 \cdot 10^{-6}$ |
| Simulated syngas | 152.5 | 39.2 | $170.4 \cdot 10^{-6}$ |

**Table 4.3.** *Gas and solid properties*

| Property | Value |
|---|---|
| Solid density $\rho_{solid}$ [kg/m³] | 2500 |
| Gas density $\rho_{gas}$ [kg/m³] | 7.0143 |
| Gas viscosity $\mu_{gas}$ [poise] | $260 \cdot 10^{-6}$ |

Hassanzadeh and Abbasian (2010) used magnesium based solid sorbent derived from dolomite and impregnated by potassium which increase the solid reactivity towards the

carbon dioxide. Their particle diameter $d_p^{HA}$ is 510 µm but their conversion is low if the residence time is roughly equal to 10.8s (value computed in our simulations through eq.(4.4)). Thus, to improve the sorbent exploitation the simulated particle diameter $d_p$ is 70 µm.

Adopting such small size could be a problem in case of fluidized bed reactors because small particles can be cohesive: to understand if this occurs we can use the Geldart diagram (Fig. 4.4) which allows to classify the particle cohesiveness as function of particle size and of gas and particle density difference.
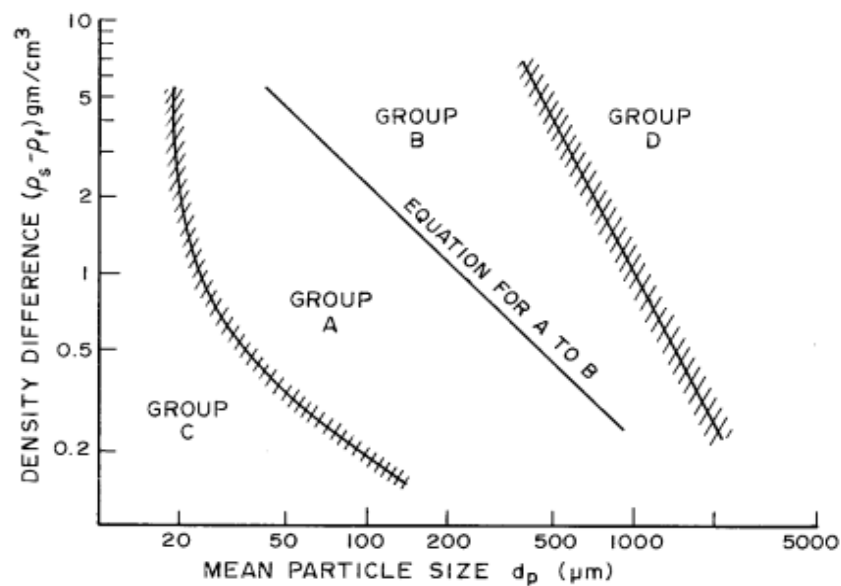


**Figure 4.4.** *Geldart classification of fluidized particles (Gidaspow, 1994)*

Using the data of Table 4.3 the sorbent is fluidizable and it belongs to group A, that is aerated particles, of small mean size and low density. Also group B (bubbling) is constituted of fluidizable particles but their size and density are larger than the group A particles.

In order to estimate the $CO_2$ capture efficiency, the sorbent conversion must be evaluated. Hassanzadeh (2007) calculated the MgO conversion, defined as the reacted MgO moles per the initial MgO moles, as a function of time (Fig. 4.5). To use the same kinetic data, some assumptions must be made. The curves are parametric on the absorber temperature and are referred to 20 atm pressure in a $CO_2/N_2 = 50/50$ atmosphere. In the simulated case the pressure is 20 bar but the gas composition is the syngas one: conditions are then different but the assumption is that hydrogen and nitrogen have similar behavior towards the sorbent, namely they do not affect the $CO_2$ capture. As far as the difference in sorbent size, the thickness of the particle reacted layer is supposed to be constant for the two particles despite the difference in their size. This assumption can be done because, the simulation residence time being 10.8 s, such layer $l_r$ is small (2.33 µm) if compared with the solid diameter in the both cases: the 510 and the 70 µm.
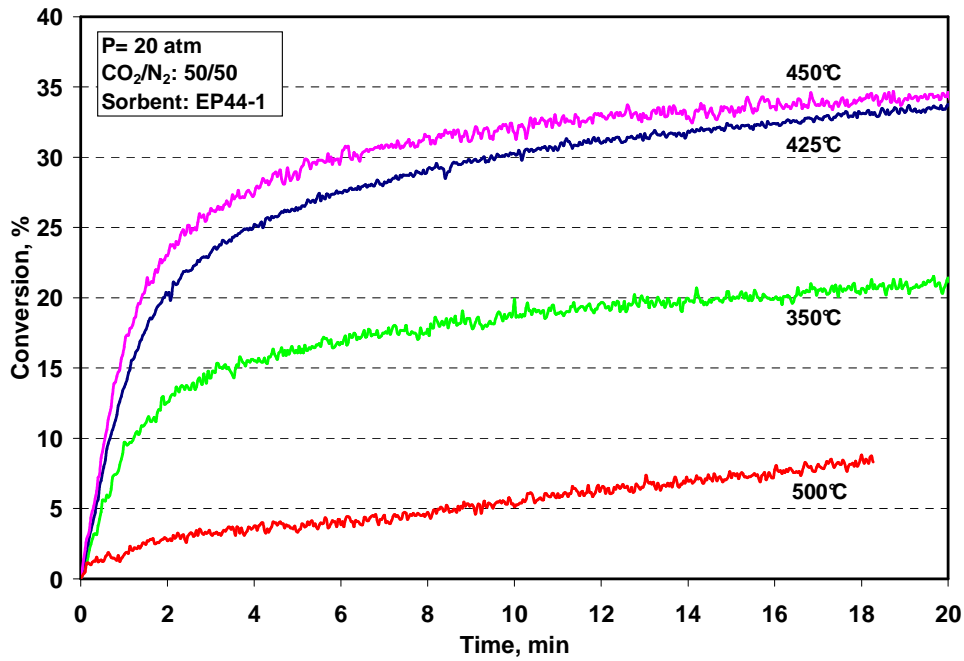
**Figure 4.5.** *Sorbent performance versus time (Hassanzadeh, 2007)*

In Hassanzadeh's experiments (Hassanzadeh, 2007), MgO based sorbents with particle diameter $d_p^{HA}$ react in given conditions of temperature, pressure and composition (Fig. 4.5). For a reaction time equal to $\tau_{solid}$, the MgO conversion ($X_{MgO}^{HA}$) is derived from the Hassanzadeh's plot (Fig. 4.5) (Hassanzadeh, 2007). From this data, the reactive layer $l_r$ is computed:

$$X_{MgO}^{HA} = \frac{n_{converted}}{n_{initial}} = 1 - \left(\frac{d_p^{HA} - 2l_r}{d_p^{HA}}\right)^3 \tag{4.14}$$

$$l_r = 255 * 10^{-6} * (1 - (1 - X_{MgO}^{HA})^{1/3}) \tag{4.15}$$

$l_r$ is then used to evaluate the particle conversion of the simulated case $X_{MgO}$ with particle size $d_p$ at the same conditions of $T$, $P$ composition and reaction time:

$$X_{MgO} = 1 - \left[\left(\frac{d_p}{2} - l_r\right)\bigg/\frac{d_p}{2}\right]^3 . \tag{4.16}$$

For small reaction times ($\tau \rightarrow 0$), Hassanzadeh's kinetic data can be expressed as first order reaction (Hassanzadeh, 2007) :

$$\left.\frac{dX_{MgO}^{HA}}{dt}\right|_{t\to 0} = k_{int}\exp\left(\frac{-E_a}{RT}\right)(c_{CO_2} - c_{CO_2}^{eq}).\tag{4.17}$$

In eq. (4.17), $k_{int}$ is a second order function that interpolates Hassanzadeh's experimental data (at $T = 703$ K, $k_{int} = 2.0081$ m$^3$/(mol·min)), $E_a$ is the reaction activation energy (44.10 kJ/mol), $c_{CO2}$ is the CO$_2$ concentration, $c_{CO_2}^{eq}$ is the equilibrium concentration. The MgO conversion for the simulated case is obtained from the formulation of Hassanzadeh (eq. (4.17)) scaled by a geometrical factor that accounts for the particle size difference: $X_{MgO}/X_{MgO}^{HA}$. The assumption of small reaction time is here justified because $\tau_{solid}$ is equal to 10.8 s in the simulated case.

The carbon dioxide conversion is evaluated assuming the absorber as an isothermal plug flow reactor, then the mass balance on an element of infinitesimal volume $dV$ is:

$$\dot{n}_{CO_2}^{in\ dV} - \dot{n}_{CO_2}^{out\ dV} + r_{CO_2}dV = 0\tag{4.18}$$

$$\dot{n}_{CO_2}^{in\ dV}dX_{CO_2} + r_{CO_2}dV = 0\tag{4.19}$$

$\dot{n}_{CO2}^{in\ dV}$ and $\dot{n}_{CO2}^{out\ dV}$ are the CO$_2$ molar flowrate that enters and exits in the infinitesimal volume $dV$ respectively; $r_{CO2}$ is the carbon dioxide reaction rate and is defined as the consumed moles of CO$_2$ per unit of volume and time.

To use Hassanzadeh (2007) kinetic data, the reaction rate $r_{CO2}$ must be expressed in terms of MgO moles:

$$\begin{aligned}\dot{n}_{CO_2}^{in}dX_{CO_2} &= \frac{w_{MgO}\rho_{solid}\varepsilon_{solid}}{PM_{MgO}}\frac{dX_{MgO}}{dt}dV\\[2mm]&= \frac{w_{MgO}\rho_{solid}\varepsilon_{solid}}{PM_{MgO}}\frac{dX_{MgO}^{HA}}{dt}\frac{X_{MgO}}{X_{MgO}^{HA}}Adh\end{aligned}\tag{4.20}$$

$$w_{MgO} = \frac{PM_{MgO}}{PM_{MgO} + PM_{CaCO_3}}.\tag{4.21}$$

$w_{MgO}$ is the solid mass fraction of magnesium oxide in the half decomposed dolomite before been used in CO$_2$ capture (0.287 w/w); assuming that the half decomposition goes to completion, the sorbent is composed of MgO, $w_{MgO}$, and CaCO$_3$, $1$-$w_{MgO}$.

Integrating from the inlet of the reactor, where the $X_{CO2}$ is 0, to the reactor exit $H$, the CO$_2$ conversion $X_{CO2}$ results:

$$X_{CO2} = -\frac{(c_{CO_2}^{in} - c_{CO_2}^{eq})}{c_{CO_2}^{in}} \left\{ \exp\left[ \frac{-c_{CO_2}^{in} k_{fit} \exp(-E_a / RT) w_{MgO} \varepsilon_{solid} \rho_{solid} AH}{PM_{MgO} \dot{n}_{CO_2}^{in}} \frac{X_{MgO}}{X_{MgO}^{HA}} \right] - 1 \right\} .(4.22)$$

Since the carbon dioxide reacts with the solid species and it is absorbed, the gas and the solid streams change their values and velocities but they are assumed to be constant.

**Table 4.4.** *Computed results*

| Resulting quantity | Value |
|---|---|
| Solid fraction $\varepsilon_{solid}$ [-] | 0.07 |
| CO₂ conversion $X_{CO2}$ (%) | 67.70 |
| Gas velocity $v_{gas}$ (m/s) | 2.799 |
| Solid velocity $v_{solid}$ (m/s) | 2.759 |

The assumed solid flux is 483 kg/m²s that corresponds to a solid fraction of 0.07 in the absorber. The carbon dioxide converted moles are 0.352 kmol/s, which correspond to a conversion of the inlet moles of 67.70% and to a particle conversion $X_{MgO}$ of 18.69%, one order of magnitude higher than the 510 μm sized particles ( $X_{CO2}^{HA}$ = 2.72%).

## 4.2.3 Fluidization analysis

As already discussed, the reactor is a circulating fluidized bed and in must be verified that the reactor is operated in the fast fluidization regime. In this kind of reactor the gas velocity must be between type A choking velocity $V_{CA}$ and type C choking velocity $V_{CC}$ values. The type A choking velocity is defined (Bi and Grace, 1995) as the point where the uniform suspension collapses and particles accumulate at the bottom reducing the gas velocity, so it corresponds to the minimum transport velocity. The type C choking velocity is identified (Bi and Grace, 1995) by the onset of a severe slugging when gas velocity is decreased until it is no more sufficient to the transport, supposing to provide sufficient blower pressure and solid feeding (if they are insufficient the generated chocking is the type B one and it is a system related problem). These velocities are calculated using the following expressions (Bi and Grace, 1995):

$$V_{CA} = \left( \frac{21.6 Ar^{0.105} G_s^{0.542} g^{0.5} d_p^{0.5}}{\rho_{gas}^{0.542}} \right)^{1/1.542} \tag{4.23}$$

$$V_{CC} = \left( \frac{32 \, Re_t^{-0.06} G_s^{0.28} g^{0.5} d_p^{0.5}}{\rho_{gas}^{0.28}} \right)^{1/1.28} . \tag{4.24}$$

In eq.s (4.23) and (4.24) $G_s$ is the solid flux, $g$ the gravity acceleration, $d_p$ the particle diameter, $\rho_{gas}$ the gas density, $Ar$ the Archimedes number and $Re_t$ the Reynolds number based on the terminal velocity. The two dimensionless numbers are defined by:

$$Ar = \frac{\rho_{gas}(\rho_{solid} - \rho_{gas})gd_p^{\ 3}}{\mu_{gas}^{\ 2}} \tag{4.25}$$

$$Re_t = \frac{\rho_{gas}v_t d_p}{\mu_{gas}}. \tag{4.26}$$

With the simulated case data, the type C choking velocity $V_{CC}$ is 2.228 m/s and type A choking velocity $V_{CA}$ is 4.147 m/s. The gas velocity $v_{gas}$ (= 2.799 m/s) is included in this two values then the absorber is in the fast fluidization regime as desired.

The flow pattern for gas-solid upward transport is mapped by Bi and Grace (1995). Figure 4.6 refers to a specific case, different than the case simulated in the present work, but it shows the gas velocity dependence on the solid flowrate and focus on the reason why the circulating bed must be exercised between the two cited choking velocities. If the gas velocity is lower than type C choking the upward transport of the solid is nearly impossible; if it is higher than type A choking the phase flow is diluted (and the sorbent conversion drops).
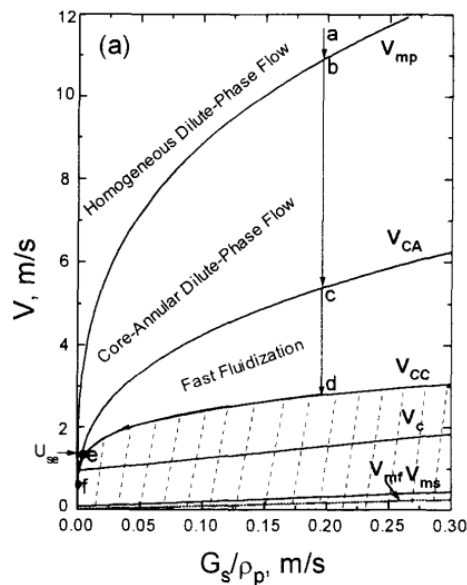


**Figure 4.6.** *Example of flow regime map for gas-solid upward transport for group A particles; the shaded regions indicate zones when practical operation is very difficult if not impossible (Bi and Grace, 1995)*
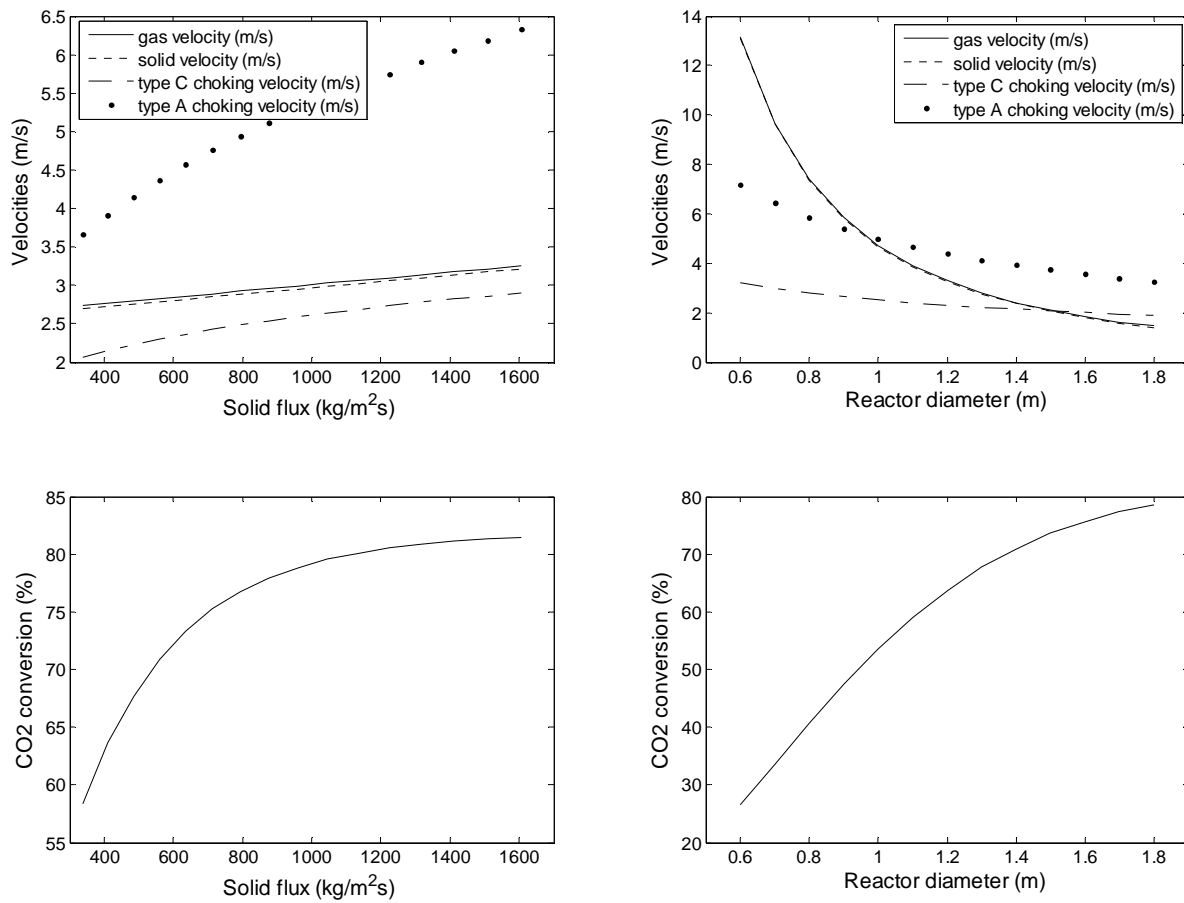
**Figure 4.7.** *Parametric studies: the figures represent the dependence of $v_{gas}$, $v_{solid}$, $V_{CC}$ and $V_{CA}$ (top) and CO$_2$ conversion (bottom) on the solid flux $G_s$ (left) and on reactor diameter D (right); gas and solid velocities are overlapped*

Increasing the solid flowrate the removal efficiency increases and also the choking velocities (Fig. 4.7, left). However, $G_s$ cannot be increased indefinitely, because a solid flux increase results in an increase of the solid volumetric fraction as well. When $\varepsilon_{solid}$ reaches the value of 0.2, the absorber does not work anymore in the fast fluidization regime. To ensure the correct operating conditions for fast fluidization circulating beds the solid flux can be varied until the condition $\varepsilon_{solid} = 0.05\text{-}0.20$ is satisfied, according to Bi and Grace (1995).

Increasing the reactor diameter (Fig. 4.7, right), the gas velocity decreases and its decrease rate is faster than the rate at which the choking velocities drop. In the simulated case the limits to work in the fast fluidization regime are 0.95-1.55 m.

## 4.2.4 Material and energy balances

As previously discussed (§4.2.1), the reaction that takes place in the absorber is assumed to be:

$$CaCO_3 + MgO + CO_2 \leftrightarrow CaMg(CO_3)_2 . \tag{4.1}$$

The absorber operates in stationary state, then the accumulation term of the balances is set equal to 0 and the resulting general formula for the material balance is

$$0 = Inlet - Outlet + Production - Consumption \,. \tag{4.27}$$

The material balances are evaluated for each compound and relate each over by the reaction stoichiometry:

$$0 = \dot{n}_{CO_2}^{in} - \dot{n}_{CO_2}^{out} - \dot{n}_{CO_2}^{cons} \tag{4.28}$$

$$0 = \dot{n}_{H_2}^{in} - \dot{n}_{H_2}^{out} \tag{4.29}$$

$$0 = \dot{n}_{MgO}^{in} - \dot{n}_{MgO}^{out} - \dot{n}_{MgO}^{cons} \tag{4.30}$$

$$0 = \dot{n}_{CaCO_3}^{in} - \dot{n}_{CaCO_3}^{out} - \dot{n}_{CaCO_3}^{cons} \tag{4.31}$$

$$0 = \dot{n}_{dolomite}^{in} - \dot{n}_{dolomite}^{out} + \dot{n}_{dolomite}^{prod} \tag{4.32}$$

$$\dot{n}_{CO_2}^{cons} = \dot{n}_{MgO}^{cons} = \dot{n}_{CaCO_3}^{cons} = \dot{n}_{dolomite}^{prod} \,. \tag{4.33}$$

The molar flowrates of hydrogen and carbon dioxide are computed from the coal feed to the gasificator $Q_p$, assuming that all the carbon is converted to $CO_2$, from the syngas composition ($y_{CO2}$) and from the previously calculated $CO_2$ conversion $X_{CO2}$:

$$\dot{n}_{CO_2}^{in} = \frac{Q_p}{PM_C} \tag{4.34}$$

$$\dot{n}_{CO_2}^{out} = \dot{n}_{CO_2}^{in}(1 - X_{CO_2}) \tag{4.35}$$

$$\dot{n}_{H_2}^{in} = \dot{n}_{syngas}^{in} - \dot{n}_{CO_2}^{in} = \frac{\dot{n}_{CO_2}^{in}}{y_{CO_2}} - \dot{n}_{CO_2}^{in} \tag{4.36}$$

$$\dot{n}_{H_2}^{out} = \dot{n}_{H_2}^{in} \,. \tag{4.37}$$

The inlet molar flowrate of the solid species are evaluated from the solid flux $G_s$ and the mass fraction composition of the half decomposed dolomite ($w_{MgO}$ and $1$-$w_{MgO}$):

$$\dot{n}_{MgO}^{in} = \frac{G_s A w_{MgO}}{PM_{MgO}} \tag{4.38}$$

$$\dot{n}^{in}_{CaCO_3} = \frac{G_s A(1-w_{MgO})}{PM_{CaCO_3}}$$ (4.39)

$$\dot{n}^{in}_{dolomite} = 0.$$ (4.40)

The outlet flowrate are obtained subtracting the consumed (or adding the produced) moles from the inlet ones, knowing that one mole of CO$_2$ reacts with one mole of MgO and one mole of CaCO$_3$ to give one mole of CaMg(CO$_3$)$_2$:

$$\dot{n}^{out}_{MgO} = \dot{n}^{in}_{MgO} - \dot{n}^{cons}_{MgO} = \dot{n}^{in}_{MgO} - \dot{n}^{cons}_{CO_2}$$ (4.41)

$$\dot{n}^{out}_{CaCO_3} = \dot{n}^{in}_{CaCO_3} - \dot{n}^{cons}_{CaCO_3} = \dot{n}^{in}_{CaCO_3} - \dot{n}^{cons}_{CO_2}$$ (4.42)

$$\dot{n}^{out}_{dolomite} = \dot{n}^{in}_{dolomite} + \dot{n}^{prod}_{dolomite} = \dot{n}^{cons}_{CO_2}.$$ (4.43)

The molar flowrate obtained with the previously reported data for each species are reported in Table 4.5. The amount of converted moles in the absorber is 0.3523 kmol/s for each species.

**Table 4.5.** *Molar flowrates at the absorber inlet and outlet*

|  | Inlet moles [kmol/s] | Oulet moles [kmol/s] |
|---|---|---|
| Carbon dioxide CO$_2$ | 0.5204 | 0.1681 |
| Hydrogen H$_2$ | 0.6619 | 0.6619 |
| Magnesium oxide MgO | 4.5640 | 4.2117 |
| Calcium carbonate CaCO$_3$ | 4.5640 | 4. 2117 |
| Dolomite CaMg(CO$_3$)$_2$ | 0 | 0. 3523 |

The macroscopic energy balance in stationary state is expressed as follows:

$$\dot{Q} - \dot{W}_s - \Delta\left[\dot{n}\left(h + e_{kin} + e_{pot}\right)\right] = 0.$$ (4.44)

$\dot{Q}$ is the heat released (negative) or absorbed (positive) by the absorber per unit of time, $\dot{W}_s$ is the power (shaft work) exchanged with the surroundings, $\dot{n}$ is the molar flowrate that enters and exits through the system boundaries, $h$ the specific molar enthalpy, $e_{kin}$ the specific molar kinetic energy and $e_{pot}$ the specific molar potential energy of the flowrate. The $\Delta$ symbol indicate the variation of the in brackets quantities between the outlet and the inlet of the system boundaries. The absorber does not exchange work with the surroundings, the

variations of the kinetic energy and the potential energy are negligible, thus the balance reduces to:

$$\dot{Q} = \Delta \dot{n}h = \sum_{i=1}^{nc} \dot{n}_i^{out} h_i^{out}(T^{out}, P^{out}) - \sum_{i=1}^{nc} \dot{n}_i^{in} h_i^{in}(T^{in}, P^{in}) \tag{4.45}$$

where $nc$ is the total number of the species that are in the reactor. Gas phase is assumed to be an ideal mixture.

The specific enthalpies are computed from the standard ($P_{ref} = 1$ bar) enthalpy of formation $h^0_{form}(T_{ref})$, the heat capacities $c_p$ and the molar volume $V_{m,i}$ of the species $i$:

$$h_i(T) = h^0_{form,i}(T_{ref}) + \int_{T_{ref}}^{T} c_{p,i}(T')dT' + \int_{P_{ref}}^{P} V_{m,i}dP'. \tag{4.46}$$

For a solid species $V_{m,i}$ is computed as the ratio of the molar weight to the density of $i$; for the gas species it is derived from the ideal gas law corrected to consider the repulsive interactions due to the co-volume:

$$V_{m,i} = \frac{RT}{P} + b_i \tag{4.47}$$

where $b_i$ is the co-volume of $i$, estimated as the Redlich–Kwong parameter through the critical properties of the species as:

$$b_i = 0.08662 \frac{RT_{c,i}}{P_{c,i}}. \tag{4.48}$$

The data used to evaluate the enthalpies are the ones of Knacke et al. (1991) tabulated in Table 2.3.

Computations were performed in two cases: a) isothermal reactor; b) adiabatic reactor.

In the first case, namely the isothermal reactor at 703 K, the enthalpy change of the absorber is -45.153 MW.

The accuracy of this hypothesis is verified by the adiabatic energy balance. The absorber still does not exchange work with the surroundings, the variations of the kinetic energy and the potential energy are still negligible, but the adiabatic condition entails that the reactor does not exchange heat as well with the surroundings ($\dot{Q} = 0$) and the temperature is no more constant within the reactor:

$$0 = \Delta \dot{n}h = \sum_{i=1}^{nc} \dot{n}_i^{out} h_i^{out} (T^{out}, P^{out}) - \sum_{i=1}^{nc} \dot{n}_i^{in} h_i^{in} (T^{in}, P^{in}).$$ (4.49)

In order to verify if the absorber is isothermal, the inlet temperature $T^{in}$ is a fixed variable and the unknown quantity is the outlet temperature $T^{out}$.

If $T^{in}$ is set equal to 703 K, the outlet temperature results to be 765 K. The temperature change from the bottom to the head is 62 K and the assumption of isothermal reactor is not acceptable.

Computations were performed also with the assumption of adiabatic reactor. In this case, the $CO_2$ conversion $X_{CO2}$ (in the mass balances) should be computed at the reactor average temperature, therefore $X_{CO2}$ was obtained iteratively. At each step, the mean value between $T^{in}$ and $T^{out}$ (arithmetic average) is used to evaluate the conversion from the mass balances. Then, the updated value of the conversion is used to recalculate the updated value of the outlet temperature from the adiabatic energy balance. Convergence was reached when two consecutive $T^{out}$ values differ of less than 1 K. The absorber mean temperature results to be 703 K when the syngas enters at 640 K.

**Table 4.6.** *Molar flowrates at the regenerator inlet and outlet*

|  | Inlet moles [kmol/s] | Oulet moles [kmol/s] |
|---|---|---|
| Carbon dioxide $CO_2$ | 0 | 0.3523 |
| Magnesium oxide MgO | 4.2117 | 4.5640 |
| Calcium carbonate $CaCO_3$ | 4. 2117 | 4. 5640 |
| Dolomite $CaMg(CO_3)_2$ | 0. 3523 | 0 |

As far as the regenerator, the reaction that takes place is the dolomite half decomposition (eq. (4.1)). When the absorber is operated isothermally, the regenerator is operated at the same temperature of the absorber but the pressure is lower. At 703 K, the decomposition partial pressure of $CO_2$ is 1.58 bar then the regenerator pressure of 1 bar ensures a (small) driving force for the reaction. The calcination reactions are faster than the carbonation ones and for this reason it is assumed that it goes to completion, namely all the dolomite that is formed in the absorber decomposes to carbon dioxide, magnesium oxide and calcium carbonate (Tab. 4.6). In addition, this assumption is supported also by the fact that the sorbent that exits from the absorber heats up to 765 K (in adiabatic conditions) and at this temperature the decomposition partial pressure of $CO_2$ is 9.40 bar, namely the driving force is larger.

## *4.2.5 Conclusions*

In this chapter, the process of carbon dioxide capture from an IGCC syngas was considered. The $CO_2$ capture was assumed to be performed by a high temperature regenerative process utilizing half decomposed dolomite sorbents. The process consists of an absorption unit (working at high pressure) and a regeneration unit (working at low pressure). Referring to a 70 MW plant and utilizing small sorbents (particle diameter equal to 70 µm), it was demonstrated that it is possible to capture about 68% of the inlet $CO_2$ in a fast fluidized bed (30 m high and 1.3 m large).

While this result is encouraging, further efforts are required in order to meet the requirement of 90% of $CO_2$ capture efficiency in a large power plant (US DOE, 2010).

However it is important to point out that the simulations were performed using kinetic data by Hassanzadeh (2007) which measured the MgO conversion as function of time from TGA (thermogravimetric analysis) experiments. These data are influenced by mass and heat transfer resistances that are present in the sample, instead in the absorber the particles are isolated from the each other with reduced heat/mass transfer resistances. Therefore, our simulation results are conservative as far as the resulting $CO_2$ capture efficiency. It is expected that using more accurate ('purified' by the heat/mass transfer resistances) data, the reaction rate should be faster and the carbon dioxide capture higher.

The main process challenges are:

1. the preparation of 'small' particles (particle diameter equal to 70 µm)

2. the sorbent transport between the absorber and the regenerator which are operated at different pressures.

The proposed solution for the solid transport is to adopt two lock hoppers between the absorber and the regenerator (Foscolo et al., 2011). After the sorbent is fed to the first of such containers the entrance and the exit are temporarily closed by two slide valves and the pressure is changed from 20 bar to low pressure; this procedure is discontinuous and the second container is used to accumulate the sorbent that exits from the first and that will be delivered to the regenerator in a continuous way thanks to a rotary valve placed at its exit. The transport from the regenerator to the absorber is conducted in analogous way.

The regenerator design was not considered in this study but the same procedure adopted for the absorber can be used. Its molar flowrates are smaller than the absorber ones and the reaction rate is faster then its size is expected to be smaller than the absorber.

## 4.3 $CO_2$ capture from combustion flue gases

### 4.3.1 Process description

In order to capture carbon dioxide from conventional coal/oil/gas fired power plants post-combustion capture is utilized and the capture unit is located downstream the boiler. In a typical coal fired plant, fuel is burned with air in a boiler to obtain steam that drives a turbine, or a generator, to produce electricity. The produced flue gas is composed mainly by $N_2$ and $CO_2$ and is sent to the control units of the nitrogen oxides $NO_x$, particulate matter and sulfur dioxide $SO_2$. The carbon separation unit can be placed after the combustion chamber, and the exiting flue gas can be sent to the vapor generation for the heat recovery. The disadvantages of the post combustion capture are the high volume of gas that must be treated and that the carbon dioxide is diluted (12-15%). Moreover the gas is at atmospheric pressure and compressing the captured $CO_2$ for the storage requires a high power load (US DOE, 2010).
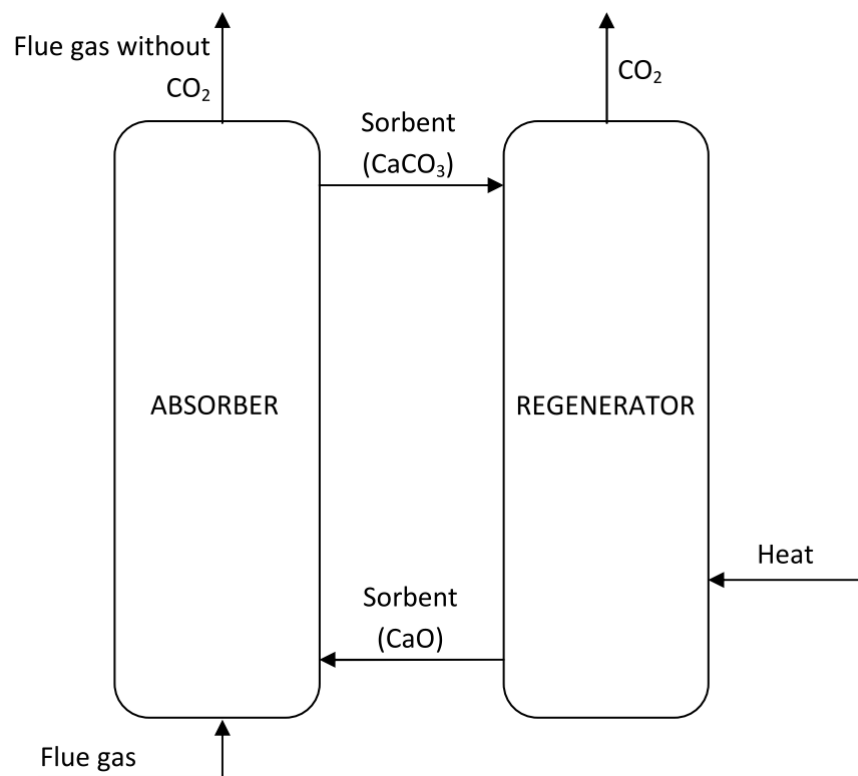


**Figure 4.8.** *Schematic of the $CO_2$ capture in a post-combustion process utilizing calcium based sorbents*

The sorbent used for the carbon dioxide capture is the calcium oxide, thus the reaction in the absorber/regenerator is:

$$CaO + CO_2 \leftrightarrow CaCO_3 \qquad\qquad (4.50)$$

In this case the absorber operates at ambient pressure, as in the combustion unit, and typical operating temperatures are between 450 and 700°C (Wang et al., 2010). The regeneration is carried out increasing the temperature and keeping the pressure at the constant value of 1 bar. Typical calcination temperatures are 850-1300°C (Wang et al., 2010) and are reached heating the reactor. It is possible to heat the calciner burning coal, but pure $O_2$ is required otherwise the purity of the carbon dioxide stream decreases (Dean et al., 2011; Wang et al., 2010). The process diagram is reported in Figure 4.8.

## 4.3.2 Operative conditions, kinetic data and $CO_2$ conversion

The operative conditions used to obtain the simulation results presented in this §4.3 were chosen from the work of Shimizu et al. (1999), namely the flue gas composition, pressure and temperature are the same as in Shimizu et al. (1999) (Table 4.7). Their gas flowrates are scaled to a 70 MW power plant. The process conditions (low pressure) imply that the gas flowrate are very high ($Q_v = 121.61$ m$^3$/s) in comparison to the IGCC case (3.43 m$^3$/s). The absorber diameter is assumed to be 4.5 m to avoid an excessively high gas velocity. The height is assumed to be 20 m. Such figures will be checked afterwards, namely it will be verified that the reactor can be operated either in the fast fluidization regime or in the dilute core-annular regime and that a high $CO_2$ capture efficiency can be obtained. Additionally, the solid flux $G_s$ is assumed to be equal to 244 kg/m$^2$s.

Operative conditions and reactor size are summarized in Table 4.7.

**Table 4.7.** *Operating conditions and reactor size*

| Variable | Value |
|---|---|
| Temperature $T$ [K] | 873 |
| Pressure $P$ [bar] | 1 |
| Flue gas composition [mol%] | $N_2 = 75.35$<br>$CO_2 = 14.88$<br>$H_2O = 6.45$<br>$O_2 = 3.32$ |
| Flue gas flowrate $Q_v$ [m$^3$/h] | 437760 |
| Absorber diameter $D$ [m] | 4.5 |
| Absorber height $H$ [m] | 20 |
| Solid flux $G_s$ [kg/m$^2$s] | 244 |

The gas and solid velocities are computed using the equations from (4.4) to (4.9). The residence time is $\tau_{solid}$ is equal to 2.5 s for a solid velocity equal to 7.357 m/s. The particle diameter $d_p$ is set equal to 100 µm.

The gas density $\rho_{gas}$ and the gas viscosity $\mu_{gas}$ are computed assuming that the flue gas is equal to a mixture composed of nitrogen, carbon dioxide, oxygen and water (Tab. 4.8). The gas density is computed as:

$$\rho_{gas} = \sum_{i=1}^{nc} PM_i \, y_i \frac{P}{RT} \tag{4.51}$$

**Table 4.8.** *Critical properties of gases (Bird et al., 2002)*

|  | $T_c$ [K] | $P_c$ [atm] | $\mu_c$ [g/cm s] |
|---|---|---|---|
| CO$_2$ | 304.2 | 72.8 | $343 \cdot 10^{-6}$ |
| N$_2$ | 126.2 | 33.5 | $180 \cdot 10^{-6}$ |
| H$_2$O | 647.1 | 217.7 | $402 \cdot 10^{-6}$ |
| O$_2$ | 154.4 | 49.7 | $250 \cdot 10^{-6}$ |
| Simulated flue gas | 187.2 | 51.77 | $220 \cdot 10^{-6}$ |

The mixture properties are average values computed by equations from (4.11) to (4.13), and are reported in Table 4.8.

The computed properties at the operative conditions are reported in Table 4.9, together with the sorbent density. The value of the sorbent density used in the simulations and reported in Table 4.9 is a mean value between the CaO and CaCO$_3$ densities (the value of the CaO density refers to a not thermally decomposed material). The sorbents used in the capture process are typically thermally decomposed to increase their reactivity, and therefore their density is lower respect to the not thermally decomposed material.

**Table 4.9.** *Gas and solid properties*

| Property | Value |
|---|---|
| Solid density $\rho_{solid}$ [kg/m$^3$] | 3015 |
| Gas density $\rho_{gas}$ [kg/m$^3$] | 0.4118 |
| Gas viscosity $\mu_{gas}$ [poise] | $340 \cdot 10^{-6}$ |

Assuming a particle diameter of 100 µm, the particles result to be fluidizable on the Geldart diagram (Fig. 4.3) they are on the boundary between group A and group B.

The reaction kinetic model is assumed to be a homogeneous model, in agreement with Grasa et al. (2008).

The kinetics of the carbon dioxide absorption is expressed similarly as for the magnesium based sorbents (§4.2.2):

$$\left.\frac{dX_{CaO}}{dt}\right|_{t\to 0} = j_{kin}(c_{CO_2} - c_{CO_2}^{eq})$$

(4.52)

$J_{kin}$ is a parameter introduced to reproduce the experimental data of Grasa et al. (2008) which refers to the initial fast reaction regime ($t \to 0$) for calcination at 650°C at partial pressures of $CO_2$ between 0.02 and 1 bar. It is equal to 0.0017 m³/(mol·s). In chapter 3 (§3.3), it was shown the (initial) fast reaction regime is not significantly affected by the particle size, therefore we used the mentioned data of Grasa et al. (2008) even if they refer to particles bigger than the particles considered in the numerical simulations of this §4.3. Additionally, Grasa et al. (2008) tested the effect of the temperature in the range from 550 to 700°C and found out that there is a poor dependency of the kinetic parameters on the temperature. Therefore, it is reasonable to neglect the dependency of $j_{int}$ on the operating temperature.

Finally, considering the small residence time (2.5 s), the assumption of operating in the in the (initial) fast reaction regime is correct; for Grasa et al. (2008) at partial pressure of $CO_2$ equals to 0.15 bar, as in the simulated case, the transition between the two phases occurs after 1-2 min.

The carbon dioxide conversion $X_{CO2}$ is evaluated assuming the absorber as an isothermal plug flow reactor, with the same approach of §4.2 (eq.s (4.18) to (4.19)). The balance results to be:

$$\dot{n}_{CO_2}^{in} dX_{CO_2} = \frac{w_{CaO}\rho_{solid}\varepsilon_{solid}}{PM_{CaO}} \frac{dX_{CaO}}{dt} Adh$$

(4.53)

$w_{CaO}$ is the solid mass fraction of calcium oxide in the sorbent, assumed to be equal to 1. Integrating from the inlet of the reactor, where the $X_{CO2}$ is 0, to the reactor exit $H$, the $CO_2$ conversion $X_{CO2}$ results to be 89.06 %, in agreement with the formula:

$$X_{CO_2} = -\frac{(c_{CO_2}^{in} - c_{CO_2}^{eq})}{c_{CO_2}^{in}}\left[\exp\left(-\frac{c_{CO_2}^{in} w_{CaO}\rho_{solid}\varepsilon_{solid} j_{int} AH}{\dot{n}_{CO_2}^{in} PM_{CaO}}\right) - 1\right]$$

(4.54)

As in §4.2, also in this case the gas and solid streams change their values and their velocities, but they are assumed to be constant.

The results are reported in Table 4.10.

**Table 4.10.** *Computed results*

| Resulting quantity | Value |
|---|---|
| Solid fraction $\varepsilon_{solid}$ [-] | 0.01 |
| $CO_2$ conversion $X_{CO2}$ (%) | 89.06 |
| Gas velocity $v_{gas}$ (m/s) | 7.724 |
| Solid velocity $v_{solid}$ (m/s) | 7.357 |

The solid fraction results to be 1%; this is a typical value for the core annular dilute transport regime ($\varepsilon_{solid}$ = 0.01-0.05), according to Bi and Grace (1995). The solid fraction cannot be increased to values typical of the fast fluidization regime ($\varepsilon_{solid}$ = 0.05-0.20) because the solid flux would result equal to several hundreds of kg/(m$^2$s).

Despite the low residence time (2.5 s) the $CO_2$ conversion is high: this is indicative of the high reaction rate of the carbonation reaction.

## 4.3.3 Fluidization analysis

In order to verify the fluidization regime in which the absorber is operated, the values of type A and type C choking velocities are computed, as indicated by eq.s (4.23) and (4.24). With the simulated data, $V_{CC}$ is 4.205 m/s and $V_{CA}$ is 8.603 m/s.

Bi and Grace (1995) identified several criteria to define the fluidization regime. One of these criteria is based on the value of the gas velocity. In the simulated case, the gas velocity $v_{gas}$ is equal to 7.724 m/s and therefore the gas velocity is between $V_{CC}$ and $V_{CA}$ ($V_{CC} < v_{gas} < V_{CA}$). According to this criterion, the absorber is operated in the fast fluidization regime (close to the boundary with the core-annular dilute transport regime). A second criterion is based on the solid volumetric fraction, which in the simulated case is equal 0.01. According to the criterion of Bi and Grace (1995) for the solid volumetric fractions, the absorber is operated in the core annular dilute transport regime. In conclusion, the absorber is operated either in the fast fluidization or in the core-annular dilute transport regime.

Increasing the solid flowrate the removal efficiency increases and also the choking velocities (Fig. 4.9, left). However, $G_s$ cannot be increased indefinitely, because a too high solid load entails operative difficulties. Smolders and Baeyens (2001) collected experimental data on solids hold up profile for fluidization reactors: with $v_{gas}$ = 7.724 m/s the solid flux is usually comprised between 70 and 500 ks/m$^2$s. The solid flux range of Figure 4.9 corresponds to a variation of $\varepsilon_{solid}$ between 0.001 and 0.030. The high reaction rate allows to obtain a good $CO_2$ capture also in the dilute phase transport.
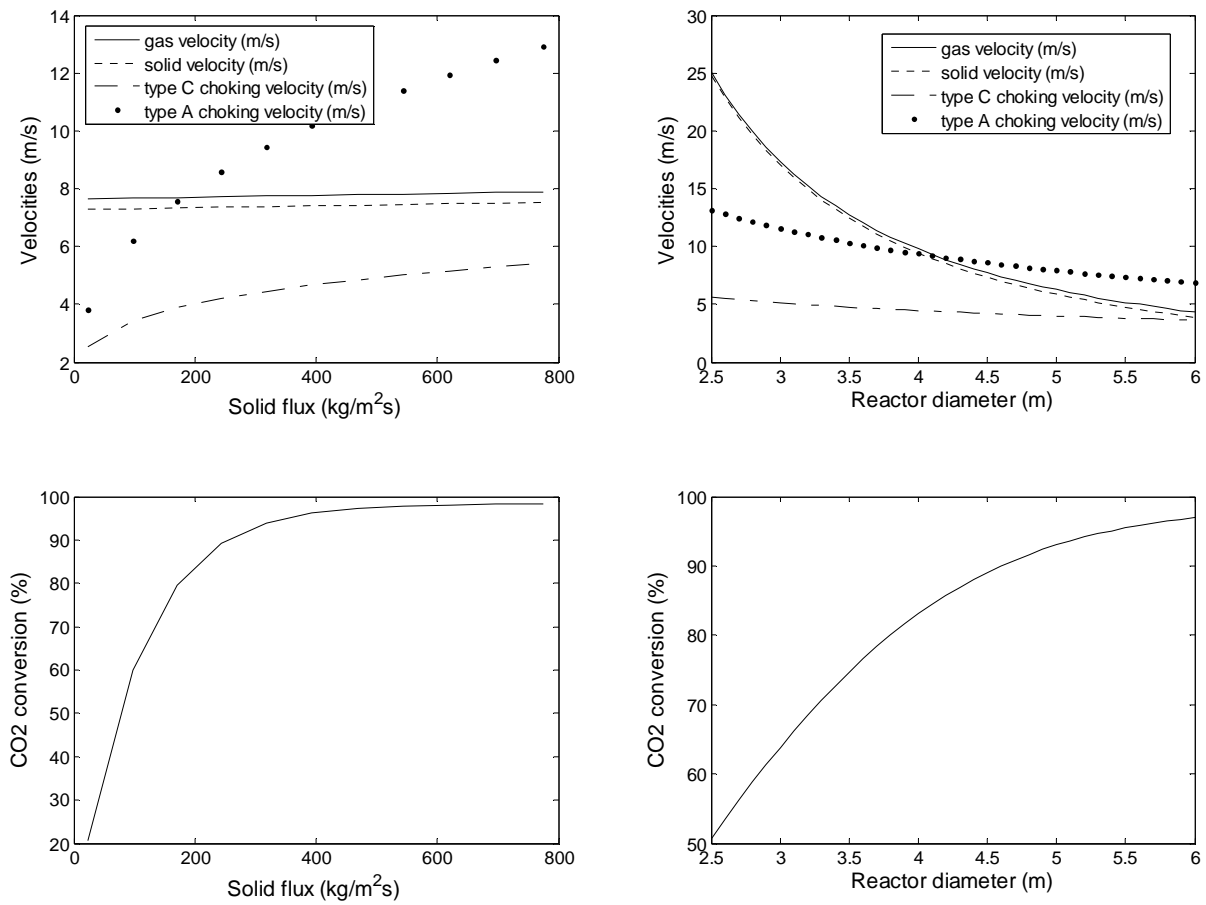
**Figure 4.9.** *Parametric studies: the figures represent the dependence of $v_{gas}$, $v_{solid}$, $V_{CC}$ and $V_{CA}$ (top) and $CO_2$ conversion (bottom) on the solid flux $G_s$ (left) and on reactor diameter D (right)*

Increasing the reactor diameter (Fig. 4.9, right), the gas velocity decreases and its decrease rate is faster than the rate at which the choking velocities drop. In the simulated case the limits for the fast fluidization regime are 4.2-6.0 m.

## 4.3.4 Material and energy balances

The reaction that takes place in the absorber is:

$$CaO + CO_2 \leftrightarrow CaCO_3 \qquad (4.50)$$

The absorber operates in stationary state, then the accumulation term in the balances is set equal to 0 and the resulting general formula for the material balance results:

$$0 = Inlet - Outlet + Production - Consumption. \qquad (4.27)$$

The material balances are evaluated for each compound and are related by the reaction stoichiometry:

$$0 = \dot{n}_{CO_2}^{in} - \dot{n}_{CO_2}^{out} - \dot{n}_{CO_2}^{cons} \tag{4.55}$$

$$0 = \dot{n}_{CaCO_3}^{in} - \dot{n}_{CaCO_3}^{out} + \dot{n}_{CaCO_3}^{prod} \tag{4.56}$$

$$0 = \dot{n}_{CaO}^{in} - \dot{n}_{CaO}^{out} - \dot{n}_{CaO}^{cons} \tag{4.57}$$

$$0 = \dot{n}_{H_2}^{in} - \dot{n}_{H_2}^{out} \tag{4.58}$$

$$0 = \dot{n}_{O_2}^{in} - \dot{n}_{O_2}^{out} \tag{4.59}$$

$$0 = \dot{n}_{H_2O}^{in} - \dot{n}_{H_2O}^{out} \tag{4.60}$$

$$\dot{n}_{CO_2}^{cons} = \dot{n}_{CaO}^{cons} = \dot{n}_{CaCO_3}^{prod} \tag{4.61}$$

The molar flowrate of the solid species are evaluated from the solid flux $G_s$:

$$\dot{n}_{CaO}^{in} = \frac{G_s A}{PM_{CaO}} \tag{4.62}$$

$$\dot{n}_{CaCO_3}^{in} = 0. \tag{4.63}$$

The outlet flowrate are obtained subtracting the consumed (or adding the produced) moles from the inlet ones, knowing that one mole of CO$_2$ reacts with one mole of CaO to give one mole of CaCO$_3$:

$$\dot{n}_{CaO}^{out} = \dot{n}_{CaO}^{in} - \dot{n}_{CaO}^{cons} = \dot{n}_{CaO}^{in} - \dot{n}_{CO_2}^{cons} \tag{4.64}$$

$$\dot{n}_{CaCO_3}^{out} = \dot{n}_{CaCO_3}^{in} + \dot{n}_{CaCO_3}^{prod} = \dot{n}_{CO_2}^{cons} \tag{4.65}$$

$$\dot{n}_{CO_2}^{cons} = \dot{n}_{CO_2}^{in} X_{CO_2}. \tag{4.66}$$

The computed molar flowrates are reported in Table 4.11. The amount of converted moles in the absorber is 0.2221 kmol/s for each species.

**Table 4.11.** *Molar flowrates at the absorber inlet and outlet*

|  | Inlet moles [kmol/s] | Oulet moles [kmol/s] |
|---|---|---|
| Carbon dioxide $CO_2$ | 0.2494 | 0.0273 |
| Nitrogen $N_2$ | 1.2624 | 1.2624 |
| Water vapor $H_2O$ | 0.1080 | 0.1080 |
| Oxygen $O_2$ | 0.0557 | 0.0557 |
| Calcium oxide $CaO$ | 69.2651 | 69.0430 |
| Calcium carbonate $CaCO_3$ | 0 | 0.2221 |

In the energy balance it can be assumed that it does not exchange work with the surroundings, the variations of the kinetic energy and of the potential energy are negligible, thus the balance reduces to:

$$\dot{Q} = \Delta\dot{n}h = \sum_{i=1}^{nc} \dot{n}_i^{out} h_i^{out}(T^{out}, P^{out}) - \sum_{i=1}^{nc} \dot{n}_i^{in} h_i^{in}(T^{in}, P^{in}) \tag{4.45}$$

The formulae for the specific enthalpies were presented in §4.2.4. Data of Table 2.1 were used in the computations. Additional required data for nitrogen, $H_2O$ and oxygen were found in Perry and Green (1997) and are tabulated in Table 4.12. It is important to note that for the $H_2O$ the heat capacity is defined as $c_p = a + bT + cT^2$ ($T$ in K); for $N_2$ and $O_2$, the heat capacities are expressed as $CaCO_3$, $CaO$ and $CO_2$.

**Table 4.12.** *Thermodynamic data used for $N_2$, $H_2O$, and $O_2$; source Perry and Green (1997)*

|  | $c_p$ [J/mol*K] | | | $\Delta h^0_{form}$ (298K) [kJ/mol] |
|---|---|---|---|---|
|  | a | b | c |  |
| $N_2$ | 27.196 | 4.184e-3 | 0 | 0 |
| $H_2O$ | 34.39248 | 0.6276e-3 | -5.60656e-6 | -241.8264 |
| $O_2$ | 34.60168 | 1.07947e-3 | -7.853368e+5 | 0 |

Assuming to operate the absorber isothermally at 873 K, the enthalpy change in the absorber is -39.650 MW.

The accuracy of the hypothesis of isothermal reactor is verified by solving the energy balance in adiabatic conditions. If $T^{in}$ is 873 K, the outlet temperature $T^{out}$ results 882 K; the temperature change is 9 K, therefore the assumption of isothermal reactor is acceptable. Considering the low temperature change between the inlet/outlet and the poor dependence of

the kinetic parameters on the temperature, there is no need to update the reactor average temperature and the conversion in the material balance.

As far as the regenerator, the reaction that takes place is the calcite decomposition (the reverse reaction in eq. (4.50)). Typical calcination temperatures are 850-1300°C (Wang et al., 2010); the simulated reactor is assumed to operate isothermally at $T_{reg}$ = 950°C, in agreement with the mentioned range. At this $T_{reg}$ the decomposition $CO_2$ partial pressure is 2.46 bar, enough to ensure a driving force for the reaction.

### 4.3.5 Conclusions

In this chapter, the process of carbon dioxide capture from a combustion flue gas was considered. The $CO_2$ capture was assumed to be performed by a high temperature regenerative process utilizing calcium oxide based sorbents. The process consists of an absorption unit (working at low temperature) and a regeneration unit (working at high temperature). Referring to a 70 MW plant and utilizing small sorbents (particle diameter equal to 100 µm), it was demonstrated that it is possible to capture about 90% of the inlet $CO_2$ in a dilute fluidized bed (20 m high and 4.5 m large).

Kinetic data used in the simulations were obtained by Grasa et al. (2008) from TGA (thermogravimetric analysis) experiments, which are influenced by mass and heat transfer resistances that are present in the sample, instead in the absorber the particles are isolated from the each other with reduced heat/mass transfer resistances. From this point of view the simulation result of capture efficiency (already high) should be conservative. However, the kinetic data used in the simulations refer to the first cycle of absorption. As explained in Chapter 3, the reaction rates of absorption decrease increasing the number of cycles of absorption/calcinations. A more detailed analysis is required to estimate the impact of these factors.

One of the main process challenges is the absorber size. In fact, the presence of nitrogen in the flue gas, the elevated temperature and the ambient pressure of the stream result in high volumetric flowrates. For this reason, the construction of an absorption unit in an existing coal combustion plant does not seem to be feasible. In this case, the carbon dioxide capture can be realized injecting the CaO sorbent in the gas stream, after the exit from the combustion chamber. In this case an exhaustive CFD analysis should be performed, to understand where the particles are to be collected, and then sent to the regeneration unit.

The regenerator design was not considered but the same procedure adopted for the absorber can be used. Its molar flowrates are smaller than the absorber ones and the reaction rate is faster therefore its size is expected to be smaller than the absorber.

# Conclusions

This work of thesis is the first step in a new research group, whose goal is to investigate a promising technology for the carbon dioxide capture: the absorption on calcium and magnesium based solid sorbents. The main goal of this thesis is to demonstrate the feasibility of two carbon dioxide capture processes, which utilize the solid sorbents, for coal gasification and coal combustion power plants: in both cases, the gas streams (syngas or flue gases) are processed in the absorber and the solid sorbents react with the $CO_2$ producing carbonates, then the sorbents are sent to the regenerator where it is decomposed releasing a stream with the captured $CO_2$. Magnesium based solid sorbents were used in the case of $CO_2$ capture in coal gasification power plants, and calcium based solid sorbents were considered in the case of $CO_2$ capture coal in combustion power plants.

The design of the absorber required to develop/collect preliminarily thermodynamic and kinetic data on the carbonate decomposition/carbon dioxide absorption reactions.

The equilibrium thermal decomposition curves of dolomite, calcite, and magnesite were computed. These curves are required to evaluate the driving force in the absorption kinetics.

Kinetic data on carbonate decomposition/carbon dioxide absorption reactions were retrieved in the literature. In the case of calcium based sorbents, thermogravimetric analyses were conducted to obtain the decomposition temperature and time of calcite and dolomite and kinetic data of $CO_2$ absorption on calcium oxides. The performance obtained, in terms of $CO_2$ absorption rate, with calcium oxide produced by thermal decomposition of calcium carbonate is in line with the literature results.

The absorber design was developed both in the case of pre-combustion capture in a coal gasification power plant (IGCC) and in the case of post-combustion capture in a coal combustion power plant.

For the IGCC case, referring to a 70 MW plant and utilizing small sorbents (particle diameter equal to 70 µm), it was demonstrated that it is possible to capture about 68% of the inlet $CO_2$ in a fast fluidized bed (30 m high and 1.3 m large). While this result is encouraging, further efforts are required in order to meet the requirement of 90% of $CO_2$ capture efficiency in a large power plant. It should be noticed that our simulation results are conservative as far as the resulting $CO_2$ capture efficiency for two reasons:

1) the simulations were performed using kinetic data from TGA experiments. These data are influenced by mass and heat transfer resistances that are present in the sample, instead in the absorber the particles are isolated from the each other with reduced heat/mass transfer resistances. It is expected that using more accurate ('purified' by the heat/mass transfer resistances) data, the reaction rate should be faster and the carbon dioxide capture higher.

2) the operating pressure used in the simulations is 20 bar, because the kinetic data are available in literature at such pressure. However, coal gasification is typically operated at higher pressures. At higher pressures, the carbon dioxide concentration and therefore the reaction rate are higher, leading to higher conversions and capture efficiencies.

The process present two challenges: the preparation of small diameter particles and the sorbent transport from the absorber to the regenerator, which are operated at different pressures. Two lock hoppers between the two reactors is the proposed solution: the sorbent is fed to the first of such containers which is temporarily closed and the pressure is changed from 20 bar to low pressure; afterwards, at low pressure the second container is used to accumulate the sorbent that is delivered to the regenerator in a continuous way thanks to a rotary valve placed at its exit. The transport from the regenerator to the absorber is conducted in analogous way.

As far as the combustion flue gas treatment, referring to a 70 MW plant and utilizing small sorbents (particle diameter equal to 100 µm), it was demonstrated that it is possible to capture about 90% of the inlet $CO_2$ in a dilute fluidized bed (20 m high and 4.5 m large). It is important to point out that in this case the presence of nitrogen in the flue gas, the high temperature and the ambient pressure of the stream result in high volumetric flowrates, and therefore the absorber size is significant. For this reason, the construction of an absorption unit in an existing coal combustion plant doesn't seem to be feasible. In this case, the carbon dioxide capture can be realized injecting the CaO sorbent in the gas stream, after the exit from the combustion chamber; a detailed CFD analysis would be valuable to understand and optimize the fluid dynamics of the injected particles.

Kinetic data of the carbon dioxide absorption on calcium oxide were obtained from TGA experiments as well, therefore the computed carbon dioxide conversion is conservative because the TGA tests are affected by mass and heat transfer limitations. A detailed analysis is required to obtain more accurate data, distinguishing between the "purely kinetic" data from the effects of heat/mass transfer.

In both cases (coal combustion and coal gasification), further investigations should be performed as far as the dependence of the $CO_2$ capture efficiency on the number of calcinations/carbonation cycles: in fact, increasing this parameter the capture efficiency drops off, mainly because of sorbent sintering.

As far as future investigations, detailed analyses about the enhancement of MgO reaction rate and the limitation of calcium and magnesium oxides sintering during the regeneration step represent a very interesting aspect.

# References

Baker, E.H. (1962). The calcium oxide-carbon dioxide system in pressure range 1-300 atmospheres. *J. Chem. Soc.*, **70**, 464-470.

Bi, H.T. and Grace J.R. (1995). Flow regime diagrams for gas-solid fluidization and upward transport. *Int. J. Multiphase Flow*, **21**, 1229-1236.

Bird, R.B., W.E. Stewart and E.N. Lightfoot (2002). Transport phenomena (2$^{nd}$ ed.). John Wiley & Sons, Inc., New York (U.S.A.).

Borgwardt, R.H. (1985). Calcination kinetics and surface area of dispersed limestone particles. *AIChE J.*, **31**, 103-111.

Chase, M.W. (1998). NIST-JANAF thermochemical tables - Part I (4$^{th}$ ed.). *J. Phys. Chem. Ref. Data*, Monograph n.9.

Dean, C.C., J. Blamey, N.H. Florin, M.J. Al-Jeboori, P.S. Fennell (2011). The calcium looping cycle for CO2 capture from power generation, cement manufacture and hydrogen production. *Chem. Eng. Res. Des.*, **89**, 836-855.

Foscolo, P.U., K. Gallucci and L. Di Felice (2011). Ottimizzazione del ciclo di gassificazione carbone-decarbonatazione syngas e calcinazione sorbente. Report RdS/2011/217 Ministero dello Sviluppo Economico - ENEA

Galan, I., F.P. Glasser and C. Andrade(2012). Calcium carbonate decomposition, *J. Therm. Anal. Calorim.,* DOI: 10.1007/s10973-012-2290-x, (2012).

Gallagher, P.K. and D.W. Johnson Jr. (1973). The effects of sample size and heating rate on the kinetics of the thermal decomposition of CaCO$_3$. *Thermochim. Acta*, **6**, 67-83.

Gallagher, P.K. and D.W. Johnson Jr. (1976). Kinetics of the thermal decomposition of CaCO3 in CO2 and some observations on the kinetic compensation effect. *Thermochim. Acta*, **14**, 255-261.

Gidaspow, D. (1994). Multiphase flow and fluidization. Academic Press, New York (U.S.A.).

Grace, J.R. (1986). Contacting modes and behavior classification of gas-solid and other two-phase suspensions. *Can. J. Chem. Eng.*, **64**, 353-363.

Graf, D.L. and J.R. Goldsmith (1955). Dolomite-magnesian calcite relations at elevated temperatures and CO$_2$ pressures. *Geochim. Cosmochim. Acta*, **7**, 109-128.

Grasa, G.S., J.C. Abanades, M. Alonso and B. Gonzalez (2008). Reactivity of highly cycled particles of CaO in a carbonation/calcination loop. *Chem. Eng. J.*, **137**, 561-567.

Gunasekaran, S. and G. Anbalagan (2007), Spectroscopy study of phase transitions in natutal calcite mineral. *Spectrochim. Acta*, **69**, Part A, 1246-1251.

Harker, R.I. and O.F. Tuttle (1955). Studies in the system CaO-MgO-CO$_2$; Part I, The thermal dissociation of calcite, dolomite and magnesite. *Am. J. Sci.*, **253**, 209-224.

Hassanzadeh, A. (2007). A regenerative process for $CO_2$ removal and hydrogen production in IGCC. Ph.D. Thesis, Illinois Institute of Technology (U.S.A.).

Hassanzadeh, A. and Abbasian J. (2010). Regenerable MgO-based sorbents for high-temperature CO2 removal from syngas: 1. Sorbent development, evaluation and reaction modeling. *Fuel*, **89**, 1287-1297.

IPCC (2007). Climate Change 2007: Synthesis Report. Contribution of Working Groups I, II and III to the Fourth Assessment Report of the Intergovernmental Panel on Climate Change Core Writing Team, Pachauri, R.K and Reisinger, A. (eds.). Cambridge University Press, Cambridge (UK).

IPCC (2005). Special Report on Carbon Dioxide Capture and Storage. B. Metz, O. Davidson, H. de Coninck, M. Loos, and L. Meyer (eds.), Cambridge University Press, Cambridge (UK).

Knacke, O., O. Kubaschewski and K. Hesselman (1991). Thermochemical properties of inorganic substances (2$^{nd}$ ed.). Springer-Verlag, Berlin (Germany).

Perry, R. and D. Green (1997). Perry's chemical engineers' handbook (7$^{th}$ ed.). McGraw-Hill Book Co., New York (U.S.A.).

Reid, R.C., Prausnitz J.M., Poling B.E. (1988). The Properties of Gases and Liquids (4$^{th}$ ed.). McGraw-Hill Book Co., New York (USA).

Rodriguez-Navarro, C., E. Ruiz-Agudo, A. Luque, A.B. Rodriguez-Navarro, M. Ortega-Huertas (2009). Thermal decomposition of calcite: Mechanisms of formation and textural evolution of CaO nanocrystals. *Am. Mineral.*, **94**, 578-593.

Rodriguez-Navarro, C., K. Kudlacz and E. Ruiz-Agudo (2012). The mechanism of thermal decomposition of dolomite: New insights from 2D-XRD and TEM analyses. *Am. Mineral.*, **97**, 38-51.

Romero Salvador, A. (1989). Effects of sample weight, particle size, purge gas and crystalline structure on the observed kinetic parameters of calcium carbonate decomposition. *Thermochim. Acta*, **143**, 339-345.

Samtani, M., D. Dollimore and K. Alexander (2001). Thermal decomposition of dolomite in an atmosphere of carbon dioxide - the effect of procedural variables in thermal analysis. *J. Therm. Anal. Calorim.*, **65**, 93-101.

Samtani, M., D. Dollimore and K.S. Alexander (2002). Comparison of dolomite decomposition kinetics with related carbonates and the effect of procedural variables on its kinetic parameters. *Thermochim. Acta*, **392-393**, 135-145.

Satterfield, C.S. and F. Feakes (1959). Kinetics of thermal decomposition of calcium carbonate. *AIChE J.*, **5**, 115-122.

Schieber, J.D. and J.J. de Pablo. Chemical, biological and material engineering thermodynamics. Under publication for Cambridge University Press.

Shimizu, T., T. Hirama, H. Hosoda, K. Kitano, M. Inagaki and K. Tejima (1999). A twin fluid-bed reactor for removal of $CO_2$ from combustion processes. *Chem. Eng. Res. Des.*, 77, 62-68.

Smolders, K and J. Baeyens (2001). Gas fuidized beds operating at high velocities: a critical review of occurring regimes. *Powder Technol.*, **119**, 269-291.

Stern, K.H. (2001). High temperature properties and thermal decomposition of inorganic salts with oxyanions. CRC Press, Boca Raton (U.S.A.).

US Department of Energy (2010). DOE/NETL Carbon Dioxide Capture and Storage RD&D Roadmap.

Wang, W., S. Ramkumar, S. Li, D. Wong, M. Iyer, B.B. Sakadjian, R. Statnick and L.S. Fan (2010). Subpilot demonstration of the carbonation-calcination reaction (CCR) process: high-temperature $CO_2$ and sulfur capture from coal-fired power plants. *Ind. Eng. Chem. Res.*, **49**, 5094-5101.

Wang, Y. and W.J. Thomson (1995). The effect of sample preparation on the thermal decomposition of $CaCO_3$. *Thermochim. Acta*, **255**, 383-390.

Wilburn, F.W., J. H. Sharp, D.M. Tinsley and R.M. McIntosh (1991). The effect of procedural variables on TG, DTG and DTA curves of calcium carbonate. *J. Therm. Anal.*, **37**, 2003-2019.


Web site

http://webbook.nist.gov/chemistry/

http://www.netl.doe.gov/technologies/coalpower/gasification/index.ht
ml